Liegt aus

Internal Report
DESY F35D–93–06
October 1993

Experimental Aspects of the Luminosity Measurement in the ZEUS Experiment

by

K. Piotrzkowski

Eigentum der DESY Bibliothek
Property of the DESY Library
Zugang: 15. NOV. 1993
Accession:
Leihfrist: Tage
Loan period: days

DESY behält sich alle Rechte für den Fall der Schutzrechtserteilung und für die wirtschaftliche Verwertung der in diesem Bericht enthaltenen Informationen vor.

DESY reserves all rights for commercial use of information included in this report, especially in case of filing application for or grant of patents.

"Die Verantwortung für den Inhalt dieses
Internen Berichtes liegt ausschließlich beim Verfasser"

Experimental Aspects of the Luminosity Measurement in the ZEUS Experiment

PhD Thesis

Krzysztof Piotrzkowski
Institute of Nuclear Physics,
Kraków, Poland

To Grażyna

Hamburg, October 18, 1993

Contents

Foreword **4**

1 Introduction **7**
1.1 The Luminosity of Collisions . . . 7
1.1.1 The Definition of Luminosity . . . 7
1.1.2 Methods of Luminosity Measurement . . . 8
1.2 The HERA - *ep* Collider . . . 9
1.2.1 Basic Collider Physics . . . 9
1.2.2 The HERA Collider . . . 12
1.3 The ZEUS Experiment . . . 17
1.3.1 The ZEUS Detector . . . 17
1.3.2 The ZEUS Trigger System . . . 20
1.4 The Luminosity Measurement in ZEUS . . . 22

2 The ZEUS Luminosity Monitor **27**
2.1 Introduction . . . 27
2.2 The Detectors . . . 30
2.2.1 The Calorimeters . . . 30
2.2.2 The Position Detectors . . . 34
2.2.3 The Čerenkov Counter . . . 38
2.2.4 Shielding . . . 40
2.3 The Calibration of the Detectors . . . 41
2.3.1 The Calibration of the Calorimeters . . . 41
2.3.2 The Calibration of the Position Detector . . . 44
2.4 The Data Acquisition System . . . 45
2.4.1 An Overview . . . 45
2.4.2 The Structure of the DAQ . . . 47

3 The Measurement of Luminosity **50**
3.1 The Experimental Procedure . . . 50
3.1.1 Basic Formulae . . . 50
3.1.2 The Experimental Methods . . . 52
3.2 The Measurement of the Acceptance . . . 53
3.2.1 The Beam Position Measurements . . . 53
3.2.2 The Photon Acceptance . . . 53

3.2.3 The Measurement of the Electron Acceptance . . . 59
3.3 Corrections . . . 63
3.3.1 Calorimeter Resolution and Absorber Effects. . . . 63
3.3.2 Subtraction of the Beam Gas Background . . . 65
3.3.3 Multiple Event Correction . . . 65
3.3.4 Timing and Satellite Bunches . . . 68
3.4 Measurement of the Energy Flux in the Photon Calorimeter . . . 70
3.5 Cross-Check Procedures and Experimental Results . . . 71
3.5.1 Comparision of Different Luminosity Measurements . . . 71
3.5.2 The Specific Luminosity . . . 73
3.5.3 The Method of Beam Separation . . . 73
3.5.4 Summary of Experimental Results . . . 74

4 Background Processes **77**
4.1 *egas* Bremsstrahlung . . . 77
4.2 Synchrotron Radiation . . . 78
4.3 The Proton Beam Halo . . . 81
4.4 e^+e^- Pair Photoproduction . . . 84
4.5 Other Processes . . . 85
4.6 Summary . . . 85

5 Experimental Errors **86**
5.1 Uncertainty in the Acceptances . . . 86
5.2 The Energy Calibration and Resolution . . . 86
5.3 Subtraction of the *egas* Background . . . 88
5.4 Satellite Bunch Corrections . . . 90
5.5 Multiple Events . . . 91
5.6 Summary . . . 91

6 Conclusions **94**

Bibliography **97**

Appendix **100**

List of Symbols

Symbol	*Meaning*	Units
$A_{e'}$	Acceptance of bremsstrahlung electron	
A_γ	Acceptance of bremsstrahlung photon	
E_e	Energy of electron beam	$[GeV]$
$E_{e'}$	Energy of bremsstrahlung electron	$[GeV]$
E_p	Energy of proton beam	$[GeV]$
E_γ	Energy of bremsstrahlung photon	$[GeV]$
E_{tot}	Total energy, $E_{tot} = E_\gamma + E_{e'}$	$[GeV]$
I_e^{pilot}	Current of electron pilot bunches	$[mA]$
I_e^{tot}	Total current of electron beam	$[mA]$
I_p^{tot}	Total current of proton beam	$[mA]$
$\mathcal{L}$	Luminosity	$[cm^{-2}s^{-1}]$
L	Integrated luminosity	$[cm^{-2}]$
$\mathcal{L}_{spec}$	Specific luminosity	$[cm^{-2}s^{-1}]$ (or $[cm^{-2}s^{-1}\mu A^{-2}]$)
β	β-function	$[m]$
ϵ	Beam emittance	$[m\ rad]$

Abbreviation	*Meaning*
BCN	Bunch Crossing Number
FADC	'Flash' Analog-to-Digit Converter
FLT	First Level Trigger
IP	Interaction Point
LMDAQ	Luminosity Monitor Data AQuisition system
e^-cal	Electron calorimeter of the luminosity monitor
γcal	Photon calorimeter of the luminosity monitor
PMT	PhotoMultiplier Tube

Foreword

The method of scattering "structureless probes" (e.g. electrons or muons) on complex objects (e.g. atoms, nuclei or hadrons) has a long history as a tool in the study of the constituents of matter. The structure of the object under investigation (the "target") is derived from the measured probabilities (differential cross-sections) for the scattering of the incident particles (the "probes") under different angles. With this method E.Rutherford discovered the structure of the atom in 1911, and in the 1960's and 1970's scattering experiments of high energy electrons and neutrinos on various targets helped to establish that hadrons are built-up from quarks and gluons. It follows from the uncertainty principle that the resolving power of a scattering experiment increases with the energy and momentum of the particle (usually a virtual photon) exchanged between the probe and the target. Originally, the target was at rest and the resolving power was increased by raising the energy of the beam of probing particles. The beam energy, however, is most efficiently utilized when both the probe and target move against each other and collide "head-on", thus leading to the construction of colliding beam accelerators, so-called colliders, which have pushed further the frontiers of this scientific research.

An important part of each scattering experiment is the measurement of the luminosity. Since the error on the luminosity enters directly into the error of the measured cross sections, a good understanding of the luminosity measurement is required. The aim of this thesis is to describe the experimental procedures of the luminosity measurement in the ZEUS experiment at the HERA *ep* collider.

In the ZEUS experiment the collisions of 820 GeV protons and 26.7 GeV electrons are studied. The primary goal of the experiment is to investigate the proton structure in a completely new kinematic region and to search for structure, now only hypothetical, of electrons and quarks. The ZEUS research program also includes studies of the structure of the photon and of its "hadronic component" in the high-energy collisions of almost-real photons with beam protons, as well as the investigation of the nature of the elusive Pomeron particle in processes of hard proton diffraction. Last but not least, the ZEUS experiment will be able to perform a number of stringent tests of Quantum Chromo-Dynamics, the present theory of strong interactions, and of the Weinberg-Salam model of electro-weak interactions.

The luminosity measurement in ZEUS is based on the measurement of the $ep \to e'\gamma p'$ bremsstrahlung process [1, 2] with the use of the detectors which have been called the LUMI monitor. The LUMI monitor consists of two "branches" which are used to measure photons and electrons produced at small angles with respect to the electron beam direction. Additionally, the LUMI electron branch can be used to convert HERA into a γp collider by tagging low-Q^2 processes [3, 4], and the LUMI photon branch can be used

to measure the initial state radiation produced by electrons in ep scattering [5, 6]. The bremsstrahlung process is used not only for the luminosity measurement but also as a precise, well known probe for the calibration of the LUMI detectors.

The basic physics of bremsstrahlung production was quite well established in the 1930's. At HERA, however, effects such as the modification of the bremsstrahlung cross-section due to large impact parameters and the contribution to the measured photon spectrum of Compton scattered blackbody photons make the luminosity measurement particulary exciting and interesting.

A precise measurement of the luminosity with the LUMI monitor requires a detailed understanding of the detector performance as well as a good treatment of the background processes. The exceptionally high rate of beam collisions and the very high rate of hard bremsstrahlung events at HERA make this a difficult task. In this thesis these and other aspects of the luminosity measurement in the ZEUS experiment at HERA are considered.

The thesis is organized as follows. At the begining of the first chapter the definition of the luminosity and methods of its measurement are introduced. Then, basic collider physics is presented with an emphasis on the parameters relevant to the measurement of the luminosity. In the following two sections the HERA collider and the ZEUS experiment are described. The chapter ends with an overview of the luminosity measurement in the ZEUS experiment. The second chapter covers the construction, performance and calibration of the detectors of the LUMI monitor as well as the functioning of the data acquisition system. The third chapter begins with a discussion of the details of the procedure of the luminosity measurement which is followed by a description of the various experimental corrections which are required in the calculation of the luminosity. It is closed with a presentation of the experimental results and a discussion of the consistency of the results. The fourth chapter contains a description of the backgrounds and the methods used to control them. The fifth chapter contains a discussion of the systematic errors. Various sources of errors are elaborated what enables one to consider further improvements and extensions of the measurement. The thesis is closed with concluding remarks in sixth chapter.

Most of the results presented here have not been previously published. We shall point out some of the aspects of the luminosity measurement described in this thesis:

- The methods which maintain the calibration of the detectors of the LUMI monitor are described (Sections 2.3, 5.3).
- The acceptance of bremsstrahlung events in the LUMI monitor, i.e. the probability that the photon (or electron, or photon and electron) produced in bremsstrahlung reaches the detector, is an important factor in deriving the luminosity from the data. The acceptance has been experimentally evaluated and continuously monitored during the course of the experiment (Section 3.2).
- The bremsstrahlung from the collisions of beam electrons with the nuclei of the residual gas molecules has been found to be a significant source of background. A general method to correct for this and for other electron-gas backgrounds has been successfully applied (Section 3.3).
- The background due to synchrotron radiation has been studied (Section 4.2).
- The problems caused by the high event rate at the nominal HERA luminosity will be difficult to handle. The effect of multiple events in a single bunch crossing has been measured at the relatively low rates presently available and compared with the expectations from Monte Carlo simulations (Sections 3.3, 5.4).
- A method of luminosity measurement which is insensitive to the effect of multiple events was developed, and in the future it may be applied to verify the main luminosity measurement (Section 3.4).

Chapter 1

Introduction

1.1 The Luminosity of Collisions

1.1.1 The Definition of Luminosity

The energy of the beams and the luminosity of the collisions are essential quantities in scattering experiments. The beam energies determine the maximum resolution power of the experiment. The luminosity, $\mathcal{L}$, relates the reaction rate dN/dt of a process to its cross-section, σ, and is defined by

$$dN/dt = \mathcal{L}\ \sigma. \tag{1.1}$$

$\mathcal{L}$ is usually expressed in units of $cm^{-2}s^{-1}$.

For experiments in which a beam hits a stationary target ("fixed target experiments") the luminosity has usually a simple form. Assuming that the transverse size of the beam is much smaller than that of the target, it follows from the definition of the cross-section and Eq. 1.1 that

$$\mathcal{L} = \rho l n/\Delta t, \tag{1.2}$$

where ρ is the number of target particles per unit volume (ρ is assumed to be constant throughout the target), l is the length of the beam path within the target and n is the number of beam particles hitting the target in a time interval Δt. In such a case the luminosity measurement just requires the measurements of ρ, l and the flux of the incident particles, $N/\Delta t$.

Typical values of the luminosity reached in fixed target experiments are $10^{37}cm^{-2}s^{-1}$. For example, with a 1m long target of liquid hydrogen and a beam intensity of $2.5 \times 10^{12} particles/s$ (as was available at the SpS at CERN) the corresponding $\mathcal{L}$ is $5 \times 10^{36}cm^{-2}s^{-1}$. Such high luminosities are not achievable with colliding beams. Hereafter, the discussion will deal exclusively with colliders.

The general expression for the luminosity of the collisions of ultra-relativistic beams can be written [7, 8]:

$$\mathcal{L} = f_c\, c^3 \int \frac{p_1 \cdot p_2}{E_1 E_2}\, n_1 n_2\, dt\, dx\, dy\, dz, \tag{1.3}$$

where f_c is the frequency of the beam crossings; c is the speed of light; p_1, p_2 and E_1, E_2 are the four-momenta and energies of the colliding beams; n_1, n_2 are the spatial distributions

of the particles in the beams; x, y, z are the spatial coordinates and t is the time coordinate. The integration is performed over the volume of the interaction region and the time of the collisions.

In the case when the beam particles are bunched (the case for most high energy, accelerators) and the bunches are of Gaussian shape, the particle densities n_1 and n_2 can be described as:

$$n(x,y,z;t) = \frac{N}{(2\pi)^{3/2}\sigma_x\sigma_y\sigma_z} exp\left(-\frac{(x-x_0)^2}{2\sigma_x{}^2} - \frac{(y-y_0)^2}{2\sigma_y{}^2} - \frac{(z-z_0)^2}{2\sigma_z{}^2}\right), \tag{1.4}$$

where N is the number of particles in the bunch; σ_x, σ_y and σ_z are the widths of the particle distributions; and x_0, y_0, z_0 are the coordinates of the center of the beam orbit. In the case that the widths are approximately constant in time of collisions[1], and the beams collide head-on which means that (over the interaction region) $p_1 \cdot p_2/E_1E_2 = 2/c^2$, $x_0 = y_0 = 0$, and $z_0 = ct$ for one beam and $z_0 = -ct$ for the other, the formula for $\mathcal{L}$ can be simplified to

$$\mathcal{L} = \frac{f \sum N_1 N_2}{2\pi\sqrt{(\sigma^*_{x,1})^2 + (\sigma^*_{x,2})^2}\sqrt{(\sigma^*_{y,1})^2 + (\sigma^*_{y,2})^2}}, \tag{1.5}$$

where f is the beam revolution frequency, N_1, N_2 are the numbers of particles confined to a pair of colliding bunches and the sum is over all pairs of bunches. The notation will be used that a star denotes a quantity given at the *interaction point* (IP), e.g. $\sigma^*_{x,1}$ is the horizontal width at the IP. In this case it is often useful to introduce the specific luminosity $\mathcal{L}_{spec} = \mathcal{L} / \sum N_1 N_2$ which is a measure of the geometric properties of the colliding beams.

It is important to keep in mind that Eq. 1.5 is valid under quite restrictive conditions. For non-zero crossing angles (e.g. at the ISR at CERN) or non-Gaussian beam shapes, the formula for the luminosity can be more complicated [9].

1.1.2 Methods of Luminosity Measurement

In practice, two methods are used to measure the luminosity at colliders.

- Method A: if the geometry and particle populations of the colliding beams are precisely known the luminosity can be calculated from Eq. 1.5 or, in more general cases, from Eq. 1.3.
- Method B: if the rate dN/dt of a process can be measured and its cross-section is well known, the luminosity can be calculated from Eq. 1.1.

The luminosity measurement with method A is usually not precise because an accurate measurement of the beam currents and especially of the beam size at the IP is difficult. The precision of the luminosity measurement with method B is limited most often by the uncertainty of the experimental corrections of the measured rate dN/dt. In practice, one method often supplements the other.

[1] In other words, the value of the β-functions do not change considerably over the interaction region; see Sections 1.2.2 and 3.3.4.

Method B is usually used at e^+e^- colliders and the luminosity measurement is based on elastic e^+e^- Bhabha scattering. For example, in the ALEPH experiment at the LEP collider the luminosity is measured with a precision better than 1%, of which 0.3% is due to the theoretical uncertainty in calculation of the Bhabha cross-section, and 0.6% is due to experimental systematic errors [10]. To-date, the highest luminosity at e^+e^- colliders has been achieved at the CESR storage ring at Cornell where $\mathcal{L}$ equal to $2.5\times10^{32}cm^{-2}s^{-1}$ has been reached with 6 GeV beams and 180 mA total beam currents.

For hadron pp ($\bar{p}p$) high energy colliders the process of elastic electromagnetic $p(\bar{p})p \rightarrow p(p)p$ scattering is difficult to measure and therefore method A is commonly used. Beam dimensions are usually measured a few meters from the interaction region and the specific luminosity is derived from the results of a beam transport program. Then, by the measurement of the beam currents the luminosity can be determined (e.g. with the use of Eq. 1.5). This method is not very accurate (8% accuracy at $Sp\bar{p}S$ at CERN [11] and about 11% at Tevatron at Fermilab [12]) but in some cases the precision can be very much improved. For instance, at the ISR pp (and $p\bar{p}$) collider a 0.3% error on the luminosity measurement was achieved [13] with the use of a method developed by S. van der Meer [14]. The ISR machine was an unbunched (coasting) beam collider with non-zero crossing angle, and the formula for its luminosity is [15]:

$$\mathcal{L} = I_1 I_2 / 2ce^2 h_{eff} tan\frac{\alpha}{2}, \tag{1.6}$$

where I_1, I_2 are the total currents in the beams, e is electron charge, h_{eff} is the effective height of the beam collision region and α is the crossing angle. Van der Meer proposed to measure h_{eff} by vertically scanning the colliding beams through one another by vertically displacing one beam, and simultaneously monitoring the elastic pp scattering rate. He observed that h_{eff} is equal to the area under the rate-vs.-displacement curve divided by the rate at zero displacement. This method requires a precise measurement of the beam displacement ($\pm20\mu m$) but was very successful. The highest luminosity for hadron colliders of $1.4\times10^{32}cm^{-2}s^{-1}$ was obtained at the ISR with 31 GeV proton beams and 10 A beam currents.

At the ep collider HERA the luminosity measurement is based on method B using the reaction $ep \rightarrow e'\gamma p'$.

1.2 The HERA - ep Collider

1.2.1 Basic Collider Physics

As mentioned above the luminosity of a collider is determined by the geometry of the beams, the population of particles within the beams, and the revolution frequency. In this section the meaning and limits of essential accelerator parameters will be discussed briefly. We restrict the discussion to proton and electron synchrotrons only.

The construction of high energy colliders currently follows a standard scheme: a multi-stage pre-acceleration system feeds the bunched beams to the main ring, where the particles are accelerated in RF (Radio Frequency) cavities in a synchronous mode, in which the frequency (and the magnetic field) are changed in accordance with the increasing speed

of the particles, and the radius of orbit is kept constant. To obtain high beam current densities and high luminosities the technique of alternating gradient focusing is applied. This method was invented by N.C.Christofilos, E.Courant, M.Livingstone and H.Snyder [16] in the 1950's and utilizes the focusing properties of an array of focusing and defocusing lenses (quadrupole magnets) interspersed with (direction-changing) prisms (dipole magnets). This resulted in the development of *storage rings*, in which beams could be stored for hours.

For the operation of a storage ring to be effective, beams with long life-times are required. Excellent vacuum systems are needed so that the beam losses due to interactions of the beam particles with the molecules of residual gas are acceptable. Typical residual gas pressures are $10^{-6}mbar$ in one beam synchrotrons and down to $10^{-12}mbar$ in colliding beam storage rings [17].

The motion of a beam particle in a storage ring is described with respect to the motion of an ideal particle with the nominal energy travelling on the design orbit. The motion is described in a curved coordinate system where the longitudinal coordinate s measures the position of the particle along the design orbit and x, y, z measure the horizontal, vertical and longitudinal displacements of the particle with respect to that orbit [18, 19]. To a good approximation, the description of the tranverse and longitudinal (time, energy) motions can be considered separately[2].

The transverse motion of beam particles of nominal energy with respect to the ideal trajectory is called *betatron motion*. The equation of motion in one transverse dimension (horizontal - same for vertical) is

$$\frac{d^2x}{ds^2} = \frac{eg_x(s)}{\gamma mc}x = k_x(s)x, \tag{1.7}$$

where $g_x(s)$ is the quadrupole gradient (with units of T/m), m is the particle mass, and γ is the Lorentz factor. In focusing quadrupoles[3] $k(s) < 0$, in defocusing quadrupoles $k(s) > 0$, and in gradient free regions $k(s) = 0$ [4]. This equation describes an oscillatory motion, *betatron oscillations*, and if one assumes a solution of the form

$$x = A_x\sqrt{\beta_x(s)}\exp i\psi_x(s), \tag{1.8}$$

where β (the beta-function) describes the amplitude and ψ the phase of the oscillations, then Eq. 1.7 splits into two equations:

$$\frac{1}{2}\frac{d^2\beta_x}{ds^2}\beta_x - \frac{1}{4}\left(\frac{d\beta_x}{ds}\right)^2 - k_x(s)\beta_x^2 = 1 \tag{1.9}$$

and

$$\frac{d\psi_x}{ds} = \frac{1}{\beta_x}. \tag{1.10}$$

[2]Any "coupling" between the transverse and longitudinal motions, for example the dispersion, is neglected here.

[3]If a quadrupole focuses in a horizontal plane, then it defocuses in a vertical plane, and vice versa, i.e. $k_x = -k_y$.

[4]At a distance s from the IP, in a drift space before first quadrupole, $\beta(s) = \beta^* + s^2/\beta^*$.

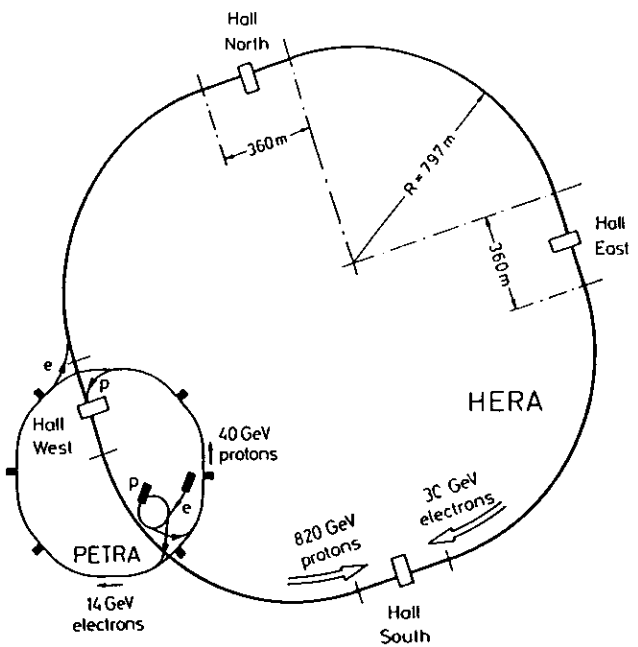

Figure 1.1: The layout of the HERA collider.

completed (without the superconducting RF cavities) and electrons were accelerated up to 14 GeV. In September 1989 the electron beam energy of 27.5 GeV was achieved. In November 1990 the construction of both storage rings was accomplished and the commisioning of HERA started in April 1991. In October 1991 the first electron-proton collisions were observed. By May 1992 the two experiments, H1 and ZEUS, were installed in the interaction regions and data taking started in June 1992. The first results from the experiments were published in September 1992.

The layout of the HERA accelerator is shown in Fig. 1.1 and its basic parameters are collected in Tab. 1.1. The electron and proton beams are guided in separate rings which cross each other in three experimental halls: South, North and East. The electron and proton acceleration and storage systems are quite independent and therefore they can be described separately [21, 22].

The Electron Storage Ring

Electrons are accelerated to 200 MeV in the electron linear accelerator LINAC I and up to 7.5 GeV in the DESY II synchrotron. The electrons are then transferred to the PETRA II synchrotron where their energy is increased to 12 GeV, after which they are

Beam	Proton	Electron
Nominal Energy	820 GeV	30 GeV
Injection Energy	40 GeV	12 GeV
C.M. Energy	314 GeV	
Maximum Q^2	$9 \times 10^4 GeV^2$	
Luminosity	$1.5 \times 10^{31} cm^{-2} s^{-1}$	
Number of Interaction Points	3	
Crossing Angle	0 (head-on collisions)	
Free Space for Experiments	±5.5 m	
Circumference	6336 m	
Bending Radius (main dipoles)	588 m	608 m
Magnetic Field (main dipoles)	4.68 T	0.16 T
Energy Range	300-820 GeV	10-33 GeV
Total Beam Current	163 mA	58 mA
Particles per Bunch	10^{11}	3.5×10^{10}
Maximum Number of Bunches	210	210
Number of Bunch Buckets	220	
Time between Crossings	96 ns	
Beta Functions (β_x^*/β_y^*)	10m/1m	2m/0.7m
Beam Size σ_x^*	0.29 mm	0.26 mm
Beam Size σ_y^*	0.07 mm	0.07 mm
Beam Size σ_z^*	11 cm	0.8 cm
Radiation Energy Loss/Turn	1.4×10^{-10} MeV	70.38 MeV
Maximum Circum. Voltage	0.2-2.4 MV	260 MV
Total RF Power	1 MW	13.2 MW
RF Frequency	50.033/208.13 MHz	499.667 MHz
Tune Shift ξ_x	0.001	0.016
Tune Shift ξ_y	0.00042	0.025
Polarization Time at 30 GeV	-	27 min
Filling Time	20 min	15 min

Table 1.1: Parameters of the HERA storage rings.

In this approximation, the β-function depends only on the configuration of quadrupoles and for storage rings is determined uniquely by Eq. 1.9.

The number of betatron oscillations per revolution, Q_x, is known as the *betatron tune*. It follows from Eqs 1.8 and 1.10 that

$$Q_x = \frac{1}{2\pi}\int \frac{1}{\beta_x(s)}ds. \tag{1.11}$$

To avoid resonance effects this number should not be an integer or a simple fraction.

Oscillations in longitudinal phase space (time vs. energy) are called *synchrotron oscillations*. It can be shown that the angular frequency ω_s of the oscillations scales as

$$\omega_s \sim \sqrt{\omega_{RF}/ET_0}, \tag{1.12}$$

where ω_{RF} is the RF angular frequency, E is the particle energy, and T_0 is the revolution period. The *synchrotron tune*, Q_s, is the number of synchrotron oscillations per revolution, $Q_s = \omega_s T_0/2\pi$. In order to keep a beam particle at the same position with respect to the phase of the accelerating field in succesive turns, T_0 must be equal to $n(2\pi/\omega_{RF})$. The integer n is called the *harmonic number*, which is also the number of bunches the ring can hold.

The transverse emittance of a beam, ϵ_x, is defined as (see Eq. 1.8)

$$\epsilon_x = \langle A_x^2 \rangle, \tag{1.13}$$

where the averaging is over all beam particles. Therefore, the RMS beam size at the position s is

$$\sigma_x = \sqrt{\epsilon_x \beta_x}. \tag{1.14}$$

In a similar way one can define a longitudinal emittance associated with the synchrotron oscillations.

It follows from Liouville's Theorem (LT) [20] that the area occupied by a beam in the $x, \gamma\beta dx/ds$ phase space cannot change in time if there is no energy dissipation (here $\beta = v/c$, and v is the particle velocity). Since the area in the $x, dx/ds$ plane is measured by the transverse emittance ϵ_x, $\gamma\beta\epsilon_x$ is constant while a beam is accelerated, transported down a beam line, etc. whenever LT is valid (for example in proton accelerators). In this case the beam size at the IP is limited by parameters of the ion source and the emittance shrinks with the beam energy as $1/E$. LT is not valid for $e^-(e^+)$ beams if energy losses due to synchrotron radiation play an important role. The radiation of synchrotron photons causes two counteracting effects: on one hand, a damping of the betatron oscillation due to the alternating energy losses and subsequent acceleration in the RF cavities; and on the other, a dilution of the emittance due to the excitation of the oscillations by the radiation of the synchrotron photons. The emittance is determined when the two effects are in equilibrium, which results in a growth of the emittance with the beam energy squared [18, 20].

Collider interaction regions are designed to have small β-functions. A small β-function is important to collider operation for two reasons. First, the transverse size of the collision area $\sigma_x^*\sigma_y^*$ is proportional to $\sqrt{\beta_x^*\beta_y^*}$, and therefore a small β at the IP reduces the collision

area and thus increases the luminosity. Secondly, with small beta functions the beams are less sensitive to the beam-beam effects, discussed in the following paragraph. This is achieved using so-called *low beta insertions*.

The interaction of particles in one beam with the electromagnetic field of the other beam (the "beam-beam interaction") also influences the luminosity value. The quantity characterizing the strength of the beam-beam interaction, ξ, is the beam-beam "tune shift". It measures the shift of the betatron tune due to the beam-beam effect. The ξ parameter can be calculated from the formula [19]:

$$\xi_{x,y} = \frac{r}{2\pi}\frac{N\beta_{x,y}^*}{\gamma(\sigma_x^* + \sigma_y^*)\sigma_{x,y}^*}, \tag{1.15}$$

where r is the classical radius of the beam particle and N is the number of particles in a bunch. A saturation of ξ at large bunch currents has been observed [19]. The empirical limit on ξ measured at the SppS and the Tevatron indicates that $N_{IP}\xi < 0.024$, where N_{IP} is the number of interaction points and ξ is the tune shift from a single IP. At e^+e^- colliders the measured limits on the tune shift vary from 0.01 to 0.07 [19]. For beams with equal bunch sizes and currents and which collide "head-on", Eq. 1.5 can be rewritten in terms of ξ_y as follows:

$$\mathcal{L} = \frac{Nn_b\gamma f\xi_y(N)}{2r\beta_y^*}, \tag{1.16}$$

where n_b is the number of bunches. At low beam intensities ξ_y is proportional to N, thus $\mathcal{L} \propto N^2$. However, ξ_y saturates at large beam currents, and in this case ξ_y is constant and $\mathcal{L} \propto N$. Therefore, accelerators are designed to obtain as high a limit on the tune shift as is possible, and so to increase the maximum available luminosity.

1.2.2 The HERA Collider

HERA (Hadron Electron Ring Anlage) is an unique collider of high energy electrons and protons. It is situated at the DESY (Deutsches Elektronen Synchrotron) laboratory in Hamburg. At HERA the study of the structure of the proton through the use of electron-proton collisions is attainable in a completely new kinematic regime. The center-of-mass energy E_{CM} of 314 GeV and the maximum square of the momentum transfer Q^2 of $\approx 10^5$ GeV^2 are, respectively, over 10 and 100 times larger than the values attained in previous experiments. Such extremely 'hard' collisions make it possible to search for hypothesized electron and quark structure with a resolution as small as 3×10^{-18} cm as well as for new particles which are anticipated by theories which extend the Standard Model of particle interactions. The interesting physics of photon-proton collisions at E_{CM} energies of about 200 GeV, which are equivalent to collisions of 20 TeV photons with stationary protons, can be explored as well. With the use of longitudinally polarized electron beams the search for right-handed currents will also be possible.

The HERA project was authorized in April 1984 after several years of research and design activities. The civil engineering of the accelerator tunnel, 6.24 km in circumference and 10-25 m below ground level, started in 1984. In August 1988 the electron ring was

injected into the HERA electron ring. It consists of 456 main dipoles of 0.16 T bending field and 605 main quadrupoles. In the arcs, the magnets are grouped in 2×11.8 m long units, each of which cointains two dipoles, two quadrupoles, three sextupoles and two correction dipoles. About 90% of the synchrotron radiation produced by the electron beam (at 30 GeV the total radiated power is 7 MW for a beam current of 58 mA) is absorbed by the water cooled copper vacuum pipe. This energy loss is compensated by the acceleration in the RF cavities. The 82 normal conducting copper cavities resonate at 500 MHz. To reach energies over 27.5 GeV 16 superconducting niobium cavities with an accelerating gradient of 5 MV/m are used. Electrons which circulate in a storage ring can become spin polarized due to the radiation of synchrotron photons, which sometimes causes the flip of the electron spin (the Sokolov-Ternov effect). This results in a spin polarization anti-paralell to the bending field. The build-up time of this "natural" vertical polarization decreases with energy and at 30 GeV is about 27 minutes. In August 1992 a transverse polarization of 60% of the 26.7 GeV beam was measured by scattering circularly polarized laser photons off the electron beam [23]. For the study of electroweak currents, longitudinally polarized electrons are required. This will be realized with the use of "spin-rotators", a series of horizontal and vertical bending magnets, installed on each side of the interaction regions. They rotate the spin into the beam direction just before collision and undo this before the beam enters the arc. The maximum longitudinal polarization is expected to be about 80%.

The Proton Storage Ring

H^- ions are accelerated up to 50 MeV in the Proton Linac and then up to 7.5 GeV in the DESY III synchrotron. After stripping off the two electrons, the protons are transferred to PETRA II, accelerated to 40 GeV and injected into HERA. The HERA proton ring consists of 422 superconducting main dipoles of 4.68 T and 224 superconducting main quadrupoles. The 47.08 m long proton ring unit (installed in the arcs) consists of 4 dipoles, 4 quadrupoles, 4 sextupoles and correction coils. To cool the superconducting components of HERA to 4.3 K, about 15 tons of helium circulate in the cooling system. During the injection and acceleration to 300 GeV, the proton RF cavities resonate at 52 MHz. At 300 GeV the 208 MHz RF system, consisting of 4 cavities, is switched on.

As mentioned in Section 1.2.1, low beta insertions are used to achieve high luminosities. In Fig. 1.2 the 'optics' of the electron and proton rings at the North, East and South straight sections are shown [21]. A triplet of electron low-beta quadrupoles (QL, QC and QB) installed close to the IP is followed by a horizontal bending magnet (BH). The quadrupoles are placed slightly off-axis with respect to the orbit of the electron beam, therefore in addition to focusing the electron beam they deflect it with an average bending radius of 1360 m. This group of magnets, called "the electron separator", provides a total deflection angle of 10 mrad and allows for the separation of the electron and proton rings. The protons are focused by a doublet of low-beta quadrupoles (QS and QR) located after the electron separator. Conventional iron magnets (BU) deflect the proton beam upwards to a level 81 cm above the electron ring. The first superconducting magnet is placed about 115 m from the interaction point, away from the direct flux of synchrotron radiation. In Tab. 1.2 the HERA parameters at the interaction point are collected.

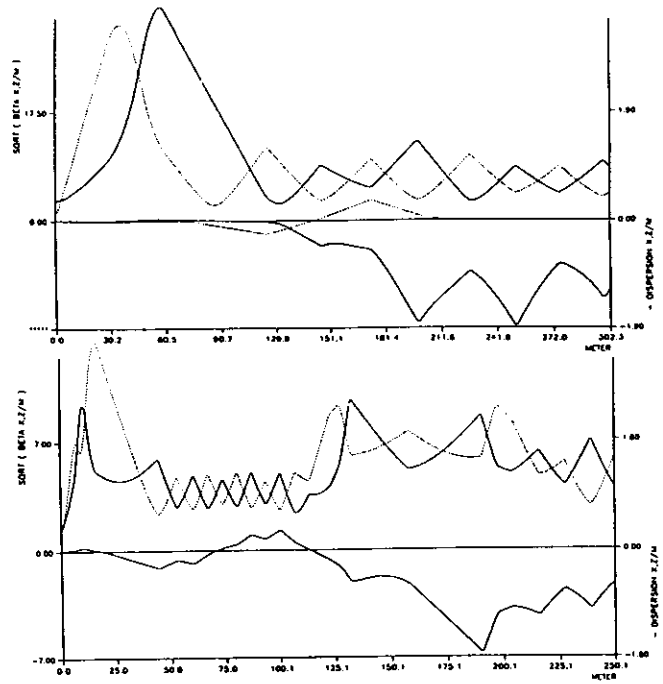

Figure 1.2: The 'optics' in the HERA low-beta sections (upper plot – proton ring, lower plot – electron ring).

Beam		Proton	Electron
Emittance	$\epsilon_x[10^{-8}m \cdot rad]$	1–2	4
	$\epsilon_y[10^{-8}m \cdot rad]$	1-2	(0.07–0.1)ϵ_x
β-function	$\beta_x^*[m]$	7	2.2
	$\beta_y^*[m]$	0.7	1.4
Beam size	$\sigma_x^*[mm]$	0.27–0.37	0.30
	$\sigma_y^*[mm]$	0.08–0.12	0.06–0.07
	$\sigma_z^*[cm]$	≈15	≈0.8
Beam angular divergence †	$\sigma_{x'}^*[mrad]$	0.04–0.05	0.13
	$\sigma_{y'}^*[mrad]$	0.12–0.17	0.04–0.05

†The beam divergences $\sigma_{x'}^*, \sigma_{y'}^*$ are the RMS width of the angular distribution of the beam at the IP and can be calculated from the formula:

$$\sigma_{x',y'}^* = \sqrt{\epsilon_{x,y}/\beta_{x,y}^*} \, .$$

Table 1.2: HERA parameters at the ZEUS IP, October/November 1992.

In Autumn 1991 HERA operated with 26.7 GeV electrons and 480 GeV protons. The number of colliding bunches was gradually increased from one to ten. After the winter 91/92 shutdown the energy of the proton beam was raised to 820 GeV. An additional electron bunch, which did not collide with a proton bunch, a so-called *pilot bunch*, was also stored to allow for background studies.

1.3 The ZEUS Experiment

With the ZEUS detector a wide class of processes which occur in the collisions of high energy electrons and protons can be studied at HERA. One of the main goals of the ZEUS experiment is the precise measurement of the deep inelastic scattering (DIS) of electrons on protons. Due to the imbalanced beam momenta at HERA and the nature of DIS, most of the secondary particles produced in such collisions emerge under small angles with respect to the direction of the primary proton. The study of DIS events requires an excellent identification and measurement of the scattered leptons (e^-, ν_e). Therefore, fine granularity, good hermeticity and good energy resolution of the detectors are vital. The use of high precision tracking and vertex detectors also ensures the capability to fully reconstruct the events (even when particle decays take place). In this way, in addition to *inclusive* measurements of leptons in DIS, which allow one to determine the proton structure functions, many *exclusive* measurements of various reactions can be performed (for example the decays of heavy quarks). So-called soft collisions involving elastic and diffractive scattering of protons and electrons will also be studied with the ZEUS detector. These are measured with the help of detectors designed to measure the small angle electrons and protons. An extensive search for the signals of new phenomena is also performed by the ZEUS collaboration.

The experimental requirements mentioned above and the very short bunch crossing time at HERA of 96 nsec made the design and construction of the ZEUS detector a demanding task. In the section below, the main components of the detector are briefly described.

1.3.1 The ZEUS Detector

The elements of the central ZEUS detector are shown in Figs. 1.3 and 1.4. The following tracking detectors are located in the magnetic field of a thin superconducting magnetic coil: a vertex detector (VXD), a central tracking detector (CTD) and transition radiation detector, and forward and rear[5] tracking detectors (FDET, RTD). A high resolution calorimeter, composed of electromagnetic and a hadronic sections, surrounds the coil over nearly the full solid angle. This calorimeter is surrounded by a backing calorimeter (BAC), barrel and rear muon detectors (BMU, RMU), and a forward muon spectrometer (FMUON). In addition, there are located near the beam line, photon and electron detectors used for the luminosity measurement and detector stations used for the observation of forward scattered protons.

[5]All directions are referred with respect to the proton beam direction.

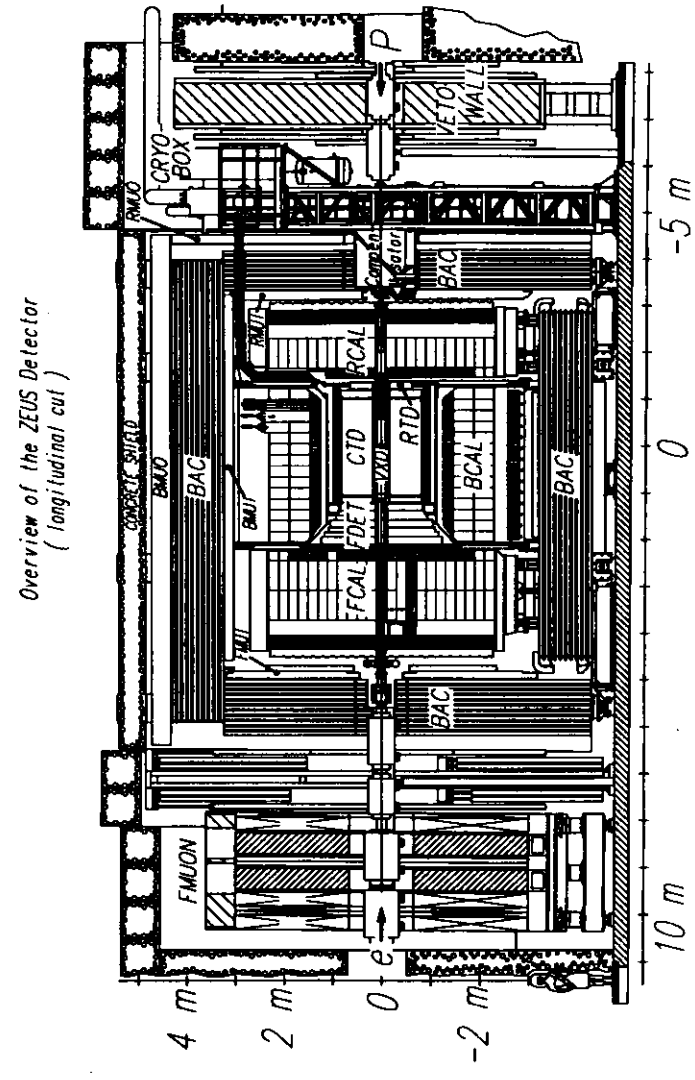

Figure 1.3: The main components of the ZEUS detector.

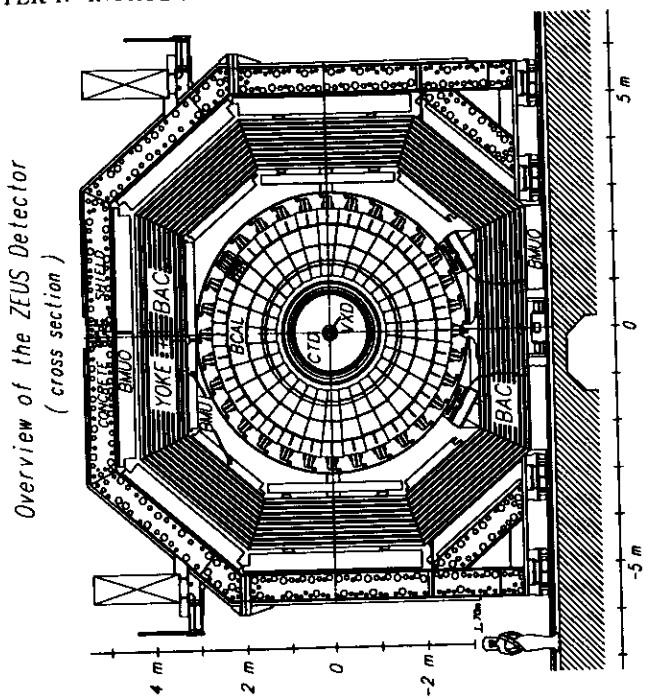

Figure 1.4: The main components of the ZEUS detector (beam direction).

The high resolution sampling calorimeter consists of depleted uranium plates interleaved with plastic scintillator. The three sections of the calorimeter (Forward, Barrel and Rear) are denoted by FCAL, BCAL and RCAL in Fig. 1.3, 1.4. The active area of the FCAL (RCAL) starts at 45 (68) mrad with respect to the beam axis. The solid angle coverage corresponds to 99.8% in the forward hemisphere and 99.5% in the backward hemisphere. Its relative energy resolution measured in beam tests is $0.18/\sqrt{E}$ (E is the energy in GeV of the incident particle in GeV) for electrons and $0.35/\sqrt{E}$ for hadrons [24]. The calorimeter is compensating, with equal mean response to hadrons and electrons of the same energy.

The central tracking detector (CTD) consists of 72 cylindrical drift chamber layers organized into 9 'superlayers'. During the data taking period considered in this thesis only three superlayers were read-out with z-by-timing electronics.

The LUMI monitor, which consists of an electron and a photon branch, is installed in the region between 35 and 108 m downstream from the IP in the direction of the electron beam. The detectors measure the energy and position of the photons and electrons which exit the beam pipes through special thin windows (see Chapter 2).

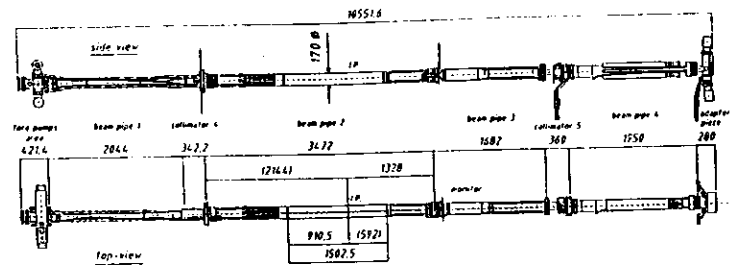

Figure 1.5: The section of the HERA beam pipe in the area of the ZEUS IP.

The HERA beam pipe in the region of the ZEUS IP is divided into three sections: a central 1.48m long beam pipe section with thin walls and two outer sections, which contain five collimators made of tungsten (Fig. 1.5). In the forward end of the straight section two Ti evaporation pumps and two ion-getter pumps are installed; four Ti evaporation pumps and two ion-getter pumps are installed in the rear region of the section. At the position of the fifth collimator, C5, four scintillation counters are installed which surround the beam pipe. They provide an accurate timing signal for the electron and proton bunches. In addition, they can be used to veto showers produced by the proton beam halo.

The majority of the electronics ("front-end electronics") is mounted close to the subdetectors with the remainder located in the Rucksack, a three story building which is moved with the detector.

The mechanical construction of most of the subdetectors was completed in 1990/91. The roll-in to the interaction region was performed in December 1991.

1.3.2 The ZEUS Trigger System

The ZEUS trigger system efficiently selects interesting events and at the same time it suppresses the background rate from its initial value of about 50 kHz down to a few Hz[6]

The architecture of the three-level trigger and data acquisition system is shown schematically in Fig. 1.6. The First-Level Trigger (FLT) sets a trigger rate of about 1 kHz by eliminating most of the beam-gas and beam-halo background. For every bunch crossing the component data are stored in analog or digital pipelines for $5\mu s$ while the FLT calculations are performed. With the use of a subset of the full data and programmable logic the FLT decision is issued after exactly 46 crossings, i.e. 4.4 μs. A positive FLT decision causes the digitized data from the components to be passed onto the Second-Level Trigger (SLT). The SLT has access to a large fraction of the data and, with more time, is able to

[6]The limit on the trigger output rate is set by the rate of writing data on tape, which is limited to 5-8 Hz.

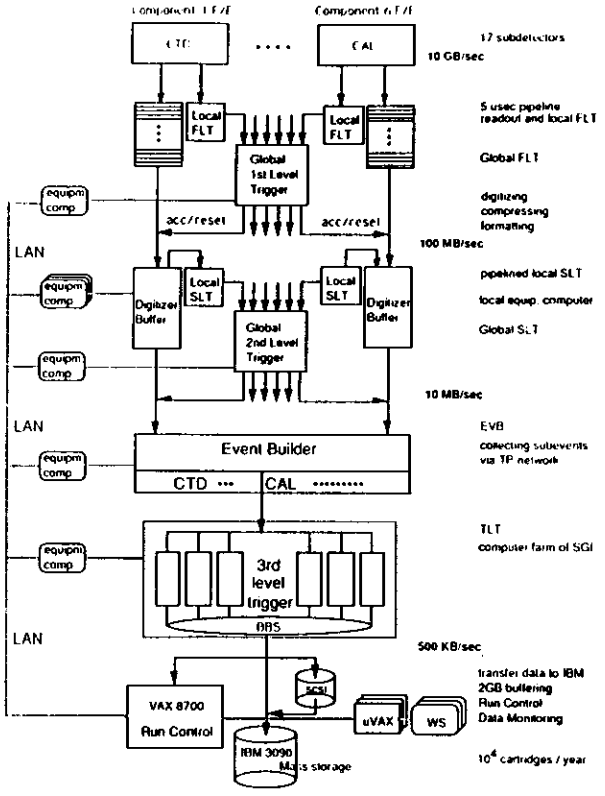

Figure 1.6: The structure of the ZEUS trigger.

perform more complicated calculations than the FLT. This enables the SLT to reduce the FLT output rate of 1 kHz down to about 100 Hz. After a positive decision from the SLT the full data of all subdetectors is collected by the ZEUS Event Builder and is sent to a Third-Level Trigger (TLT) processor farm of Silicon Graphics workstations. The TLT runs a reduced version of the off-line analysis code and reaches an output rate of about 3–5 Hz.

To allow a study of trigger efficiencies and acceptances, loose criteria were used in the trigger system during the early data taking period which is considered in this thesis. This occasionally resulted in a substantial dead time in the system when the background level was high. In the off-line analysis the background contribution was efficiently filtered out by cuts on event timing. In the future, however, a dead time free performance of the ZEUS trigger system is aimed for.

1.4 The Luminosity Measurement in ZEUS

The bremsstrahlung process $ep \to e'\gamma p'$ was chosen for the ZEUS luminosity measurement[7] [1] because:

- its cross-section is large and precisely known from QED,
- it has a clean experimental signature, namely the coincidence of a photon and an electron at small angles with respect to the electron beam axis, with energies which add up to the beam energy: $E_{e'} + E_\gamma = E_e$ (Fig. 1.7).

The bremsstrahlung cross-section was first calculated by H.Bethe and W.Heitler [26]. Their formula for the differential cross section $d\sigma/dE_\gamma$ for ultra-relativistic electrons ($E_{e'}$, $E_e \gg m_e$) scattering on protons with energy E_p is:

$$\frac{d\sigma_{br}}{dE_\gamma} = 4\alpha r_e^2 \frac{E_{e'}}{E_\gamma\, E_e}\left(\frac{E_e}{E_{e'}} + \frac{E_{e'}}{E_e} - \frac{2}{3}\right)\left(\ln\frac{4E_pE_e\,E_{e'}}{m_pm_eE_\gamma} - \frac{1}{2}\right), \qquad (1.17)$$

where α is the fine structure constant, r_e is the classical radius of the electron, and m_e, m_p are the masses of the electron and proton. The cross-section for ep bremsstrahlung cannot be calculated exactly in QED because the proton structure cannot be derived from the theory. Extensive studies have shown that the Bethe-Heitler formula derived with the assumption that the proton is a static, pointlike and spinless object agrees within 0.2% with the results derived utilizing proton structure functions, including the effects of proton recoil [27], and also with the results which take into account Z boson exchange [28]. For example, the total cross-section obtained by integration of Eq. 1.17 over $8 < E_\gamma < 14\ GeV$ is only 0.23% larger than the corresponding cross-section obtained by Gaemers and van der Horst in [27] and 0.24% larger when the integration is performed over $1 < E_\gamma < 30\ GeV$ [28]. In both cases the values $E_e = 30\ GeV$ and $E_p = 820\ GeV$ were assumed and all calculations were done at the Born level.

[7] The luminosity measurement based on the bremsstrahlung process was recently tested at LEP e^+e^- collider with the use of a single photon counter [25].

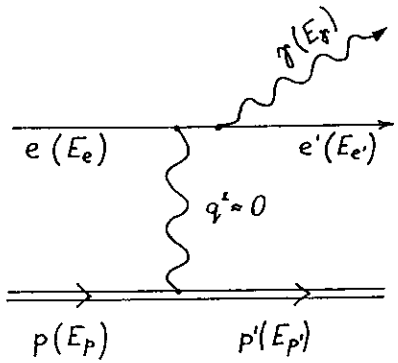

Figure 1.7: Feynman diagram of electron-proton bremsstrahlung.

M. van der Horst [29] has estimated that the cross-section for inelastic $ep \rightarrow e'\gamma X$ bremsstrahlung is $\approx 10^5$ times smaller than that of elastic bremsstrahlung, and so we shall neglect the former in the calculations of the cross-sections for the luminosity measurement.

Higher order corrections to $ep \rightarrow e'\gamma p'$ have also been considered. M. van der Horst [30] showed that virtual photon loop corrections and soft radiative corrections partially cancel each other, resulting in an overall correction of about -0.2% for the assumed experimental cuts. In practice, however, different kinematic cuts may be applied, and therefore this correction should be checked for each particular setup.

The results of the above studies show that the Bethe-Heitler cross-section obtained purely from QED (Eq. 1.17) is accurate at the 1% level. Therefore, this formula and other QED results obtained at the Born level can be used without contributing significantly to the systematic error of the luminosity measurement[8].

The final state electrons and photons produced in bremsstrahlung emerge under very small angles with respect to the direction of the primary electron, and with balancing transverse momenta. To a good approximation the differential cross-section $d\sigma/d\theta_\gamma$ can be written in the form [31]:

$$\frac{d\sigma}{d\theta_\gamma} \propto \frac{\theta_\gamma}{((m_e/E_e)^2 + \theta_\gamma{}^2)^2}, \tag{1.18}$$

where θ_γ is the angle between the momenta of the primary electron and the bremsstrahlung photon. The typical value of θ_γ is m_e/E_e which for $E_e \approx 30\ GeV$ is much smaller

[8]Formulae for bremsstrahlung differential cross-sections calculated under different approximations can be found in [31].

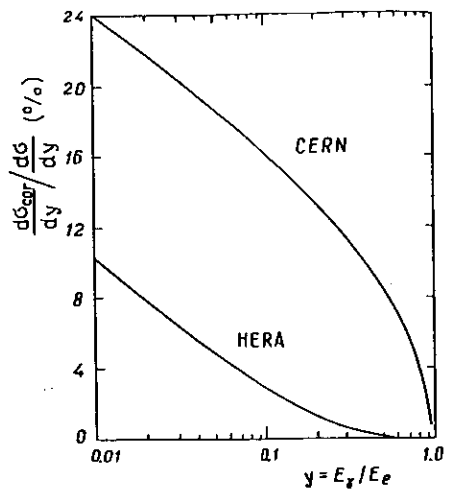

Figure 1.8: The beam size effect at HERA and LHC [7].

than the expected angular divergence of the electron beam at the IP [9](see section 1.2.2). Thus one can determine the electron beam divergence at the IP by measuring the angular distribution of the bremsstrahlung photons. The typical final state electron scattering angle is $m_e/E_{e'}$ and for high energy electrons this angle is also small compared with the widths $\sigma^*_{x'}$ and $\sigma^*_{y'}$.

The energy exchanged between the primary electron and proton is very small, of the order of m_e^2/m_p, and so to a very good approximation $E_e = E_{e'} + E_\gamma$. The transverse momenta of the exchanged virtual photons are also small, with values as low as $10^{-12}\ GeV/c$. Events with very small momentum transfers are suppressed due to the finite transverse dimensions of the colliding beams. This can be understood qualitatively when bremsstrahlung is treated, in the quasi-classical Weizsäcker-Williams model, as the Compton scattering of the virtual photons, which form a cloud around each proton, on the beam electrons. The range of the virtual photons increases with $1/E_\gamma$ therefore the distribution of soft photons is larger than the transverse dimensions of the electron beam. The resultant suppresion of the bremsstrahlung rate due to the finite transverse beam sizes is called the *beam size effect*. It was first observed at the Novosibirsk VEPP-4 e^+e^- collider [32] and was theoretically explained soon afterwards [33]. Results of calculations of this effect based on the wave-packet formalism for HERA and LHC (Large Hadron Collider) colliders are shown in Fig. 1.8. At HERA the effect is less than 3% for $E_\gamma > 3GeV$ but at an LHC ep collider it would be much more pronounced.

In Table 1.3 the integrated cross-sections σ in different photon energy intervals are shown together with the corresponding bremsstrahlung event rates, R_{br}, for the HERA

[9]For E_e =30 GeV one expects $\sigma^*_{x'} = 0.14\ mrad, \sigma^*_{y'} = 0.11\ mrad$ and $\langle\theta_\gamma\rangle \approx 0.017\ mrad$.

Process type and assumed HERA parameters		Photon Energy Range		
		0.1–30 GeV	1–30 GeV	8–14 GeV
ep bremsstrahlung	σ[mb]	336.9	174.0	24.66
$\mathcal{L} = 1.5 \times 10^{31} cm^{-2} s^{-1}$	R_{br}[Hz]	5.05×10^6	2.61×10^6	3.70×10^5
E_e =30GeV,E_p =820GeV	$\langle N_{br} \rangle$	0.509	0.263	0.037
egas bremsstrahlung	σ[mb]	1739.1	960.4	141.8
$I_e = 58mA, p = 10^{-9} mbar$	R_{br}[Hz]	1.88×10^5	1.04×10^5	1.54×10^4
E_e =30GeV,$\langle Z \rangle = 4.2$	$\langle N_{br} \rangle$	0.019	0.011	0.0016

Table 1.3: **Bremsstrahlung cross-sections and rates at HERA.**

nominal luminosity. The scattering rates are high due to the large cross-section. As a result, the statistical error of the luminosity is negligible even for measurements lasting only one minute. However, the probability for more than one event occuring in the same bunch crossing (the "pileup effect") is also high. The pileup effect is directly related to the average number $\langle N_{br} \rangle$ of bremsstrahlung events per bunch crossing which is also given in Table 1.3. It can be seen that for the nominal luminosity the effect is large and cannot be neglected.

One background to ep bremsstrahlung is *egas* bremsstrahlung, the bremsstrahlung of the beam electrons on the residual gas molecules in the beam pipe. It has the same signature as the ep process and a similar differential cross section, which can be seen in Fig. 1.9 where the ep and *egas* bremsstrahlung photon energy distributions, generated with the BREMGE Monte Carlo generator [34], are shown. As a result, this background cannot be recognized on an event-by-event basis and has to be subtracted statistically, utilizing an independent measurement of the contribution of *egas* bremsstrahlung. For this purpose electron pilot bunches, which do not have matching proton bunches, are used. The difference between the shapes of the differential cross-sections $d\sigma/dE_\gamma$ for ep and *egas* bremsstrahlung has an origin similar to the beam-size effect: *egas* events with small momentum transfer are suppressed due to the fact that the atomic nuclei, which are the scattering centers for beam electrons, are screened at distances larger than the atom size by the atomic electrons and have a null effective charge. For the ultra-relativistic HERA electrons the case of "full screening" applies [31].

For a rest gas pressure p of 10^{-9} *mbar* the contribution of the *egas* bremsstrahlung events is a function of the composition of the gas and its pressure distribution along the beam pipe and is expected to be about 2–10% of the total bremsstrahlung rate. In Table 1.3 the *egas* bremsstrahlung cross-sections, rates and $\langle N_{br} \rangle$ are presented for a mean Z of 4.2 (corresponding to a mixture of 90% H_2 and 10% CO_2), a uniform gas distribution and an effective source length[10] of 11 m.

[10]The source length is determined by the acceptance of the bremsstrahlung photons and is close to the length of the ZEUS beam pipe section, described in section 1.3.1.

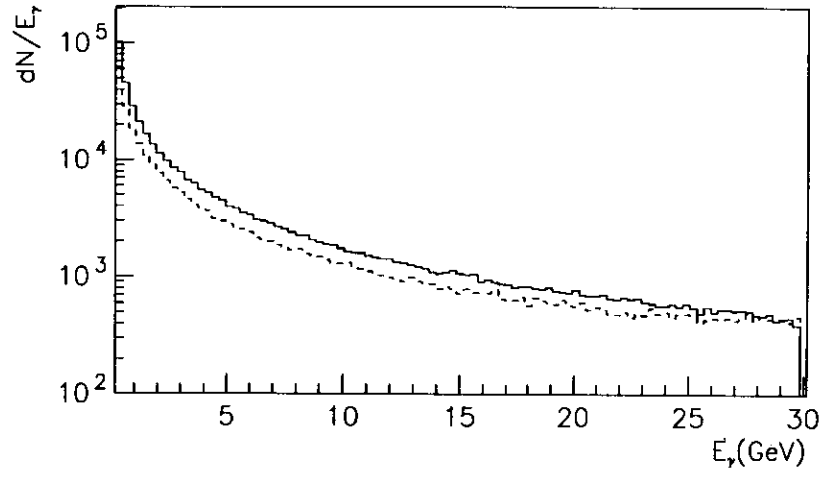

Figure 1.9: **The photon spectra of *ep* (solid line) and *egas* (dashed line) bremsstrahlung from the Monte Carlo generator BREMGE.**

Chapter 2

The ZEUS Luminosity Monitor

2.1 Introduction

The determination of the luminosity in the ZEUS experiment is based on the measurement of the electrons and photons from the reaction $ep \rightarrow e'\gamma p'$. The secondary electrons with energies lower than the beam energy are deflected from the nominal orbit by the magnet system, and can leave the vacuum pipe through a thin window installed about 27 m from the interaction point (IP) (Fig. 2.1). The bremsstrahlung photons, are not deflected by the magnetic field and can leave the vacuum pipe through a window about 92m from the IP. The geometric acceptances[1] for photons and electrons are less than 100%. The acceptance of photons is energy independent and is about 98% under 'normal' conditions, i.e. with the electron beam axis not tilted, the nominal angular dispersion of the beam, etc. In contrast, the electron acceptance is energy dependent and is non-zero in the range $0.2E_e < E_{e'} < 0.8E_e$. In the range $0.35E_e < E_{e'} < 0.65E_e$ the electron acceptance is over 70%.

The detector of the bremsstrahlung events – the LUMI monitor – is naturally divided into two parts, the photon and the electron branches which measure the energy and position of the bremsstrahlung photon and electron, respectively.

The photon branch (Fig. 2.2), consists of a 1.5 mm thick exit window (90% copper, 10% beryllium) and in sequence: a carbon filter, an air filled threshold Čerenkov counter and a lead-scintillator sampling calorimeter, γcal , with a position detector utilizing scintillator 'fingers' inserted at a depth of 7 radiation lengths[2] (7 X_0). The detectors are situated approximately 20 m behind the window. The carbon filter, with an adjustable thickness, reduces the flux of synchrotron photons down to a negligible level. The Čerenkov counter can be used to veto events in which a bremsstrahlung photon has converted to an e^+e^- pair in the carbon filter. Utilizing the 22 X_0 deep calorimeter the energy is measured with a resolution $\sigma_E/E = 0.185/\sqrt{E}$ (E is the photon energy in GeV), and the position of the photons is measured with the position detector with a resolution of about 2 mm.

[1]The geometric acceptance is defined as the probability that a photon (an electron) leaves the beam pipe through the dedicated window.

[2]The radiation length X_0 is the distance in a material (in cm or in g/cm^2) in which a high energy electron loses all but $1/e$ of its kinetic energy by bremsstrahlung.

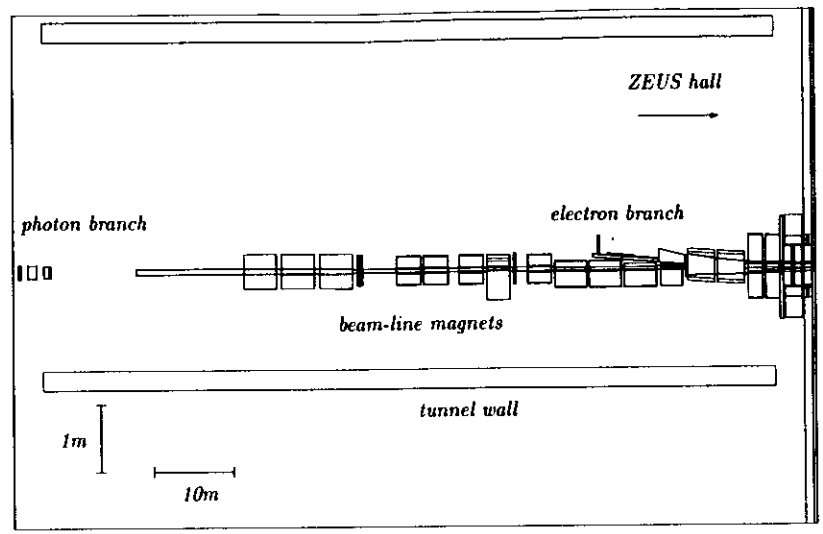

Figure 2.1: The layout of the ZEUS LUMI monitor as simulated with the GEANT program; shown is a horizontal cross-section through the HERA tunnel.

The electron branch is composed of the following components: a 1.5 mm thick steel exit window and, approximately 7 m downstream, the 21 X_0 deep lead-scintillator calorimeter, e^-cal , with similar energy resolution as γcal and with a similar position detector[3] at a depth of 7 X_0 (Fig. 2.2). A scintillator finger is placed, for calibration purposes, in front of the calorimeter.

Both calorimeters are installed on movable, remotely controlled tables. During injection and tests of the electron beam the calorimeters are moved into parking positions about 0.7 m from the beam pipes.

As was shown in section 1.4 the rate of hard bremsstrahlung events ($E_\gamma > 1GeV$) is expected to be over 10^6 $events/s$ with the nominal luminosity. As a result, the detectors absorb large amounts of energy during their operation, which requires good radiation hardness of all detector components as well as continuous monitoring of the calibration. The high rates also require an efficient dead time free data acquisition system.

An inventory of the luminosity monitor components is given in the Appendix and each component of the LUMI monitor is described separately below.

[3]In the data taking period considered here the electron position detector was not installed and the e^-cal had a depth of 23 X_0.

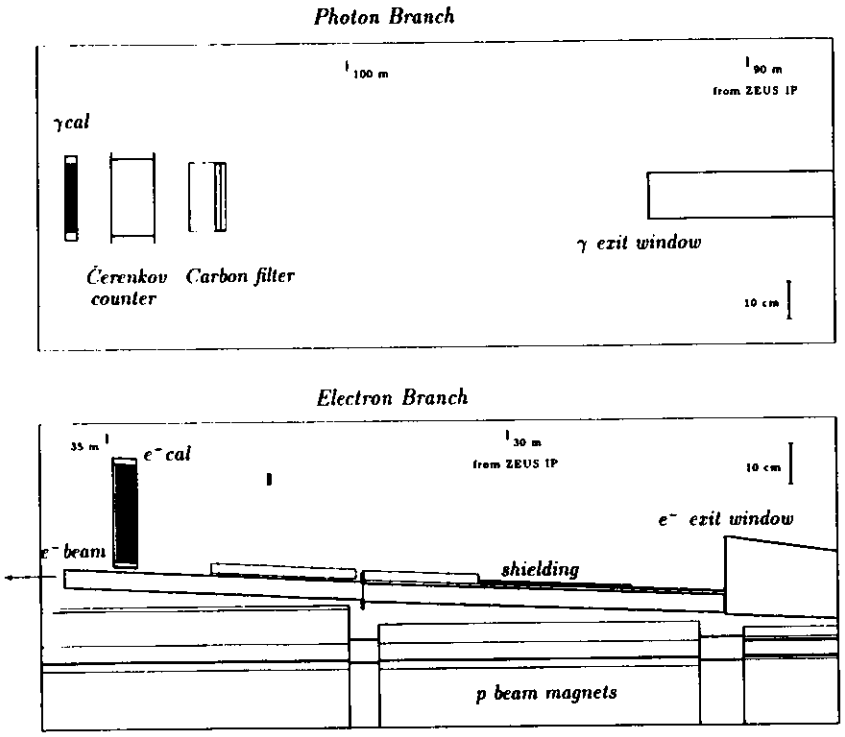

Figure 2.2: The photon and electron branches shown in horizontal cross-sections (from GEANT).

2.2 The Detectors

2.2.1 The Calorimeters

The Energy Measurement

The calorimeters used in high energy physics are detectors devised to measure the kinetic energy of incident particles by converting it into detectable atomic excitations and ionizations. In the case of electromagnetic calorimeters, the incident particles are electrons and photons which develop electromagnetic cascades inside the detectors while the atomic and molecular de-excitations are converted into electrical signals. The longitudinal shape of the cascade is usually measured in units of radiation lengths, X_0. It depends on the energy of the incident particle and on the atomic number of the absorber only logarithmically (Fig. 2.3). The lateral profile of the cascades scales approximately with the Molière radius, R_M. For materials with medium and high atomic numbers ($12 < Z < 93$), $R_M \approx 7A/Z(g/cm^2)$, where A is the atomic mass.

There are two classes of calorimeters, *homogeneous* and *sampling*. Homogeneous calorimeters are made entirely from active material, i.e. the signal (e.g. visible light) is collected from the entire volume of the calorimeter. Lead-glass, BGO and NaI crystal calorimeters are the most popular types of homogeneous calorimeters. Sampling calorimeters are made of layers of passive material, which absorb most of the incident energy, interspersed with layers of active material. These calorimeters detect only a fraction of the total incident energy (*sampling fraction*).

In a sampling electromagnetic calorimeter the energy resolution, σ_{cal}, can be parametrized as [35]

$$\sigma^2_{cal}(E) = \sigma_0^2 + \sigma_1^2 E + \sigma_2^2 E^2, \tag{2.1}$$

where E is the energy of the incident particle; σ_0 is an energy independent contribution, usually noise in electronics; σ_1 is mainly determined by fluctuations of the sampling fraction (*sampling fluctuations*); and σ_2 is caused by non-uniformities and cracks in the construction. Instrumental effects may also contribute to σ_1. For example, in the case of read-out systems which utilize photomultiplier tubes (PMTs), the fluctuations in the number of photoelectrons produced in the photocathode of the PMT, N_{pe}, appear due to the limited number of photons which are produced in the scintillator and which reach the PMT photocathodes. Since the fluctuations in N_{pe} are governed by Poisson statistics, the width, σ_{pe}, scales with the incident energy as $\sqrt{E}$ [4]. Therefore, in the case when σ_0 and σ_2 are small, the calorimeter energy resolution can be written as

$$\sigma_{cal} = \sigma_1^2 E = \sigma^2_{smpl} + \sigma^2_{pe}. \tag{2.2}$$

Construction and Front-end Electronics

The γcal and $e^- cal$ sampling calorimeters have a very similar construction. They differ mainly in their transverse dimensions ($250 \times 250 mm^2$ for $e^- cal$ and $180 \times 180\ mm^2$ for

[4] This follows from $\sigma_{pe} \propto \sqrt{N_{pe}}$ (Poisson statistics) and $N_{pe} \propto E$ (calorimeter linearity).

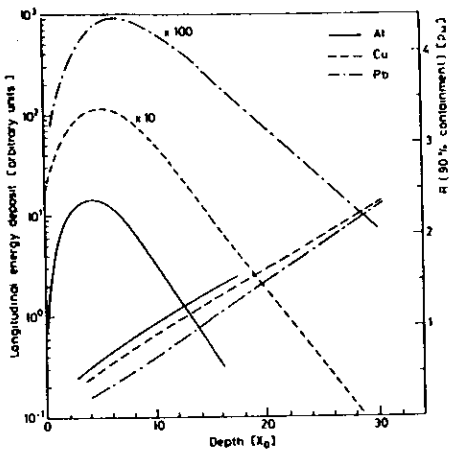

Figure 2.3: The longitudinal profiles and lateral containments of electromagnetic cascades in various materials, from [35].

γcal) and in the details of the insertions of the position detectors. Each calorimeter is made of 5.7 mm lead plates (1 X_0) interleaved with 2.6 mm plates of the scintillator SCSN-38 from KIOWA, which is also used in the ZEUS uranium calorimeter. An additional lead plate (thickness 1 X_0) is located in front of the γcal to increase the shielding against synchrotron radiation. The light generated in the scintillator is collected by Y-7 wavelength shifter (WLS) plates. (There are two such plates in each calorimeter, on the left and right sides of e^-cal , and on the top and bottom of γcal .) The light is then transported through light guides directly onto the PMTs. The 10-stage photomultipliers XP2011 Philips are powered by passive voltage dividers.

The anode voltages are rather low, about 1000 V, to avoid large currents through the PMT anodes as a result of the high event rates. Still, mean anode currents of 10 μA are expected for the design luminosity, which can cause a systematic change of the PMT gains [36]. To maintain a good performance a continuous monitoring of the gains is required. The PMT signals, after a tenfold amplification, are driven through 20 m long cables to the inputs of 8 bit charge-sensitive FADC (Flash Analog-to-Digit Converter) cards which are installed in an electronics rack under the HERA tunnel floor. The signals have a full width at half maximum (FWHM) of about 30 nsec and are integrated within a 50 nsec gate. The charge sensitivity of the FADC card is about 1 pC/channel.

A number of test circuits are also installed, for example LED pulsers and charge injectors, in order to check the performance of each part of the electronics, and as an aid in diagnostics.

Measured parameters	e^-cal	γcal
$\sigma_1(GeV^{1/2})$	0.19 ± 0.05	0.185 ± 0.005
$\lambda(cm)$	83 ± 5	60 ± 5
$\langle N_{pe}\rangle^\dagger$	120 ± 20	150 ± 20

† Average value for a 1 GeV particle.

Table 2.1: Performance of the γcal and e^-cal calorimeters.

Performance of the Detectors and Beam Tests

Lead-scintillator sampling calorimeters with PMT readout were chosen for the energy measurement for the following reasons: 1) fast response, well below the HERA crossing time of 96 nsec, 2) good radiation hardness, 3) good energy resolution, 4) low cost and easy maintenance.

The fast response of the calorimeters is guaranteed by the short decay time of the SCSN-38 scintillator signal (2 nsec) and by the use of fast PMTs (the rise time of the XP2011 signal is ≈2.5 nsec [36]).

For the nominal luminosity the photon calorimeter will absorb about $2 \times 10^7 GeV$ per second and the electron calorimeter about 50% less. We expect the energy deposited at the most irradiated point of the scintillator to be about 1 Mrad per year for both calorimeters (a HERA year is equal to $10^7 s$). The scintillator shows a 5% decrease in light yield and a 15–20% shortening of the attenuation length after an irradiation of 1 Mrad [37]. Since there have been no observed effects of dose rates in a range 3–100 krad/hour, we do not expect different behaviour of the scintillator for the nominal dose rates in the LUMI calorimeters of 0.4 krad/h. Therefore the calorimeters are expected to perform well for a couple of years at the nominal HERA luminosity, providing that the radiation damage and calibration are carefully monitored.

The EGS4 package [38] has been used to simulate the performance of the calorimeters. The sampling fraction is found to be about 0.04 and the sampling fluctuations, σ_{sampl}, is $0.17\sqrt{E}$. The photostatistics fluctuations, σ_{pe}, was determined experimentally from the width σ_{u-d} (σ_{l-r}) of the distribution of the difference between the signals from the two PMTs of the calorimeter (up and down of γcal , left and right of e^-cal) at a fixed beam energy. The photostatistics can be also determined with the use of LED (Light Emitting Diode) tests. Typically, σ_{pe} equals $0.08\sqrt{E}$ which corresponds to an average yield of 150 photoelectrons for 1 GeV of incident energy. Thus, the total energy resolution σ_{cal} is expected to be $(0.17 \oplus 0.08)\sqrt{E} = 0.185\sqrt{E}$.

The performance of the calorimeters was experimentally verified in several test beam measurements [39, 40, 41]. In Fig. 2.4 the mean energy measured with e^-cal , $\langle E_{meas}\rangle$, is plotted as a function of the beam energy, E_{beam}. The ratio $(\langle E_{meas}\rangle - E_{beam})/E_{beam}$, shown also in Fig. 2.4, measures deviations from a perfect linear behaviour. In the electron energy range between 1 and 6 GeV the linearity of the calorimeters was found to

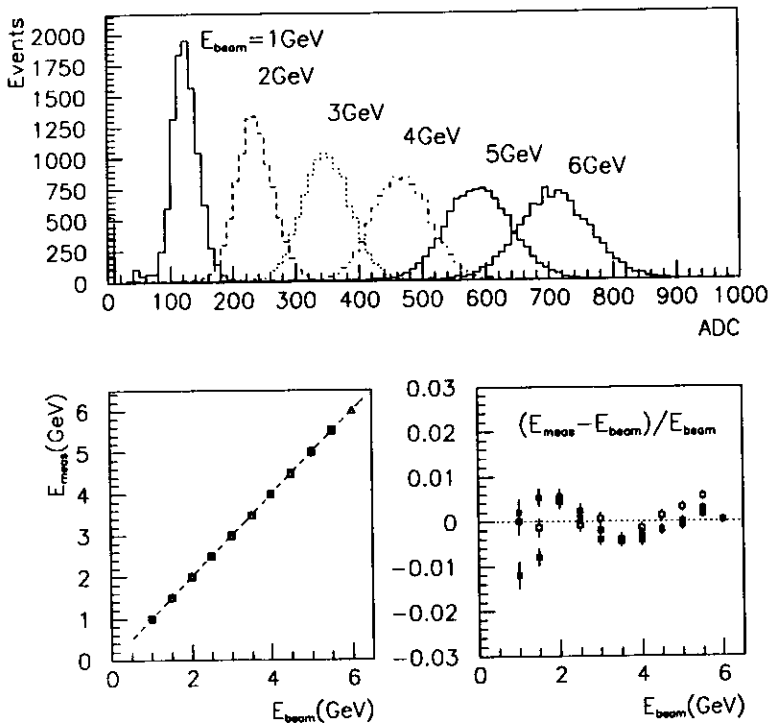

Figure 2.4: Distributions of the e^-cal response for various beam energies; plots of the e^-cal linearity (E_{meas} *vs.* E_{beam}) and of the deviation of the response from the linear behaviour.

Uniformity level	e^-cal		γcal	
	horizontal	vertical	horizontal	vertical
±1%	±9cm	±5cm	±3cm	±6cm
±3%	±11cm	±7cm	±5cm	±7cm

Table 2.2: The fiducial dimensions of the calorimeters.

be approximately 0.5–1%.

The energy resolution and uniformity of the calorimeters were also measured in test beams. The measured resolutions agree with the results of the MC simulations (see Fig. 2.5, Table 2.1). To check the uniformity of the calorimeters (i.e. the sensitivity of the calorimeter response, at a fixed beam energy, to the transverse position of the incident particles) the average measured energy can be plotted as a function of the distance, Δx or Δy, of the beam axis from the center of the calorimeter (Fig. 2.5). The fiducial volumes of each calorimeter are set by upper limits in the deviations of $\langle E_{meas}\rangle$ from the average value measured at the calorimeter center (see Table 2.2).

The light produced in the scintillator is attenuated as it propagates to the PMTs through the scintillator, wavelength shifter plates, and light-guide bars. The effective attenuation length in the scintillator, λ, can be found by measuring the ratio (E_1/E_2) of the signals detected in the two read-out channels as a function of the transverse distance between the beam axis and the calorimeter center. Assuming an exponential attenuation with position, one finds

$$ln\frac{E_1}{E_2} = \frac{2\Delta z}{\lambda}, \tag{2.3}$$

where z is x (or y) for e^-cal (or γcal). In Fig. 2.6 the measured values of $ln(E_1/E_2)$ are shown as a function of Δx. The attenuation length λ was found by fitting the experimental results with Eq. 2.3, and the results are shown in Table 2.1. To minimize the effects of this attenuation on the energy measurement, the energy is calculated by a geometrical average of the two readouts, $E = \sqrt{E_1 E_2}$.

2.2.2 The Position Detectors

DESIGN CONSIDERATIONS

The position detectors measure the horizontal and vertical position of the final state photons and electrons at large distances from the IP, and so help to determine the scattering angles. The bremsstrahlung photons follow the direction of the primary electrons with an angular spread of about 0.017 mrad (see Section 1.4) which corresponds to a spot of about 2 mm radius at the position of the photon calorimeter, 107 m from the IP. This spread limits the accuracy of the measurement of the direction of the primary electron, and so determines the useful resolution of the position detector. The measurement of the electron scattering angle is also limited by the angular divergence of the electron beam [43].

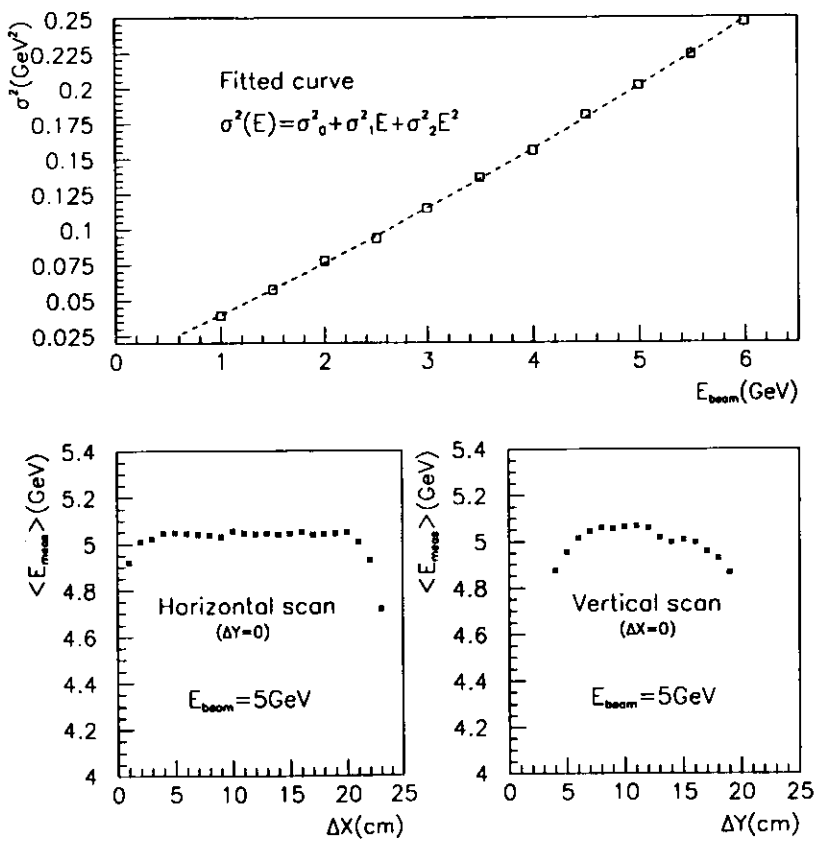

Figure 2.5: **Results of the measurements of the energy resolution and uniformity of** e^-cal .

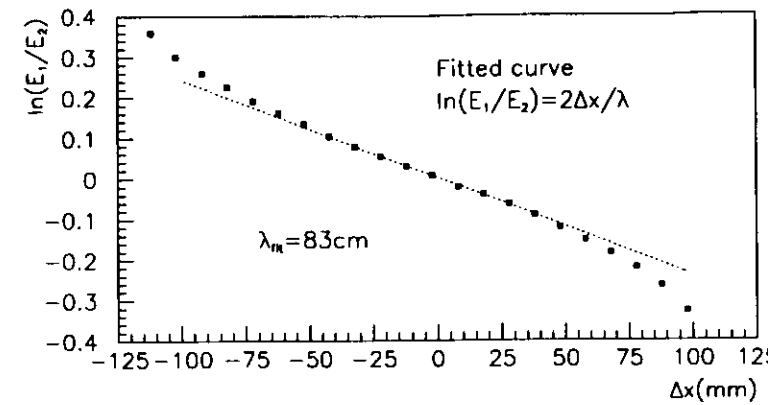

Figure 2.6: **Measurement of the** e^-cal **effective attenuation length,** λ.

The design requirements for the position detectors can be summarized as follows: 1) a spatial resolution of 1-2 mm, 2) the capability to operate with high signal rates ($\approx 10^6$ *events/s*) and fast response (less than 96 ns), 3) good radiation hardness - the detectors should tolerate energy deposits due to ionizing radiation over 1 *Mrad* and neutron fluences[5] of about 10^{13} *neutrons/cm²/year*.

The large neutron fluences prohibit the use of so-called "silicon pads" for the position measurements. Satisfactory results were obtained in tests of a detector consisting of 8 scintillator fingers read-out by P-I-N photodiodes and placed after 5 X_0 of lead [42]. The position of the incident particle was measured by the 'center of gravity' of the electromagnetic cascade [45]. This type of detector is utilized in the LUMI monitor.

Construction and Front-end Electronics

A sketch of the mechanical construction of the LUMI position detectors is presented in Fig. 2.7. The position detectors are inserted in γcal and e^-cal at a depth of 7 X_0, near maximum of the shower development in the calorimeters (see Fig. 2.3). Each detector is composed of two crossed planes of NE110 scintillator fingers for the measurement of the vertical and horizontal positions. The photon (electron) detector consists of 16 (16) vertical fingers of $10 \times 10 \times 143$ mm^3($13 \times 10 \times 166.5$ mm^3) and of 14 (12) horizontal fingers of $10 \times 10 \times 163$ mm^3($13 \times 10 \times 218.5$ mm^3).

A single S3590-03 P-I-N photodiode (manufactured by Hamamatsu) is glued to one end of each finger. The photodiodes are fully depleted at 70 V and are coupled to the

[5]One expects an average of 0.35 neutrons per GeV of incident energy to be produced in electromagnetic showers due to photonuclear processes ('giant' resonances) [44]. This corresponds to a yield of 7×10^{13}(3×10^{13}) neutrons in the γcal (e^-cal) per year of HERA operation at the nominal luminosity.

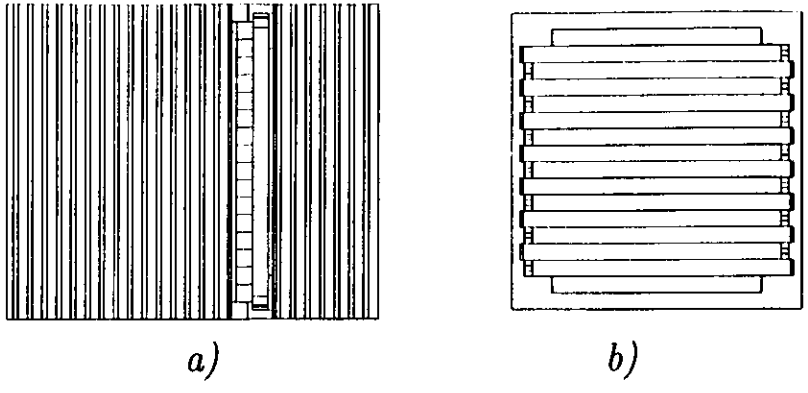

Figure 2.7: GEANT simulation of the γcal position detector; (a) a longitudinal cut through γcal showing the insertion of the position detector; (b) one plane of the detector with scintillator fingers.

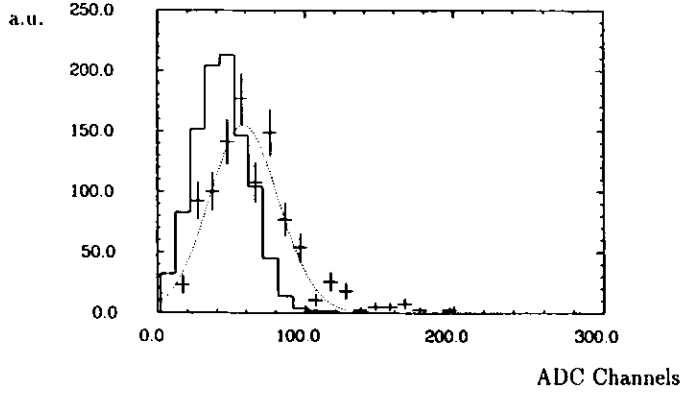

Figure 2.8: The calibration of a position detector channel based on the measurement of the average MIP signal; pedestal–solid line, MIP signal–dotted line.

low impedance input of the fast current amplifier MSD-2 [46] through a capacitor. The output of the front-end electronics is connected through 20 m of cable to the input of a four channel FADC card installed under the HERA floor. The FADC cards are similar to the cards used for the calorimeters, with the main difference being in the charge sensitivity which is about 0.4pC/channel for the position detectors. Test circuits include LEDs which are coupled to the fingers and are capable of generating 30 nsec wide (FWHM) light pulses, as well as charge injectors at the inputs of the preamplifiers.

The scintillator can withstand doses as high as 1 Mrad, and the photodiodes are placed far from the source of neutrons; the expected neutron fluence of $\approx 10^{11}$ $neutrons/cm^2/year$ is acceptable [47].

Performance of the Detectors and Beam Tests

The position detectors have been calibrated in a high energy electron beam. A convenient unit for the signal from a finger is the energy deposited by a MIP (Minimum Ionizing Particle). The MIP signal, of a 5 GeV electron traversing a finger, is comparable to the mean noise fluctuations (Fig. 2.8), therefore minimizing the noise is important and directly influences the resolution of the position measurement. The shower signal is much larger than the MIP signal and the spatial distribution includes 3–4 fingers. However, cuts to remove the noise are needed to measure the position accurately. A simple, though quite efficient algorithm requires the signal from a given finger be over the threshold of about 3–4 pedestal widths to be included in the position calculation. The position of the incident particle is calculated by taking the sum of the positions of the chosen fingers weighted with the energy deposited in the finger. In Fig. 2.9 two typical shower signals in two planes are shown with the threshold of the cut indicated.

A resolution of about 3.5 mm was obtained in the test measurements with an electron beam of 5 GeV, see Fig. 2.10. The resolution of the detectors improves with increasing energy due to the smaller fluctuations in the energy deposited in the fingers and the smaller influence of the noise. Monte Carlo simulations show that for energies over 10 GeV, the resolutions of photon and electron position detectors are about 2mm and 2.5mm, respectively.

2.2.3 The Čerenkov Counter

A Čerenkov counter placed between the carbon filter and the photon calorimeter is used to veto events in which a photon has converted between the exit window and γcal. An air filled Čerenkov counter was chosen because of its high threshold for electrons of 23 MeV, which is much higher than the energies of the synchrotron photons, and for its direction sensitivity.

Measurements in the electron test beam showed that the counter efficiency is $98 \pm 1\%$ inside a circle of 2 cm around the counter axis, and gradually decreases to 95% and to 90% at distances of 3 and 5 cm from the axis, respectively. No change in the efficiency was detected for small (a few degrees) tilts of the incident beam with respect to the counter axis.

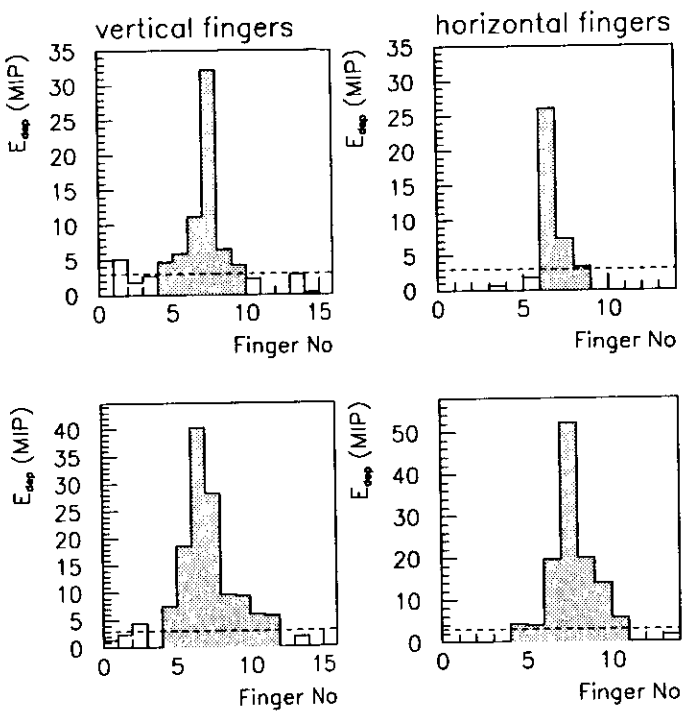

Figure 2.9: The shower profile in the photon position detector. The hatched area indicates fingers which were selected after applying the noise cut (dashed line) and clustering algorithm.

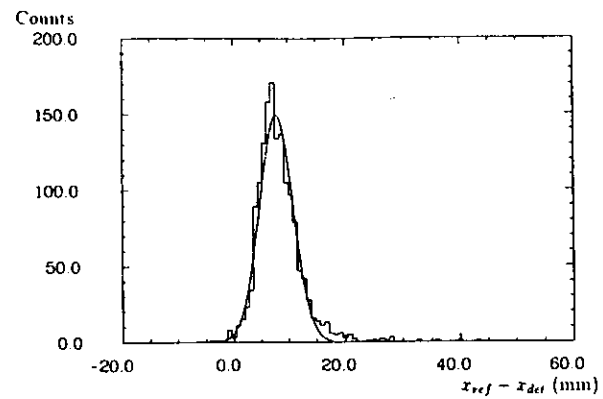

Figure 2.10: The test beam measurement of the resolution of the γcal position detector from the distribution of the difference between the position measured with a reference drift chamber (x_{ref}) and with the γcal detector (x_{det}).

2.2.4 Shielding

The environment of the HERA tunnel is heavily irradiated, mainly by synchrotron radiation and background related to the proton beam [48, 49]. Therefore, the components of the luminosity monitor have to be shielded.

The photon calorimeter must be shielded against the synchrotron radiation which is produced in the double function low-beta quadrupoles close to the IP. For the nominal electron beam energy of 30 GeV the direct synchrotron radiation leaving the proton beam pipe through the exit window carries about 500 W. Therefore, the carbon filter which is installed in front of the γcal , plays two roles: it reduces the signal from this direct radiation to a negligible level and protects the calorimeter from radiation damage. Additionally, the calorimeter has a 1 cm thick lead shielding on all sides and a 2.5 cm thick lead wall from the proton beam direction. The Čerenkov photomultiplier is placed in a 1 cm thick lead tube and is shielded from the electron direction by 2.5 cm lead. The electron beam pipe screen is situated between the exit window and the electron calorimeter and consists of lead plates of gradually increasing thickness from 2 to 10 mm. The screen shields the calorimeter from the energy of high energy bremsstrahlung electrons which hit the beam pipe wall.

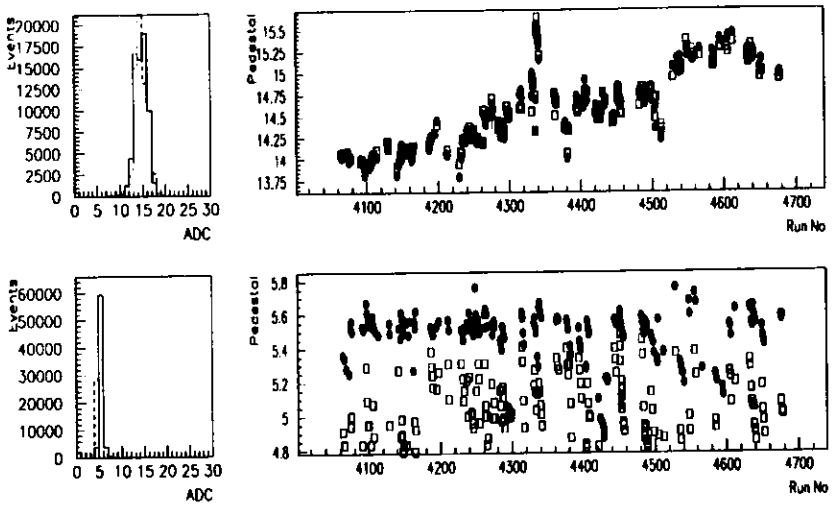

Figure 2.11: The pedestal distributions of two FADC channels and the average value of the pedestals as a function of the run number, for γcal (upper plots) and e^-cal (lower plots).

2.3 The Calibration of the Detectors

2.3.1 The Calibration of the Calorimeters

The miscalibration of the calorimeters can be a source of large systematic errors in the luminosity measurement (see Chapter 5), therefore the calibration should be maintained to within $\pm 2\%$. The calibration method of γcal and e^-cal makes use of the characteristics of the bremsstrahlung process in which both the end-point of the photon spectrum and the total energy, $E_\gamma + E_{e'}$, are equal to the energy of the electron beam, E_e.

The signal of each calorimeter is measured in two readout channels, adc_1, adc_2. The energy of the incident particle, E, is calculated from the measured ADC values by taking the geometrical average of the energies E_1, E_2:

$$E = \sqrt{E_1 E_2} = \sqrt{c_1(adc_1 - ped_1)c_2(adc_2 - ped_2)}, \tag{2.4}$$

where c_1, c_2 are the calibration constants which relate adc_1, adc_2 to the energies E_1, E_2 (in GeV) after subtraction of the pedestals ped_1, ped_2.

The calibration procedure is done in three steps: 1) measurement of ped_1, ped_2, 2) determination of the product c_1c_2, 3) determination of the ratio c_1/c_2. The pedestals are measured using a random trigger (i.e. the data from random bunch crossings) and are continuously monitored during the ZEUS runs. In Fig. 2.11 pedestal distributions and their long-term stability are shown.

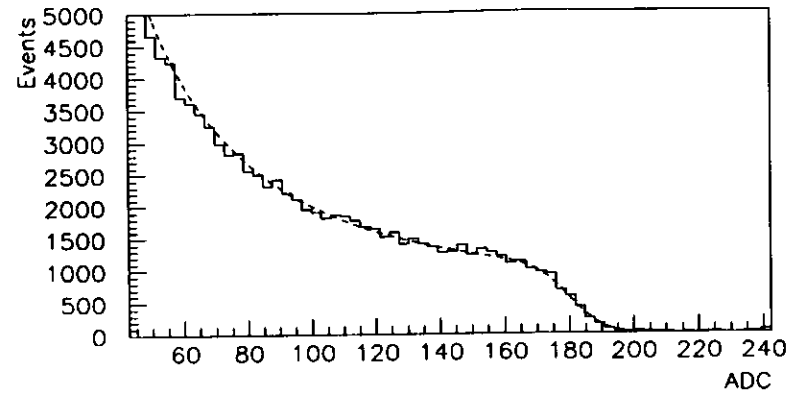

Figure 2.12: A measured bremsstrahlung photon spectrum (solid line) and the fit with the function F (dashed line).

The quantity $c^\gamma = \sqrt{c_1^\gamma c_2^\gamma}$, a calibration constant for the photon calorimeter, is measured from the end-point of the bremsstrahlung spectrum. As shown in Fig. 2.12, the shape of the measured bremsstrahlung photon spectrum ($E_\gamma > 10GeV$) is well described by the function $F(E_\gamma)$, which is the convolution of the Bethe-Heitler cross-section (see Eq. 1.17) and the Gaussian response function of the γcal :

$$F(E_\gamma) = N \int_{E_\gamma^{min}}^{E_{beam}} \frac{d\sigma}{dk_\gamma} exp(-(k_\gamma - E_\gamma)^2/2\sigma_0^2 k_\gamma) dk_\gamma, \tag{2.5}$$

where N is a normalization, k_γ is the photon energy and $\sigma_0\sqrt{k_\gamma}$ is equal to the calorimeter energy resolution. The three free parameters in the fit to the data are N, σ_0 and the factor converting E_γ to ADC counts. The latter can be identified with the γcal calibration constant c^γ. The consistency of this method has been tested with MC simulations (Fig. 2.13) which show that the calibration constant found by fitting F to the MC photon energy distribution gives the correct energy scale.

To find $c^e = \sqrt{c_1^e c_2^e}$, 'good' bremsstrahlung events have to be selected, i.e. events in which both the photon and the electron are well measured. Therefore, cuts on E_γ , $E_{e'}$ and E_{tot} are applied (Fig. 2.14a) to remove events with unreliable energy measurements, e.g. when a particle has hit the edge of the calorimeter (most often when $E_{e'} < 7GeV$ or $E_{e'} > 18GeV$). The measured distribution of E_{tot} as a function of E_γ , shown in Fig. 2.14, is fit with a straight line. The distance between the intercept of the line with the E_{tot} axis and the point corresponding to the beam energy measures directly the miscalibration of e^-cal . The method needs a few iterations as $E_{e'}$ was used in some data selections.

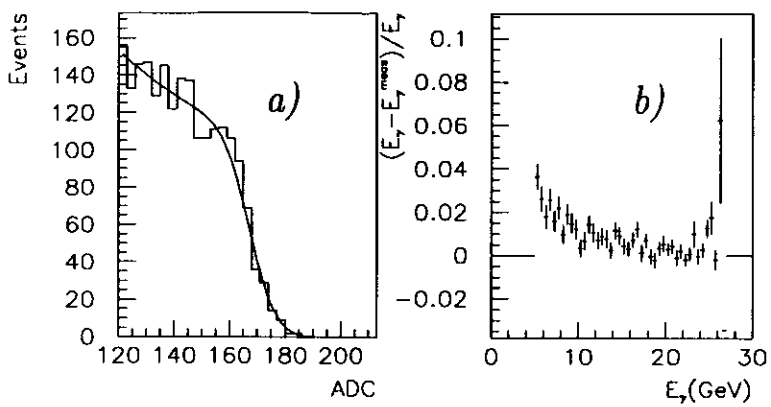

Figure 2.13: MC studies of the photon energy calibration. (a) MC bremsstrahlung photon spectrum and fit with the function F; (b) the distribution of $(E_\gamma^{meas} - E_\gamma)/E_\gamma$ showing that the calibration method provides the right energy scale (deviations at low energies are due to the absorption in the filter).

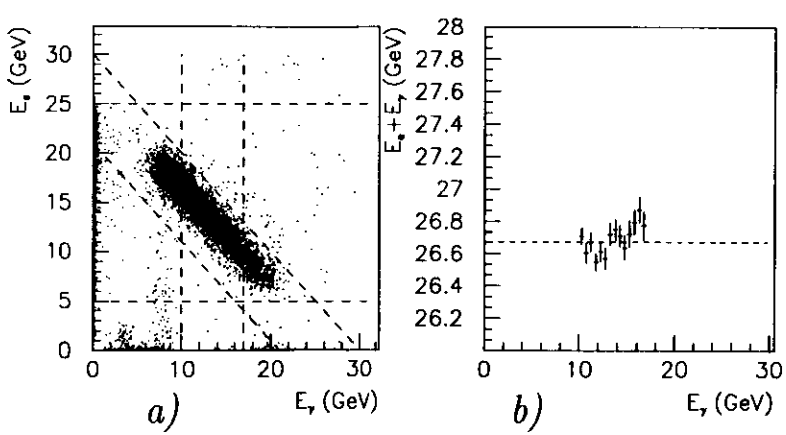

Figure 2.14: (a) Plot of $E_{e'}$ vs. E_γ with selection cuts indicated, (b) plot of the E_{tot} vs. E_γ and the straight line fit used to calibrate e^-cal .

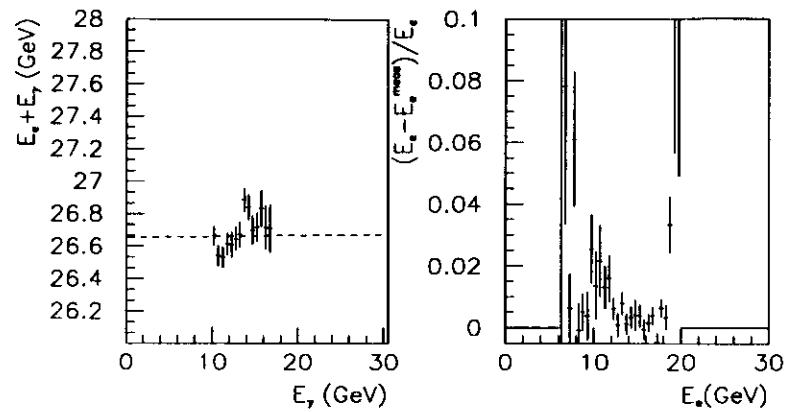

Figure 2.15: MC studies of the e^-cal calibration and a check of the energy scale.

The comparison shown in Fig. 2.15 of the MC results of the measured energy (after calibration of the MC data with the experimental procedure) with the 'true' energy generated in the simulation shows good agreement.

In Fig. 2.16 the long term behaviour of both constants is shown, which reveals two behaviors: slow, smooth changes which indicates a permanent deterioration of the gain of a channel and rapid fluctuations due to the limited accuracy and also presumably due to the effects of high event rates. The estimated precision of the calibration method is 2%.

Although the ratios c_1/c_2 are not used in the energy calculation they are needed to calculate c_1 and c_2 separately. The measurements of these ratios was done with the position detector in the photon calorimeter and the scintillator finger in front of the electron calorimeter. Events were selected in which particles had hit the center of the calorimeter. The ratio of the signals measured in the two channels equals the ratio of the calibration constants, c_1 and c_2.

An independent monitoring of the scintillator radiation damage is possible using the measurement of the light attenuation in the scintillator plates. The gains of the PMTs are monitored with the LED test system, which inject constant amounts of light onto the PMT photocathodes.

2.3.2 The Calibration of the Position Detector

A direct calibration of each channel of the position detector, as described in section 2.2.2, cannot be performed in the HERA tunnel. It is possible, however, to perform an indirect iterative method of calibration based on the observation that the average energy deposited in both detector planes should be equal and that both energies cannot depend on the hit

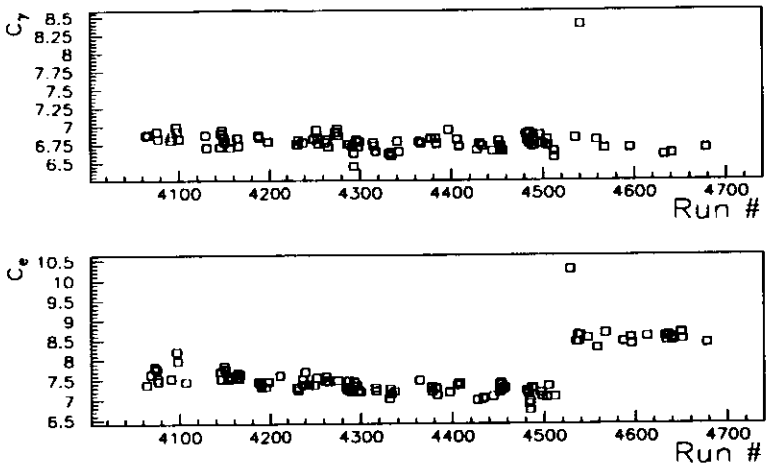

Figure 2.16: The long term behaviour of the calibration constants.

position. This method allows one to measure the ratios of the calibration constants which is all required for the position measurement. The absolute values have to be determined from the Monte Carlo simulations. The calibration of the position detectors are monitored with LEDs.

2.4 The Data Acquisition System

2.4.1 An Overview

The role of the Luminosity Monitor Data Aquisition (LMDAQ) system is to transfer the full LUMI monitor data for each HERA bunch crossing to the ZEUS trigger system. It should also perform 'hardwired' calculations and scaler counting which are used in on-line and off-line luminosity calculations. The system must be dead time free.

To meet the above requirements buffers are used to store and synchronize the events with the 10.4 MHz frequency of the bunch collisions (Fig. 2.17). The information stored in the buffers is accessed via a VME bus. Processes running on a VME based computer (MVME 147S) handle the data and transfer them to the ZEUS trigger system via a transputer board, which is also VME resident. The Luminosity Slow Control (LSC) controls the functioning of the electronics. The Luminosity Run Control (LRC) supervises the processes in the LMDAQ, performs the setups and resets of the system, watches over the data taking and communicates with the main ZEUS Run Control. Communication is maintained through an Ethernet link between the VME computer and a DEC workstation where a stand alone data analysis is performed.

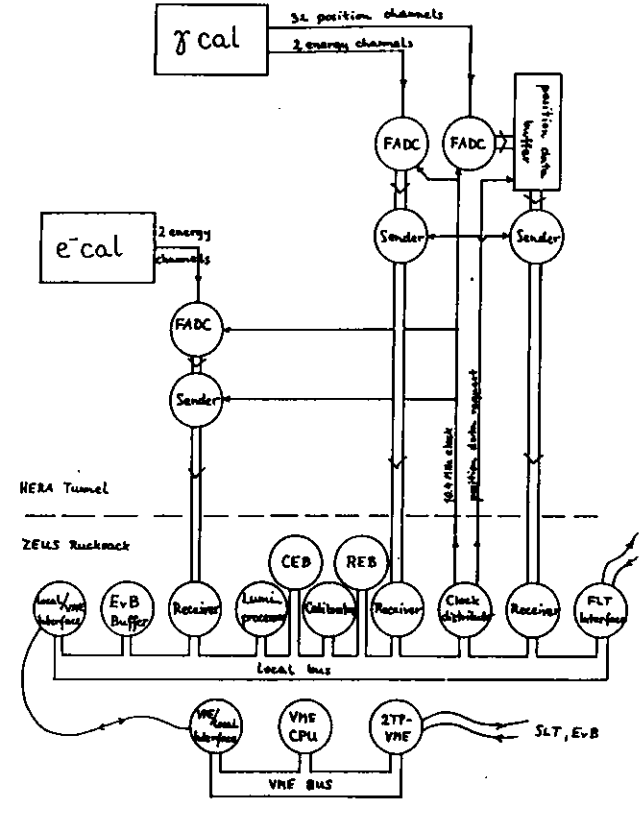

Figure 2.17: The general scheme of the LUMI monitor DAQ system.

2.4.2 The Structure of the DAQ

The luminosity monitor data aquisition system performs several independent functions. The major functions are: 1) the transmission of the data from the HERA tunnel to the ZEUS Rucksack, 2) the buffering and synchronization of the data, 3) the conversion of the raw FADC data to energy and the setting of a process flag, 4) the counting of the bremsstrahlung events, 5) the communication with the ZEUS trigger system. The important functions are discussed below in more detail.

The FADC data is transmitted from the tunnel to the ZEUS Rucksack at 10.4 MHz over a distance of 180 m and 100 m for the photon and electron branches, respectively. The basic transmission unit contains a sender board, 20 RG58 twisted pair cables and a receiver board.

The energy and position data are treated differently due to the limited number of transmission lines, as only 4×8 bits (4 FADC channels) can be sent in parallel from each branch. The energy data for each bunch crossing (2×8 bits) is sent synchronously with the HERA 10.4 MHz clock. The position detector data ($2 \times 32 \times 8$ bits of FADC data) is stored in cyclic buffers installed in the racks under the HERA tunnel floor. The buffer depth of 220 events is equal to the number of HERA bunches, therefore data from one complete HERA revolution can be stored. In this way data are kept for about 21 μs and are then overwritten. Thus, for any ZEUS trigger request coming (to the tunnel racks) at most 5 μs after the bunch crossing, the position detector event is available and can be attached to the energy data already sent to the ZEUS Rucksack.

The energy data is calibrated in the ZEUS Rucksack and transferred further to the FLT, and is stored in the Raw_Energy_Buffer and the Calibrated_Energy_Buffer (REB and CEB) during the wait for a decision from the FLT (see Fig. 2.17). When an accept decision (together with the bunch crossing number) arrives from the FLT, the proper energy data are copied from the REB and CEB to the Event_Builder_Buffer (EvBB) and a request for the position detector data is sent to the tunnel. After a few μs this data is also written into the EvBB where it waits for the SLT decision. Once a positive decision from the SLT is received, the full luminosity monitor event (4 FADC values from the calorimeters, a Čerenkov bit, process type flag, two 8 bit energies, 32+32 FADC values from the position detectors and the transmission status) is sent to the ZEUS Event Builder.

In parallel with the main stream of the data flow, tools for the stand-alone data collection are available. The energy data in the REB and CEB can be accessed via the VME bus. The position detector data can be transferred from the tunnel buffer to a separate part of memory in the EvBB on a request from the lumi_processor (see below).

The calibrator converts the FADC data from the REB into the energy, forms the mean of the two channels (E_1, E_2 in Sec. 2.3.1) and stores the result in the CEB (see Fig. 2.18). The conversion of the data is done with a 4×256 byte look-up-table, where the 8 bit FADC value is used as an address and the 8 bit number stored under this address is the calibrated value. The total energy $E_{tot} = E_\gamma + E_e$ is also calculated. These operations are done for each bunch crossing, synchronous with the 10.4 MHz HERA clock.

The energies E_γ, E_e and E_{tot} are transferred to the lumi_processor which determines the event type. The lumi_processor classifies each event as a bremsstrahlung, photopro-

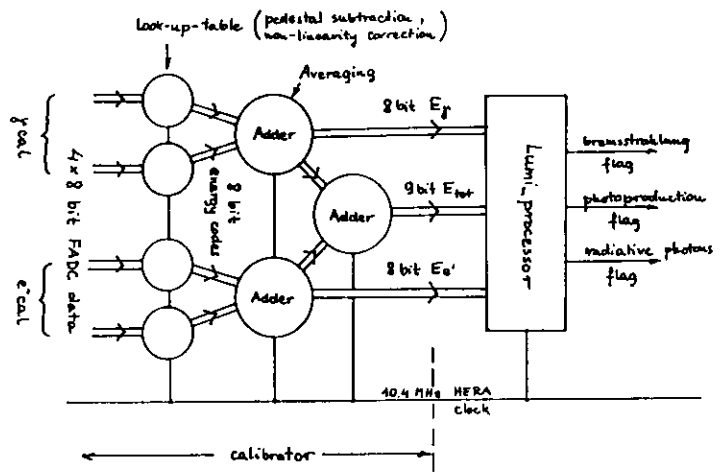

Figure 2.18: The lumi_processor and calibrators.

Process Type	Criteria	Bit#
bremsstrahlung	$E_\gamma > E_\gamma^{min}$	1
photoproduction	$E_e > E_e^{min}$ .and. $E_\gamma < E_\gamma^{min}$	2
radiative gamma	$E_\gamma > E_\gamma^{min}$ .and. $E_e < E_e^{min}$	3

Table 2.3: Types of physics processes flagged by the lumi_processor.

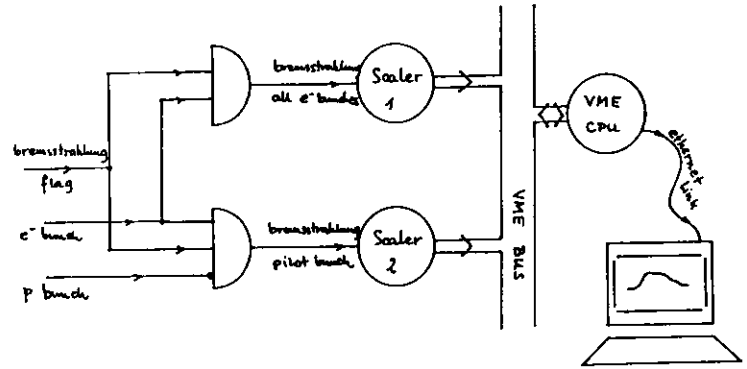

Figure 2.19: Counting bremsstrahlung events and the luminosity on-line display.

duction, radiative photon or a 'null' event and sets the proper bits to '1' in a 3 bit flag word. This flag is attached to the energy data. The criteria shown in Tab. 2.3 are 'hardwired' but the energy thresholds are programmable.

Five simple coincidence units which are read-out by scalers are installed for on-line luminosity monitoring. The input data for the units are (Fig. 2.19) the proton and electron bunch flags provided by the FLT (these 'hardwired' signals mark the non-empty proton and electron bunches), the lumi_processor bremsstrahlung flag and the HERA clock. The first scaler counts the bremsstrahlung events for crossings with non-empty electron bunches. The second counts the bremsstrahlung events for crossings with non-empty electron and empty proton bunches (i.e. crossings of an electron pilot bunch). The third and fourth scalers count the number of non-empty electron bunch crossings and pilot bunch crossings, respectively. The last scaler (serving interrupts) counts the HERA clock ticks and when the count reaches a predefined value an interrupt is generated which stops all scalers, resets and re-starts them. Just before the reset the scaler values are read. The electron-proton bremsstrahlung rate which is obtained from the scalers is used for the luminosity calculation and for the on-line display by the histogram presenter which runs on a DEC workstation (Fig. 2.19).

The ZEUS FLT system also provides a set of scalers which plays an imporatant role in the luminosity measurement: 64 scalers which count the bremsstrahlung events for 64 chosen BCN, and 32 scalers which count the 8 different types of bremsstrahlung events separately for colliding and piloting bunches as well as with and without correction for the ZEUS trigger dead time.

Chapter 3

The Measurement of Luminosity

3.1 The Experimental Procedure

3.1.1 Basic Formulae

The luminosity determination in the ZEUS experiment is based on the measurement of electron-proton bremsstrahlung. The bremsstrahlung event rate dN_{br}/dt is measured, the bremsstrahlung differential cross-section $d\sigma_{br}$ is calculated using QED, and the luminosity $\mathcal{L}$ is obtained with the following formula:

$$\mathcal{L} = \frac{dN_{br}/dt}{\int C_{exp} d\sigma_{br}}, \tag{3.1}$$

where C_{exp} is a correction factor for experimental effects. The integration is carried out over the angles of the initial and final state electrons, the energy and angles of the bremsstrahlung photons as well as over the positions of the electron-proton interactions. The cross-section can be corrected, if necessary, for the beam size effect (see section 1.4).

The main method of luminosity measurement considered in this thesis is based on the counting of bremsstrahlung photons. In this case the integral in the denominator of Eq. 3.1, denoted as σ_{br}^{obs} (after integration over the angles of the final state electrons), can be written as

$$\sigma_{br}^{obs} = \int C_{exp} d\sigma_{br} = \int a_\gamma \, f_{res} \, \rho_e \, \frac{d^2\sigma_{br}}{dE_\gamma \, d\Theta_\gamma} \, dE_\gamma \, d\Theta_\gamma^x \, d\Theta_\gamma^y \, d\theta_e^x \, d\theta_e^y \, d^3\vec{r}. \tag{3.2}$$

Here E_γ is the photon energy; Θ_γ is the angle[1] between the momenta of the initial electron and the bremsstrahlung photon, Θ_γ^x and Θ_γ^y are the projections of Θ_γ onto the (x,z) and (y,z) planes respectively); θ_e^x and θ_e^y are the angles of the initial electron; $a_\gamma(\theta_\gamma^x, \theta_\gamma^y, \vec{r})$ is equal to 1 when the bremsstrahlung photon leaves the beam pipe and 0 otherwise, and θ_γ^x and θ_γ^y are the angles of the bremsstrahlung photon and $\vec{r}$ is the position of the electron-proton interaction; $f_{res}(E_\gamma, \theta_\gamma^x, \theta_\gamma^y, \vec{r})$ describes the migration of events in energy due to absorber effects and the non-zero energy resolution of γcal, and $\rho_e(\theta_e^x, \theta_e^y, \vec{r})$ is a measure of the angular (θ_e) distribution of the beam electrons at the IP as well as of the spatial ($\vec{r}$) distribution of the ep interactions. For small angles $\theta_\gamma^x = \theta_e^x + \Theta_\gamma^x$ and $\theta_\gamma^y = \theta_e^y + \Theta_\gamma^y$.

[1] All angles are defined in the laboratory frame, see Fig. 3.1.

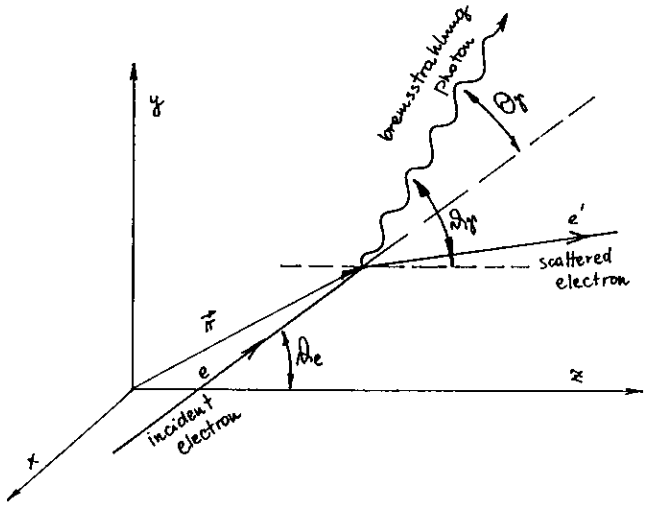

Figure 3.1: The definitions of the variables.

Since the fiducial area of γcal is large in comparsion with the transverse size of the beam of bremsstrahlung photons, Eq. 3.2 can be simplified with the approximation that f_{res} depends only on E_γ . The angular and energy dependence of the differential cross-section, $d^2\sigma_{br}/dE_\gamma d\Theta_\gamma$, can also be factorized. Performing the integration over angles in Eq. 3.2, one obtains:

$$\sigma_{br}^{obs} \approx A_\gamma \int f_{res} \frac{d\sigma_{br}}{dE_\gamma} dE_\gamma \,, \tag{3.3}$$

where

$$A_\gamma = (\frac{d\sigma_{br}}{dE_\gamma})^{-1} \int a_\gamma \rho \frac{d^2\sigma_{br}}{dE_\gamma\, d\Theta_\gamma} d\theta_e^x d\theta_e^y d\Theta_\gamma^x d\Theta_\gamma^y d^3r \tag{3.4}$$

is called the *bremsstrahlung photon geometrical acceptance.*

Since A_γ depends on ρ, A_γ and σ_{br}^{obs} can change in time if the e^- or p beam geometries change, e.g. if the position of the interaction region, the e^- beam divergence, or the direction (*tilt*) of the e^- beam axis changes.

There is a significant experimental difficulty in using the counting rate to determine the probability for bremsstrahlung production in intense beams (see section 3.4.2). One can see in Tab. 1.3 that for the nominal HERA luminosity of $1.5 \times 10^{31} cm^{-2} s^{-1}$ the average number of hard (e.g. $E_\gamma > 1\ GeV$) bremsstrahlung events per bunch crossing, μ, is about 0.3. The distribution of the number of events per bunch crossing, k, is given by the Poisson distribution $P(k,\mu) = e^{-\mu}\mu^k/k!$. For $\mu = 0.3$ a single bremsstrahlung event occurs in 22% of the bunch crossings, double events in 3%, triple events in 0.3%, etc. It is

not always possible to distinguish between single and multiple events. Values of the total energy $E_{tot} = E_e + E_\gamma$, which should be equal to the beam energy, and the shape of the shower profiles are the only criteria available on an event-by-event basis. However, these signatures are smeared by absorber effects, calorimeter and position detector resolutions, etc. A correction of the measured rate of bremsstrahlung events, dN_{br}^{meas}/dt, with a factor c_{mult} is required:

$$dN_{br}/dt = c_{mult}\, dN_{br}^{meas}/dt. \tag{3.5}$$

The correction can be calculated with MC; see section 3.3.4.

There is a method which does not require corrections for the pileup effect: instead of counting a bremsstrahlung rate one measures the energy flux into the photon calorimeter (e^-cal cannot be used in this case as the electron acceptance depends on $E_{e'}$). The luminosity can then be determined utilizing Eq. 3.1:

$$\mathcal{L} = \frac{dE_{br}/dt}{\int C_{exp} E_\gamma\, d\sigma_{br}}, \tag{3.6}$$

where dE_{br}/dt is the energy flux detected in the photon calorimeter.

In both methods the contribution of the *egas* interactions dN_{egas}/dt and dE_{egas}/dt must be subtracted from the total rate and the energy flux of bremsstrahlung events, dN_{tot}/dt and dE_{tot}/dt,

$$dN_{br}/dt = dN_{tot}/dt - dN_{egas}/dt$$

and

$$dE_{br}/dt = dE_{tot}/dt - dE_{egas}/dt.$$

For the luminosity measurement involving the measurement of the secondary electrons, the corresponding electron acceptance $A_{e'}$ is a strong function of the electron energy and f_{res} depends on the angles $\theta_{e'}^x, \theta_{e'}^y$. Therefore, the factorization, used in Eq. 3.3, is not as accurate and σ_{br}^{obs} can be estimated for a given experimental setup only on the basis of Monte Carlo simulations.

3.1.2 The Experimental Methods

The measurement of the luminosity with bremsstrahlung can be done in many different ways. One can measure the rate of $ep \rightarrow e'\gamma p'$ events, the energy flux in γcal , the single photon and electron rates or the coincidence rate. The methods are complementary because they are sensitive to a different extent, to the various instrumental quantities such as acceptances, calibration constants, etc. The comparison provides a cross-check of the procedures and an estimate of the systematic errors in the luminosity measurement.

The counting rate of the bremsstrahlung photons is sensitive to the calibration of γcal but less sensitive to the γcal energy resolution. In contrast, $\langle \frac{dE_\gamma}{dt} \rangle$ is insensitive to the pileup effect but requires an excellent understanding of the calorimeter resolution. The measurement of bremsstrahlung electrons is sensitive to the electron acceptance and to the calibration of e^-cal .

For the off-line physics analysis one usually uses the luminosity integrated over the time of data taking. The integrated luminosity is used in the conversion of the number

of selected events into a cross-section. When the beam conditions are stable and σ_{br}^{obs} is approximately constant in time, one can obtain the integrated luminosity with the substitution of dN_{br}/dt and dE_{br}/dt in Eqs. 3.1 or 3.5 with their integrals, i.e. the total number of events N_{br} and the total deposited energy E_{br}, respectively. This approximate method is sometimes useful for a crude on-line monitor of the luminosity, but for an accurate measurement one has to take into account the variation of the beam parameters in time as well as the dead time of the ZEUS trigger system. Then, the formula for the effective integrated luminosity, L_{eff}, delivered in the time interval Δt is

$$L_{eff} = \int_{\Delta t} f_{dead} \mathcal{L}\, dt, \tag{3.7}$$

where f_{dead} is a correction factor for the dead time of the trigger system, which is measured on-line.

3.2 The Measurement of the Acceptance

3.2.1 The Beam Position Measurements

The mean z position of the ep collisions directly influences the specific luminosity. In the ZEUS experiment this position is monitored with the C5 scintillator counters as well as with the Central Tracking Detector (CTD). The C5 detector measures the timing of the electron and proton beam related background with a resolution of about 0.5ns. Since it is placed 3.15m from the nominal IP, the signals associated with each beam are separated in time. The time difference between them equals half the distance between the C5 detector and the actual z position of the collisions, divided by the speed of light. The average z-position of the IP can be determined with an accuracy of 8cm using this method [50]. The spatial distribution of the vertices of the ep events reconstructed with the CTD data measures the average position and the spatial extent of the ep interaction region. For some dedicated runs the data from the HERA beam pick-ups was available, with which one can determine the beam trajectories.

3.2.2 The Photon Acceptance

The angular distribution of the ep bremsstrahlung photons is determined mainly by the divergence of the electron beam at the IP. This can be seen in Fig. 3.2 where the simulated angular distributions of the primary electrons and the bremsstrahlung photons are compared.

For nominal conditions, the majority of the bremsstrahlung photons leave the proton beam pipe through an exit window 82m from the IP (Fig. 3.3), traverse a distance of about 20m in air and hit γcal a total distance $l_{\gamma cal} = 106m$ from the IP. The hit position, (x_γ, y_γ), is measured with the γcal position detector and the photon angles $\theta_\gamma^x, \theta_\gamma^y$ can be evaluated using the relations

$$\theta_\gamma^x = x_\gamma / l_{\gamma cal},$$
$$\theta_\gamma^y = y_\gamma / l_{\gamma cal}. \tag{3.8}$$

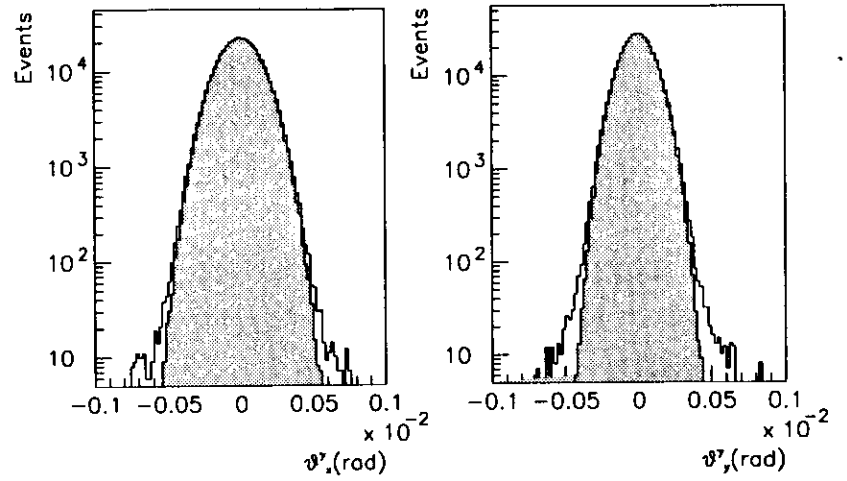

Figure 3.2: Simulated angular distributions of the beam electrons (dashed line) and the bremsstrahlung photons (solid line) at the IP.

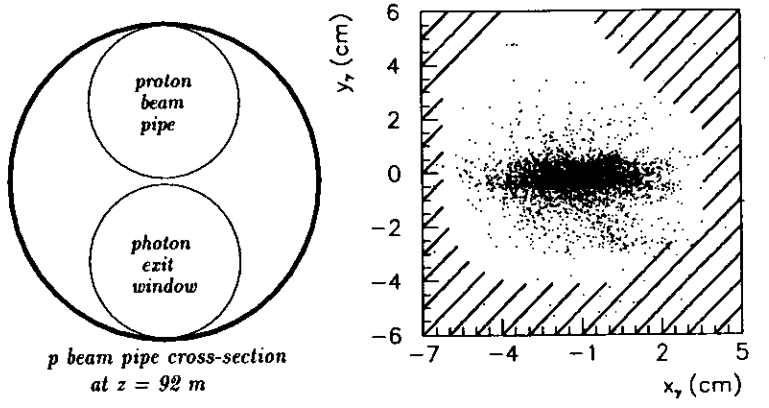

Figure 3.3: The photon exit window and the photon hit distribution at γcal (the hatched area marks the regions at γcal which are shadowed by beam-line magnets).

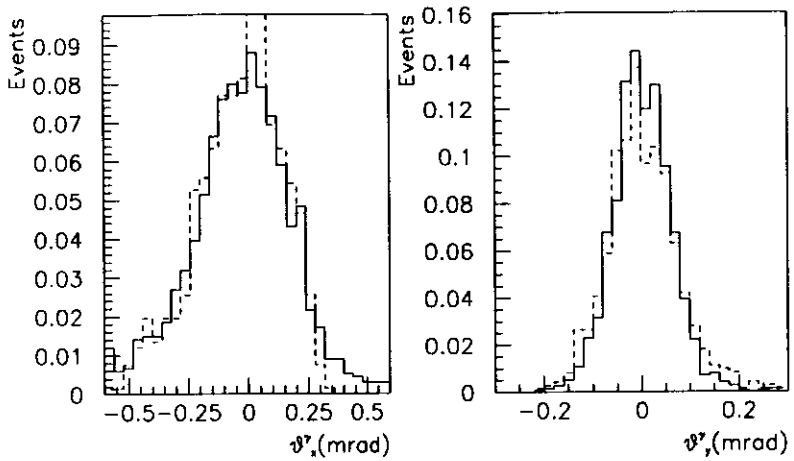

Figure 3.4: **The angular distributions of primary beam electrons (solid line) and measured (dashed line) bremsstrahlung photons, simulated using the MOZART program [51].**

A MC comparison of the electron angular distributions at the IP and the measured distributions, presented in Fig. 3.4, show that the measured values of $\langle\theta^x_\gamma\rangle$, $\langle\theta^y_\gamma\rangle$, $\sigma_{\theta^x_\gamma}$ and $\sigma_{\theta^y_\gamma}$ are very close to the actual values of the tilts and dispersions of the electron beam. Therefore the measured widths and positions of the photon beam at the γcal can be directly used to derive the electron beam parameters as well as to estimate the photon acceptance.

A number of test runs were performed to verify the photon acceptance used in the Monte Carlo simulations. Only the electron beam was circulated in HERA during these runs and therefore the acceptance for *egas* bremsstrahlung events could be measured. The MC results (Fig. 3.5) show that the photon acceptance for *egas* events is constant as a function of the z position of the eA interaction for events originating in the ZEUS straight section of the HERA ring, and drops abruptly to zero outside this region. Therefore, the change of the rate of *egas* events as a function of the beam tilt measures, to a good approximation, the change of A_γ [2]. Thus the relative photon acceptance can be measured as the ratio of the rate measured in a given run to the rate obtained from reference runs with a fixed electron beam geometry. In Fig. 3.6b the comparison between the experimental results and the MC expectations is shown. The observed systematic difference between the MC results and the data is accounted for the misaligment of the HERA magnets close to the IP[3].

[2]The distribution of the rest gas pressure is not exactly known, but is peaked at the IP.

[3]The measured misaligments of the HERA magnets were typically about 0.5mm, with values up to 1-1.5mm [52].

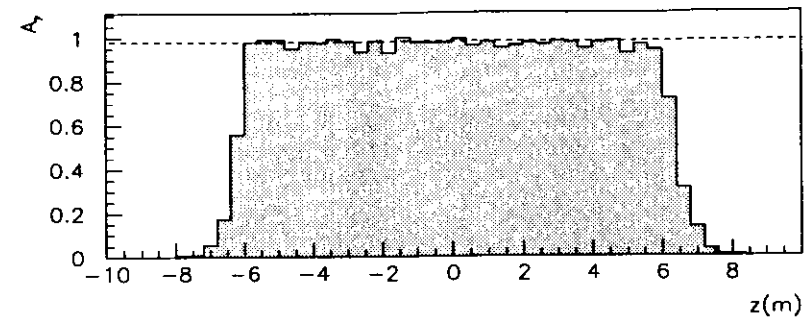

Figure 3.5: A_γ for *egas* events as a function of the z position of the interaction.

During normal operation the acceptance A_γ is monitored by tagging bremsstrahlung events with e^-cal . In this case, the measured acceptance A^{meas}_γ equals the number $N_{\gamma/e}$ of photons measured in coincidence with electrons divided by the number N_e of measured electrons. Selected electrons are required to have an energy at which the electron acceptance is close to 100%. This ensures that the angular distribution of the photons measured in coincidence is unbiased by the tagging with electrons. MC simulations show, see Fig. 3.7, that for a wide range of tilts this method gives consistent results.

The contribution of *egas* events spoils the results unless special corrections are made. The value of A^{meas}_γ measured for pilot bunches is much smaller than the expected acceptances for ep events, as shown in Fig. 3.8. This is caused mainly by *egas* bremsstrahlung events which occur outside the ZEUS straight section, for which the secondary electrons may be detected in e^-cal but for which the acceptance for bremsstrahlung photons is zero.

Since for colliding bunches the contribution of *egas* events is proportional to the electron bunch current, the *egas* contribution can be subtracted with the following formula:

$$A^{meas}_\gamma\,(ep) = \frac{N_{\gamma/e}(all) - kN_{\gamma/e}(pilot)}{N_e(all) - kN_e(pilot)}, \tag{3.9}$$

where $k = I^{tot}_e/I^{pilot}_e$ is the ratio of the total electron beam current and the current of the electron pilot bunches. A cutoff of the total energy, $E_{tot} > 21GeV$, is used in the selection of $\gamma \cdot e$ coincidences. The measured acceptances were constant for electrons in the energy range between 12 and 17 GeV (where the electron acceptance is high, see Fig. 3.8) as expected from MC studies. In Fig. 3.9 the dependance of A^{meas}_γ on the average position of the photon beam at γcal is compared with MC expectations.

No dependance on the BCN was found of the photon beam position and width measured in γcal . In particular, no significant difference for colliding and pilot bunches was observed; see Fig. 3.10. This justified the use of the same acceptance for all HERA bunch crossings.

The acceptance A_γ can be also estimated by fitting the photon beam profile measured in γcal with an *a priori* known distribution, because A_γ should equal the ratio of the

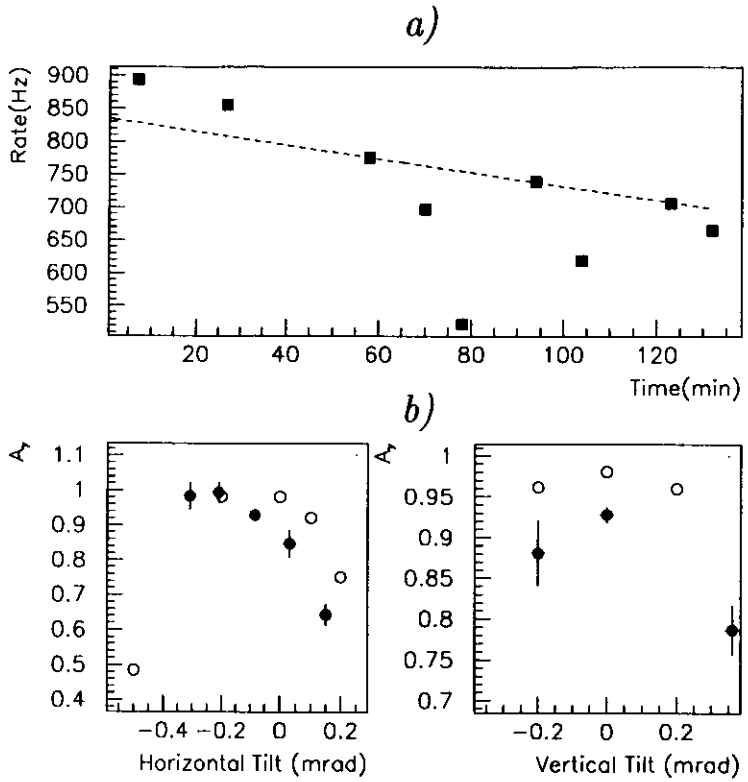

Figure 3.6: Measurements of A_γ for *egas* events; (a) the measured rate of bremsstrahlung events for several runs with different beam tilts, the dashed line indicates the estimated rate of the *egas* events for the reference setting of the electron beam; (b) the experimental results (full circles) are compared with MC predictions (open circles).

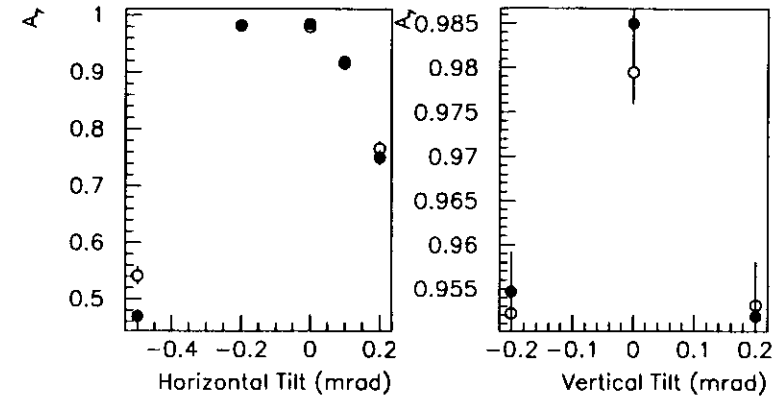

Figure 3.7: A_γ^{meas} (full circles) and A_γ (open circles) plotted as functions of the tilt of the electron beam, obtained from MC simulation.

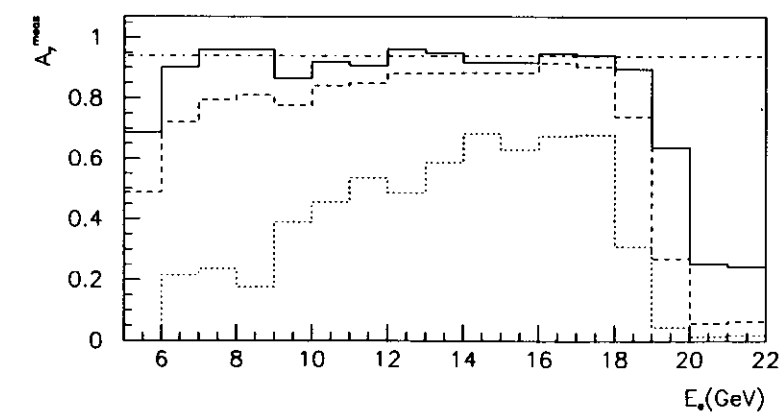

Figure 3.8: The acceptance, A_γ^{meas}, plotted as a function of the tagging electron energy for *egas* bremsstrahlung photons measured with pilot bunches (dotted line), for all bremsstrahlung photons from colliding bunches (dashed line), and for *ep* bremsstrahlung photons (solid line); the horizontal line is the result of fit to the *ep* acceptance in the range 12–17 GeV.

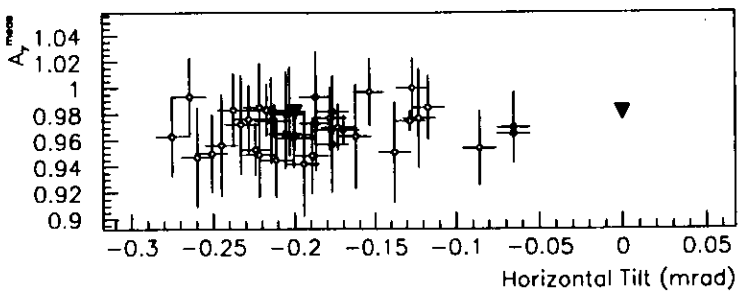

Figure 3.9: A_γ^{meas} plotted as a function of the horizontal position of the photon beam at γcal for runs with colliding beams. The triangles are the MC expectations.

number of measured events N_{meas}, and the total number of events obtained from the fit N_{fit} (from normalization factors). The advantage of this method is that the positions and tilts of the beam at the IP are not required. However, to obtain reliable results, the tails of the measured distributions should be very well understood to avoid the situation when some instrumental effects are not included in the fitting function. So far it has been difficult to apply this technique except for runs when the electron beam was strongly tilted and the shadowing of the magnet apertures was substantial. In that case, the acceptance was found by fitting Gaussian distributions to the photon hit distribution within a region where the acceptance is expected to be 100% (Fig. 3.11).

During the fall of '92 HERA running period the bremsstrahlung photon acceptance was approximately constant and for most runs was typically 98%, see Fig. 3.12.

3.2.3 The Measurement of the Electron Acceptance

Similar to the photon acceptance measurement, the electron acceptance $A_{e'}$ can be measured by tagging bremsstrahlung events with γcal. The acceptance $A_{e'}^{meas}$ equals the number $N_{e/\gamma}$ of photons detected in coincidence with matching electrons, divided by the number N_γ of all photons. An electron matches a photon when $E_\gamma + E_e > 21GeV$.

The series of HERA test runs discussed in the previous section was also used for the studies of the electron acceptance of the *egas* bremsstrahlung events. The results of the analysis show a clear dependence of $A_{e'}^{meas}$ on the tilt of the electron beam (see Fig. 3.13).

The analysis of the data taken during ZEUS luminosity runs, shown in Fig. 3.14, indicates that there is a small but systematic difference between $A_{e'}^{meas}$ for pilot and for colliding bunches. This is, however, expected from the Monte Carlo simulations and is a result of the different acceptances for *ep* and *egas* bremsstrahlung electrons.

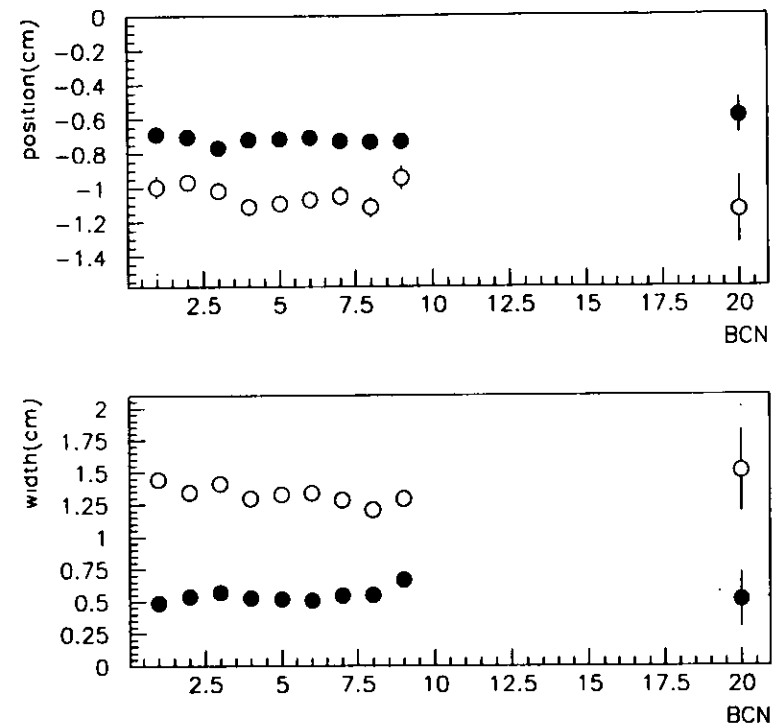

Figure 3.10: The width and position (horizontal – full, vertical – open circles) of the photon beam plotted as functions of the BCN.

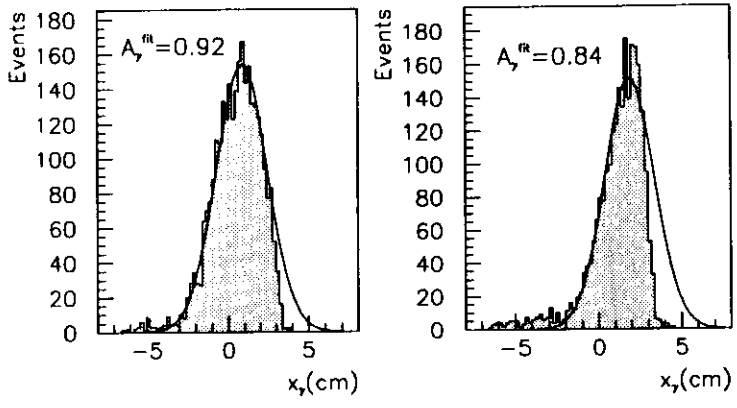

Figure 3.11: Measurement of A_γ by fitting the profile of the photon beam.

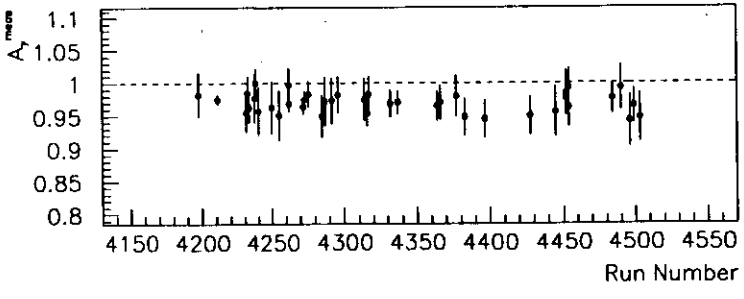

Figure 3.12: The history of the measured photon acceptance during the fall of '92 running period.

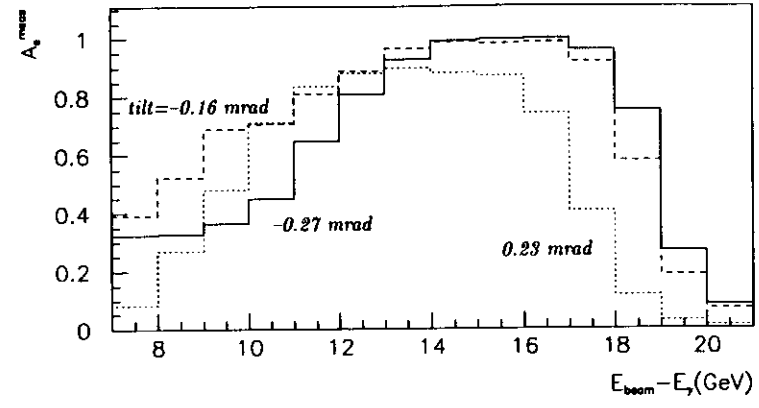

Figure 3.13: A_e^{meas} plotted as a function of the expected electron energy $E_{beam} - E_\gamma$ for three *egas* runs with different e^- beam horizontal tilts.

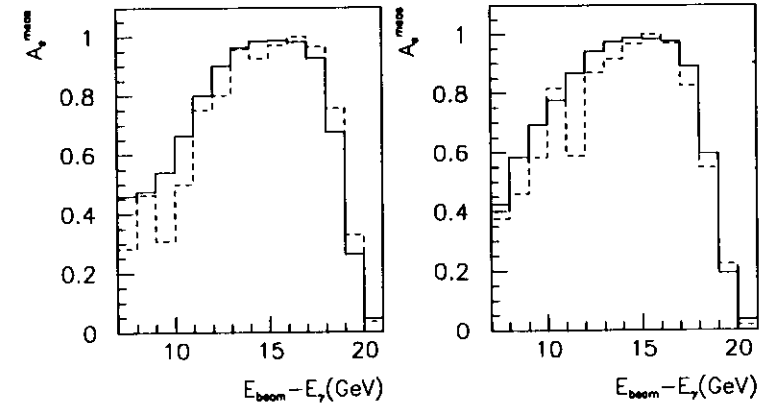

Figure 3.14: A_e^{meas} for colliding (solid line) and pilot bunches (dashed line) for two luminosity runs.

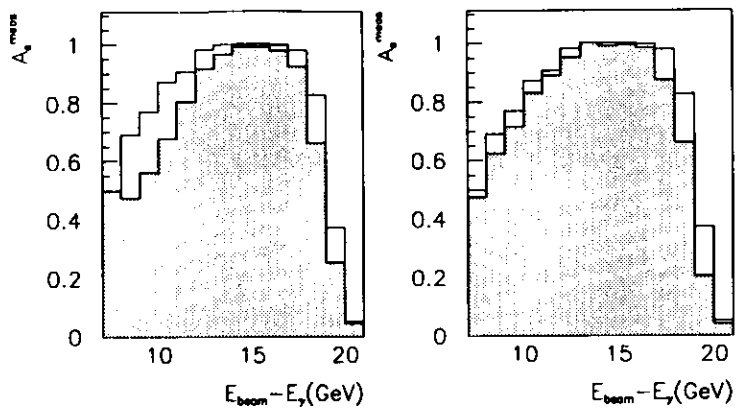

Figure 3.15: A comparison of $A_{e'}^{meas}$ for ep bremsstrahlung electrons, measured in two runs (hatched histogram) and the MC expectations.

$A_{e'}^{meas}$ can also be determined for ep events with the formula (as for A_γ^{meas}):

$$A_{e'}^{meas}(ep) = \frac{N_{e/\gamma}(all) - kN_{e/\gamma}(pilot)}{N_\gamma(all) - kN_\gamma(pilot)}, \tag{3.10}$$

where $k = I_e^{tot}/I_e^{pilot}$. A comparison of $A_{e'}^{meas}$ for ep events with the results of MC simulations is shown in Fig. 3.15.

3.3 Corrections

3.3.1 Calorimeter Resolution and Absorber Effects.

Due to the non-zero energy resolution of the calorimeters and the energy absorption by 'dead' material, events which in a perfect measurement would be classified as 'good' luminosity events can in practice fall out of this class; and, vice versa, 'bad' events can be measured as luminosity events. In Fig. 3.16 the distributions of the measured and 'true' energy of photons and electrons which reach γcal and e^-cal are compared.

The migration of events due to the imperfect energy measurement is larger in e^-cal than in γcal as bremsstrahlung electrons often hit e^-cal outside of its fiducial volume. For low energy photons the presence of the synchrotron radiation filter in front of γcal deteriorates the measurement of E_γ . The magnitude of the migration and the value of f_{res} in Eqs. 3.2, 3.3 are obtained from Monte Carlo simulations of the complete experimental setup.

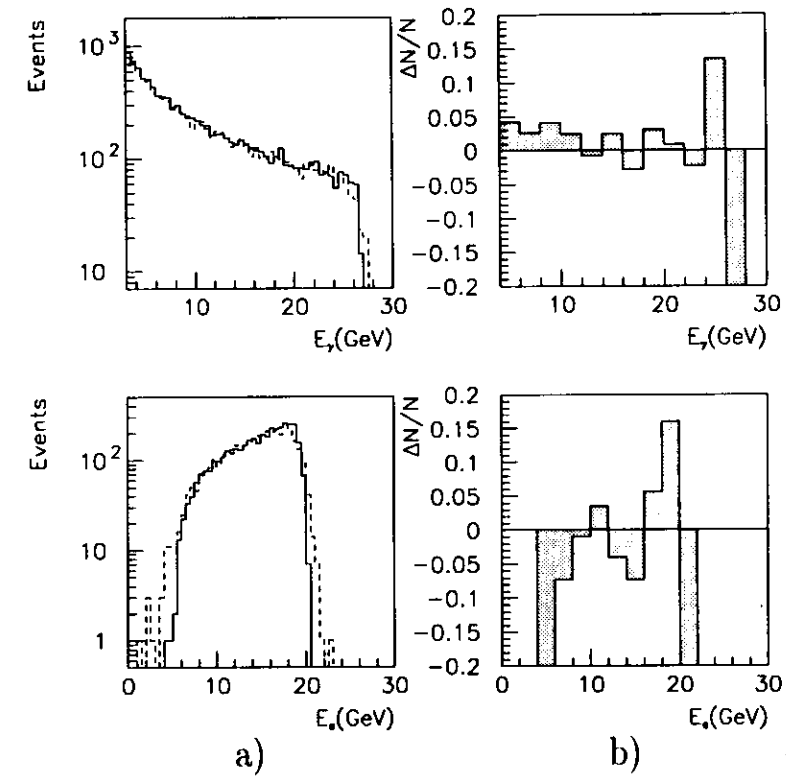

Figure 3.16: (a) MC distributions of generated (solid line) and measured (dashed line) energies of bremsstrahlung photons and electrons which reach the LUMI detectors; (b) plots of the relative difference between distributions in (a).

3.3.2 Subtraction of the Beam Gas Background

A major source of background is the process $eA \rightarrow e'\gamma A$, i.e. bremsstrahlung from the collisions of beam electrons with atoms of the residual gas.

Correction for this background can only be done statistically using data from measurements of the electron pilot bunches. For low event rates per bunch crossing, the rate of ep events, R_{ep}, can be obtained from the total rate R_{tot} and the rate measured with the pilot bunches, R_{pilot}, with the fomula:

$$R_{ep} = R_{tot} - R_{pilot}\frac{I_e^{tot}}{I_e^{pilot}}, \tag{3.11}$$

where I_e^{tot} and I_e^{pilot} are the currents of the electron beam and of the pilot bunches, respectively. For high rates this subtraction may not be so straightforward, as the event rates are not exactly proportional to the bunch currents; this effect will be discussed in the next section. At HERA, the electron bunch currents are measured with pick-up coils with an accuracy of 1-2%.

The pileup effect does not affect the measurement of the photon energy flux, $\langle\frac{dE_\gamma}{dt}\rangle$, and thus Eq. 3.11 can be used, regardless of the event rate, after having substituted the energy flux for the rates.

3.3.3 Multiple Event Correction

When the average number of bremsstrahlung events per bunch crossing is high, the probability of more than one such event occuring in a given bunch crossing (pileup) becomes comparable with the probability of the single event, see Tab. 1.3. There are three categories of such multiple events: (i) when each 'sub-event' separately is not triggered as a luminosity or 'good' event, but the combined signal is; (ii) there is only one good sub-event; (iii) there is more than one good sub-event in a given bunch crossing. Each category of events influences the total bremsstrahlung counting rate differentely. The first type will always increase the counting rate. The second kind will not change the counting rate but may decrease it, depending on the luminosity trigger which is used. Events from the last category will always cause an decrease of the counting rate. The contribution of each of these categories depends on the luminosity and the trigger type which is used, and it cannot be derived analytically.

The Monte Carlo simulation of multiple events was performed by generating a number of bremsstrahlung events N_{br} in a given bunch crossing from the Poisson distribution with mean $\mu = \sigma_{br}\mathcal{L}/f_c$ for equal bunches and $\mu_i = \sigma_{br}l_i/f_{rev}$ if the bunch were not equal; $\mathcal{L}$ is total luminosity, l_i is the luminosity for BCN i, f_c and f_{rev} are the HERA crossing and revolution frequencies, respectively. When $N_{br} > 1$, the signals from all sub-events are summed to form the signal.

The results obtained from the simulations show that the pileup at nominal luminosity significantly changes the measured distributions of E_γ and $E_{e'}$ (see Fig.3.17). The measured rates, R_{meas}, are not usually sensitive to the pileup effect and are close to the 'true' rates, R_{true} (see Fig. 3.18).

When the ratio R_{meas}/R_{true} differs from one, the algorithm for the subtraction of the $egas$ background described in the previous section should be modified and performed for

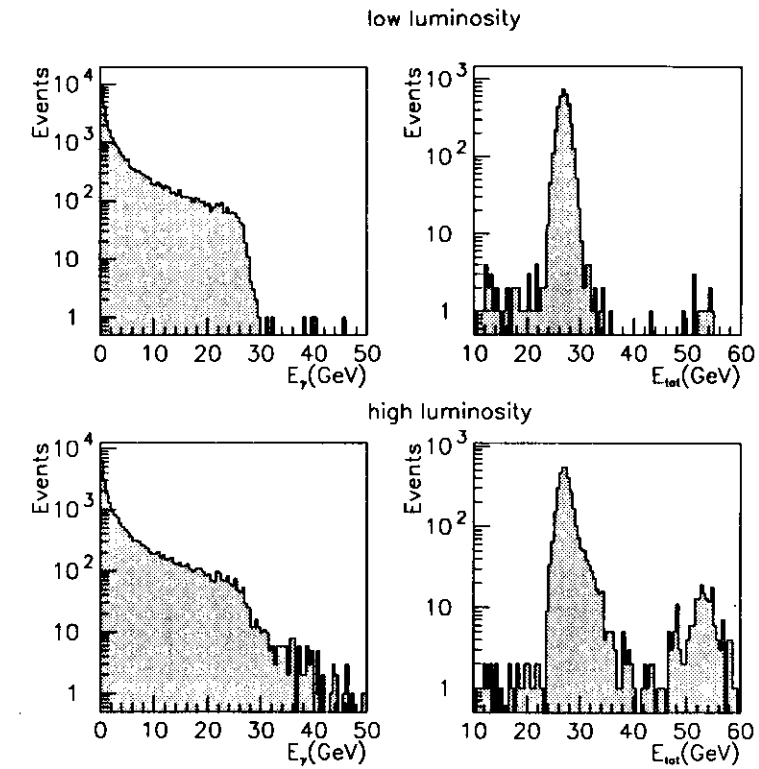

Figure 3.17: Monte Carlo distributions of the bremsstrahlung photon energy, E_γ, and total energy, E_{tot}, for low and high luminosities.

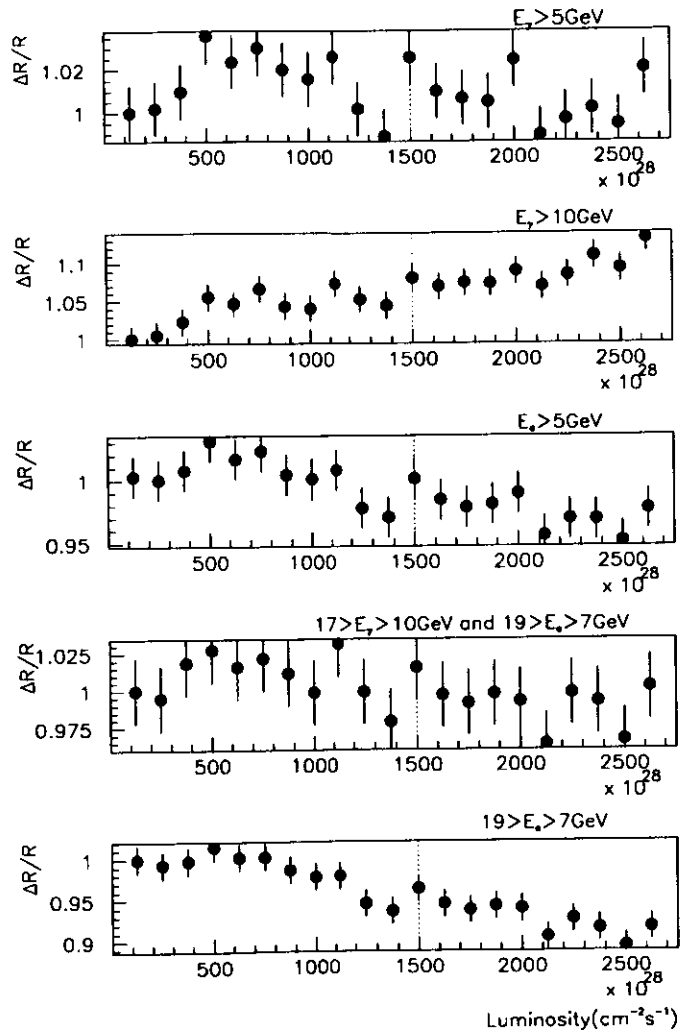

Figure 3.18: Monte Carlo study of $(R_{meas} - R_{true})/R_{true}$ as a function of the luminosity for different luminosity triggers (the dotted line indicates the nominal luminosity).

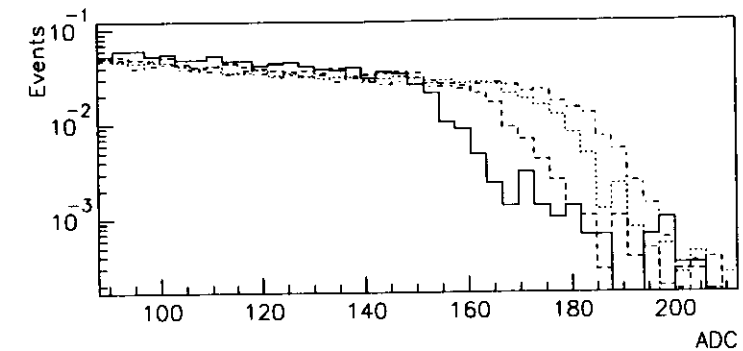

Figure 3.19: ADC distributions of the signals from γcal for several shifts of the timing.

each bunch crossing separately. First, the 'true' rate has to be unfolded using the results from MC simulations for each colliding and pilot bunches. Then, the *egas* subtraction is done for each BCN and the total luminosity $\mathcal{L}$ is obtained by summing the l_i over all colliding bunches:

$$\mathcal{L} = \sum_{i}^{bunches} l_i = \frac{1}{\sigma_{br}^{obs}} \sum_{i}^{bunches} R_{true}^{i} - k R_{true}^{pilot}. \tag{3.12}$$

Therefore, the c_{mult} factor in Eq. 3.3 equals the ratio R_{true}/R_{meas} (see Fig. 3.18).

3.3.4 Timing and Satellite Bunches

During normal operation, the luminosity monitor data acquisition system is timed with the 10.41 MHz clock provided by the HERA control system. Several test runs were taken with only the electron beam circulating in HERA to measure the sensitivity of the detectors of the luminosity monitor to a change in the timing. During the test runs the phase of the HERA clock was shifted by known amounts and the response of the detectors for each shift was measured.

In Fig. 3.19 the measured spectra of bremsstrahlung photons are shown for several shifts of the timing. The end-point of the photon spectrum and the distribution of the total energy, E_{tot} , (i.e. the c^{γ} and c^{e} calibration constants) were used to obtain the delay curves for the two calorimeters. The results are shown in Fig. 3.20.

The above investigations show that a drift of the timing (i.e. a change of the phase between the HERA clock and the actual time of bunch crossing at the ZEUS IP) of ± 2 *nsec* will cause a change in the measured energy of less than 2%.

The timing of the electron and proton bunches at the IP is monitored with the C5 scintillator counter described in section 2.3.1. For all runs taken in the 1992 fall period,

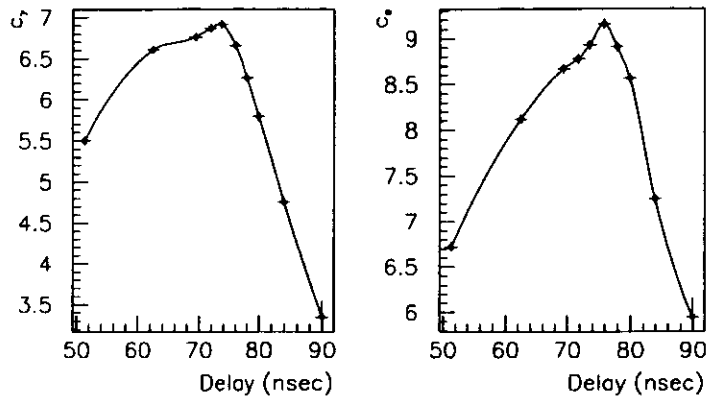

Figure 3.20: **The delay curves of the signals from γcal and $e^- cal$.**

the time distribution of the electron bunch signal revealed a peak 8 nsec apart from the signal of the nominal electron bunch (see Fig. 3.21). The height of the peak was typically 5–15% of the main peak. This unexpected peak was interpreted as the signal produced by small, so-called *electron satellite bunches*. Due to the incorrect timing (see section 1.3.2) the ep events from collisions of the e^- satellite bunches with the proton bunches were rejected by the ZEUS trigger system. In contrast, the bremsstrahlung events originating from the collisions of the satellite bunches with the proton beam were measured in the LUMI monitor with high efficiency.

The 8 nsec shift of the e^- bunch timing corresponds to a 4 nsec shift of the ep collisions with respect to the nominal timing. This causes a 1.2 m shift of the IP. It follows from the discussion in Section 1.1 that the specific luminosity changes with the position of the collisions along the z-axis according to

$$\mathcal{L}_{spec}(z) = \frac{f_{rev}}{2\pi\sigma_x(z)\sigma_y(z)}, \tag{3.13}$$

where

$$\sigma_x(z) = \sqrt{\epsilon_{x,e}(\beta^*_{x,e} + z^2/\beta^*_{x,e}) + \epsilon_{x,p}(\beta^*_{x,p} + z^2/\beta^*_{x,p})}$$
$$\sigma_y(z) = \sqrt{\epsilon_{y,e}(\beta^*_{y,e} + z^2/\beta^*_{y,e}) + \epsilon_{y,p}(\beta^*_{y,p} + z^2/\beta^*_{y,p})}. \tag{3.14}$$

Thus, at a distance of 1.2 m from the nominal IP the horizontal and vertical beta functions of the electron beam increase from 2.2 and 1.4 m to 2.85 and 2.43 m, and the proton beta functions increase from 7 and 0.7 m to 7.21 and 2.76 m, respectively, which results in a decrease of the specific luminosity to 52% of the nominal value. Therefore, collisions of satellite bunches with protons contributed to the ep bremsstrahlung rate at the level of 6% [50].

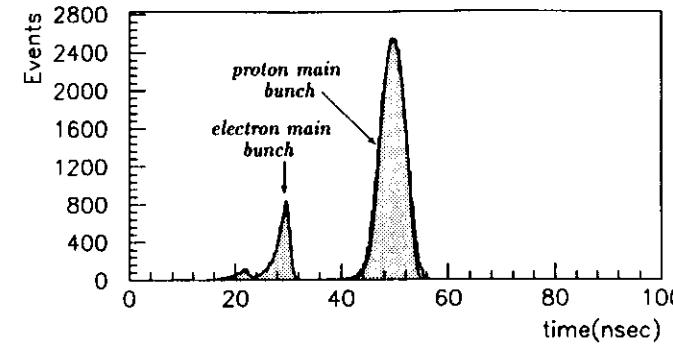

Figure 3.21: **C5 counter timing distributions, showing the electron and proton bunches.**

3.4 Measurement of the Energy Flux in the Photon Calorimeter

The luminosity measurement utilizing the measurement of the energy flux into γcal does not require a correction for multiple events. The mean energy deposited in γcal is found by dumping the content of the CEB buffer (described in section 2.3.2) which contains the energy data from one revolution of the HERA beams. Then, the energy is calculated for all relevant bunch crossings.

In Fig. 3.22 an energy distribution measured in γcal is compared with the results of MC simulations. The mean values of the distribution $\langle E_\gamma \rangle$ is equal to the average energy deposited in γcal per bunch crossing. To obtain the mean energy per second, $\langle \frac{dE_\gamma}{dt} \rangle$, one multiplies these averages by the HERA revolution frequency, f_{rev}, and by the number of bunches, N_{bunch}:

$$\langle \frac{dE_\gamma}{dt} \rangle = \langle E_\gamma \rangle \, f_{rev} N_{bunch}. \tag{3.15}$$

The *egas* background can be subtracted using the method described in Section 3.3.2.

At present, the mean energy deposited in γcal is low ($<$ 0.4 GeV), therefore the precision of the method is limited by the uncertainty of the pedestal value ($\pm$0.05GeV) and non-linearities of the FADC modules ($\pm$0.05 GeV). The energy deposited for the nominal luminosity will be higher ($\langle E_\gamma \rangle \approx$ 2GeV), but for a precise measurement the performance of the front-end electronics (pedestal stability, linearity, pileup) as well as an understanding of the energy scale (energy leakages, absorber effects) have to be substantially improved.

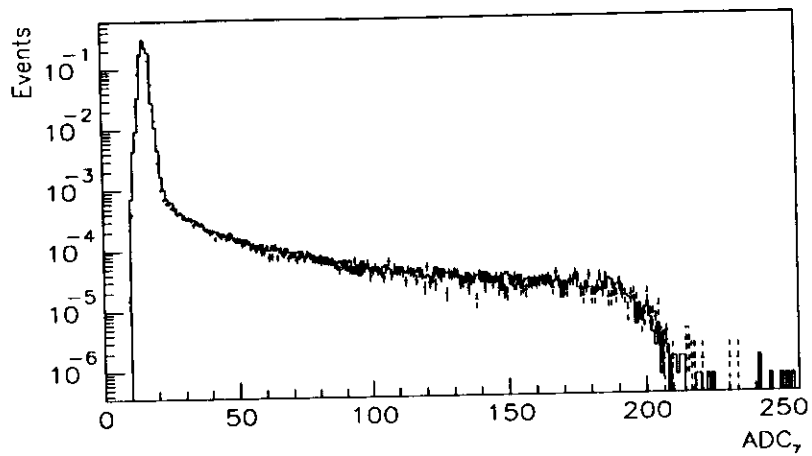

Figure 3.22: Measured (solid line) and simulated (dashed line) energy distributions in γcal .

3.5 Cross-Check Procedures and Experimental Results

3.5.1 Comparision of Different Luminosity Measurements

The comparisons between the luminosity obtained with different triggers or by measuring different quantities (rate vs. energy flux) are an excellent tool for understanding various experimental effects.

In Fig. 3.23 is plotted $L(E_\gamma > 5GeV)/L(E_\gamma > 10GeV)$, i.e. the ratio of the integrated luminosities measured by the counting rates of photons over 5 and 10 GeV respectively, which tests the measured photon energy scale. Fig. 3.24 shows a comparison between the luminosities measured only with γcal and when the electron measurement was involved, which is a test mainly of the accuracy of the electron acceptance measurement. We interpret the large systematic difference between the luminosities measured by the counting rates of photons and electrons (L_1 and L_3 in Fig. 3.24) as due to unsatisfactory description of the electron acceptance (especially for high electron energies) in the MC simulation and due to a large error in the *egas* subtraction in the calculation of L_3 (see Chapter 5).

The above results show the self-consistency of the luminosity measurements based on different triggers of bremsstrahlung events.

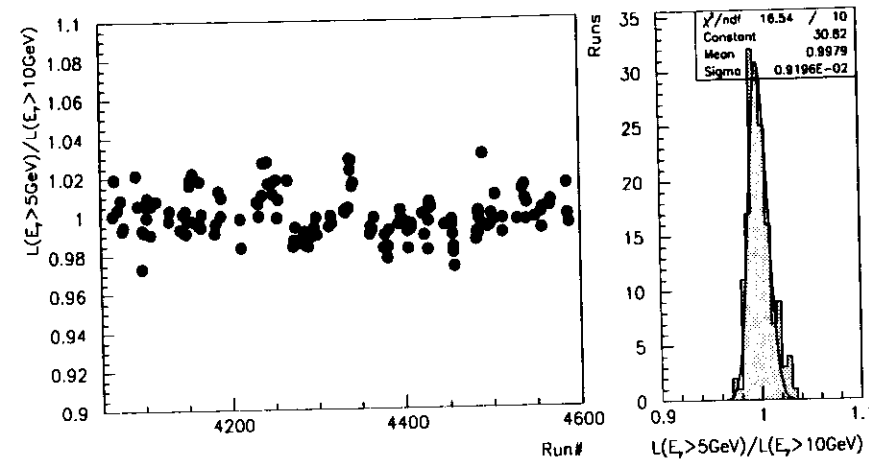

Figure 3.23: $L(E_\gamma > 5GeV)/L(E_\gamma > 10GeV)$ plotted as a function of the run number and its distribution for all runs – a test which is sensitive to the energy scale in the photon measurement.

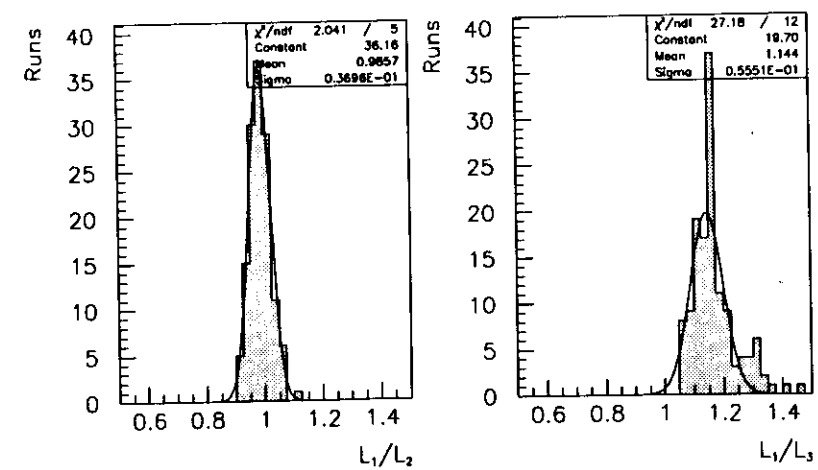

Figure 3.24: A comparison of the luminosities based on bremsstrahlung photon and electron measurements (L_1 : $L(E_\gamma > 5GeV)$, L_2 : $L(16 > E_\gamma > 10GeV$ and $19 > E_{e'} > 7GeV)$, L_3 : $L(E_{e'} > 4GeV)$).

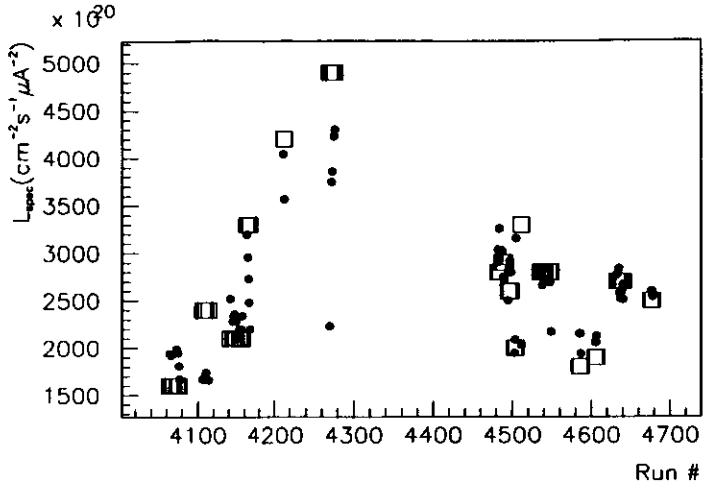

Figure 3.25: A comparison of the specific luminosities measured with the LUMI monitor (full circles) and those derived from the HERA beam parameters (squares).

3.5.2 The Specific Luminosity

The luminosity can also be estimated from the parameters of the colliding beams. This follows from the fact that the luminosity can be expressed as a function of the bunch currents, beam emittances and the values of the β-functions at the IP (see section 1.1). The bunch currents are measured with pick-up coils and the β-functions, which are determined by the focussing of the HERA magnet system, are known. The emittance of the proton beam is measured with an accuracy of about 10% [21] using beam profile residual gas monitors and a wire scanner. The emittance of the electron beam is estimated from Monte Carlo simulations and was confirmed by measurements of the electron beam divergence at the IP with the LUMI monitor.

In Fig. 3.25 the luminosities measured with the LUMI monitor and calculated from the HERA parameters are compared for runs when the proton beam emittance was available. The results from these two independent measurements of the luminosity are in good agreement.

3.5.3 The Method of Beam Separation

The magnitude of the ep bremsstahlung rate can also be measured utilizing a transverse shift of the proton beam at the IP. Such a shift ensures constant acceptances of the luminosity monitor branches and causes that the proton and electron bunches pass each other without colliding. The drop in the bremsstrahlung rate measures directly the contribution from ep collisions. After separation, the bunches can again be brought into collision. The

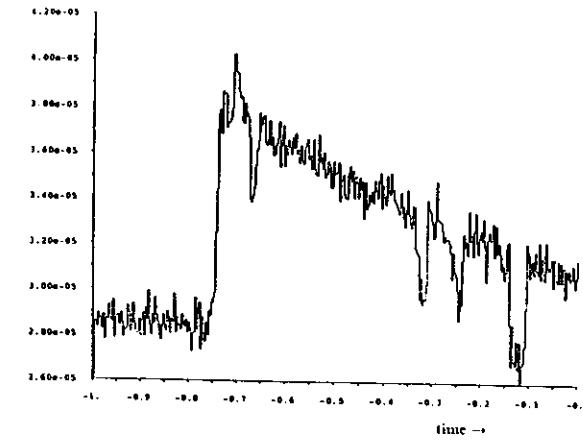

Figure 3.26: The bremsstrahlung rate plotted as a function of time during a HERA run in which several beam separations were performed.

results of several separations performed in a 1991 HERA run are shown in Fig. 3.26 [2].

The method requires a very precise handling of the proton beam and after the detectors of the ZEUS and H1 experiments were rolled into their working positions it was no longer used because of the high danger of proton beam loss and detector damage.

3.5.4 Summary of Experimental Results

In this section the results of the luminosity measurements performed during the HERA 1992 Fall (September–November) running period are summarized. For this period HERA operated with the low-beta optics described in section 1.2.2. There were typically 9 colliding electron and proton bunches, as well as one electron and one proton pilot bunch. Proton and electron beam energies were 820 GeV and 26.7 GeV, respectively.

During this time the ZEUS experiment took data corresponding to an integrated luminosity of $30.5nb^{-1}$ which is about 60% of the total luminosity delivered by HERA in the fall run.

A peak instantaneous luminosity of $1.7 \times 10^{29} cm^{-2}s^{-1}$ was observed on 9/10/92 (see Fig. 3.28), and the largest measured specific luminosity (see Fig. 3.29) was $4.4 \times 10^{24} cm^{-2}s^{-1}\mu A^{-2}$. The largest integrated luminosity collected within a single ZEUS run was $1.1nb^{-1}$ in a 3 hour run.

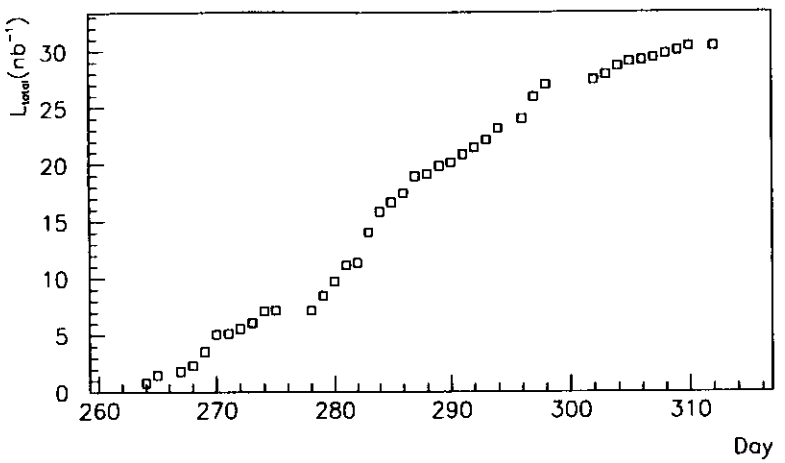

Figure 3.27: The ZEUS integrated luminosity as function of time.

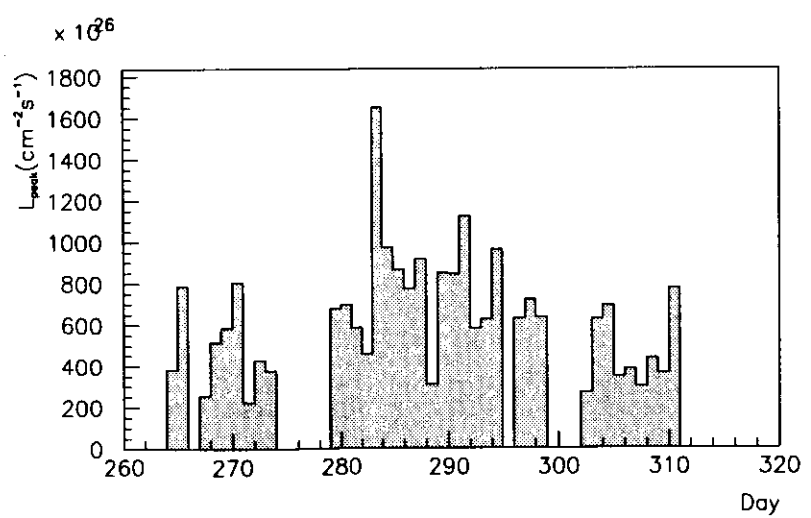

Figure 3.28: The history of the HERA peak luminosity.

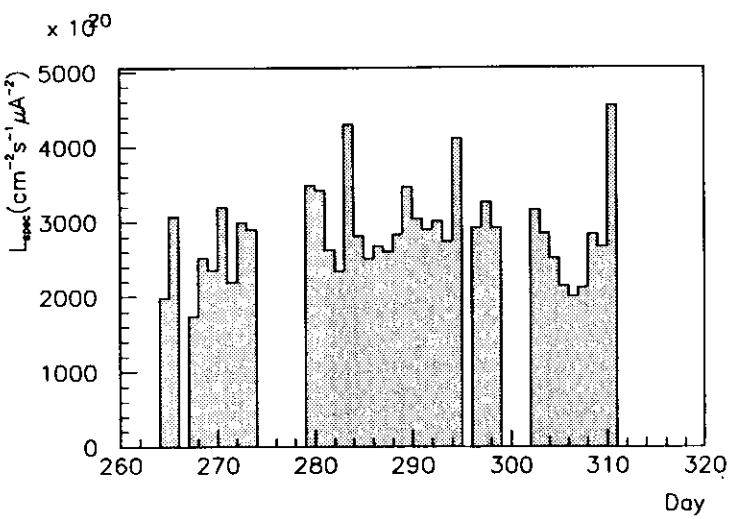

Figure 3.29: The history of the HERA specific luminosity.

Chapter 4

Background Processes

The measurement and identification of background processes is an essential part of any experiment. In the luminosity measurement described in this thesis, a good understanding of the background is vital for the analysis of the data as well as for forecasting the conditions of future measurements.

In this chapter the main sources of background are discussed. The most serious is the bremsstrahlung from collisions of the electron beam with atoms of the residual gas, which fakes the $ep \rightarrow e'\gamma p'$ process very well. Other processes, such as interactions of the proton beam halo, synchrotron radiation and Thermal Photon Compton (TPC) scattering off the beam electrons, concern mainly the measurement with γcal , except for the process $ep \rightarrow epe^+e^-$ which can be observed only in e^-cal .

4.1 *egas* Bremsstrahlung

As discussed in Section 1.4 the largest source of background in the luminosity measurement is the interaction of beam electrons with atoms of residual gas. The composition of the gas and its pressure in the vicinity of the IP are not precisely known. From tests and laboratory measurements a composition of 90% H_2 and 10% CO_2 is expected [53]. Therefore, a mean atomic number Z equal to 4.2 has been used in Monte Carlo simulations. The pressure of the residual gas is measured at the positions of the vacuum pumps (see Section 1.2.2) and the gauges are not closer than about 6m to the IP. As a result, some assumptions about the distribution of the gas pressure have to be made. A uniform distribution of the residual gas was assumed in the MC simulations.

The *egas* bremsstrahlung can be measured directly when only the electron beam is circulated or with the use of electron pilot bunches. The simulated and measured spectra of *egas* bremsstrahlung photons and electrons are compared in Fig. 4.1. It can be seen that the agreement between the data and MC predictions is good. The trigger required a coincidence of the signals in γcal and e^-cal . This limits the position of the electron-atom (eA) interaction to within about $\pm 6m$ from the IP because outside of this region the photon acceptance drops sharply to zero (see Fig. 3.5).

However, without the coincidence requirement there is a serious discrepancy between the measured and simulated electron spectra. The measured spectrum contains a peak at about 20 GeV (see Fig. 4.2), which is very poorly reproduced in the Monte Carlo simu-

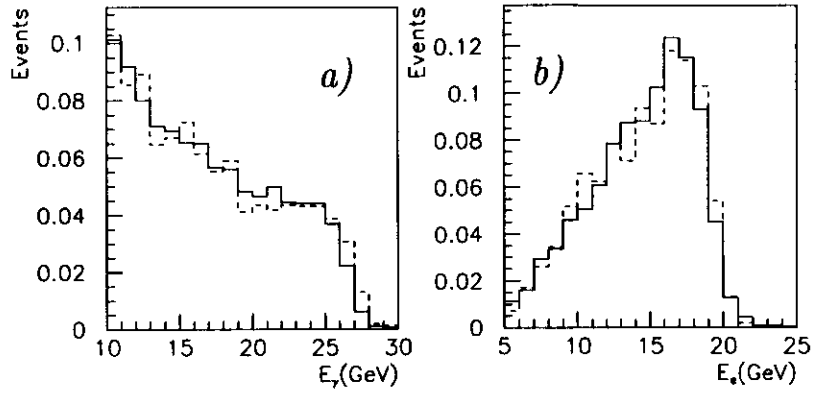

Figure 4.1: **Measured (solid line) and simulated (dashed line) spectra of *egas* bremsstrahlung (a) photons and (b) electrons.**

lations. The difference is particulary visible when no energy deposit is required in γcal . The discrepancy cannot be an artifact of the distribution of the rest gas pressure in the simulations because even with extreme distributions the effect could not be reconstructed. We expect that these events originate farther up-stream than is actually simulated in the MC.

Assuming a constant composition of the residual gas during the '92 running period and a mean atomic Z equal to 4.2, one can evaluate the mean gas pressure p along the straight section of the beam pipe by means of the measured rates of bremsstrahlung events for the pilot bunches R_{pilot}:

$$p = R_{pilot} k_B T e / \sigma^{obs}_{egas} I_{pilot} l, \tag{4.1}$$

where k_B is Boltzmanns constant, T is the temperature of the beam pipe, e is the electron charge, σ^{obs}_{egas} is the observed cross-section (in analogy to σ^{obs}_{br}) for *egas* bremsstrahlung events, $l = 12m$ is the length of the straight section and I_{pilot} is the current of the pilot bunches. In Fig. 4.3 the short and long term behaviour of the measured pressure is shown.

4.2 Synchrotron Radiation

Synchrotron radiation is produced by a charged particle which moves along a curved trajectory. The total radiated energy is proportional to the fourth power of the Lorentz factor of the particle, $\gamma = (1 - v^2/c^2)^{-1/2}$ (where v is the particle velocity), and is inversely proportional to the radius of curvature R of the trajectory [54]. The Lorentz factor of the

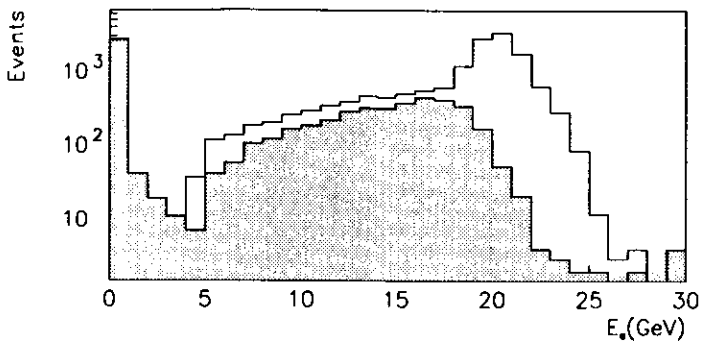

Figure 4.2: Measured distributions of the bremsstrahlung electron energy with (hatched histogram) and without the requirement of a coincidence with a photon.

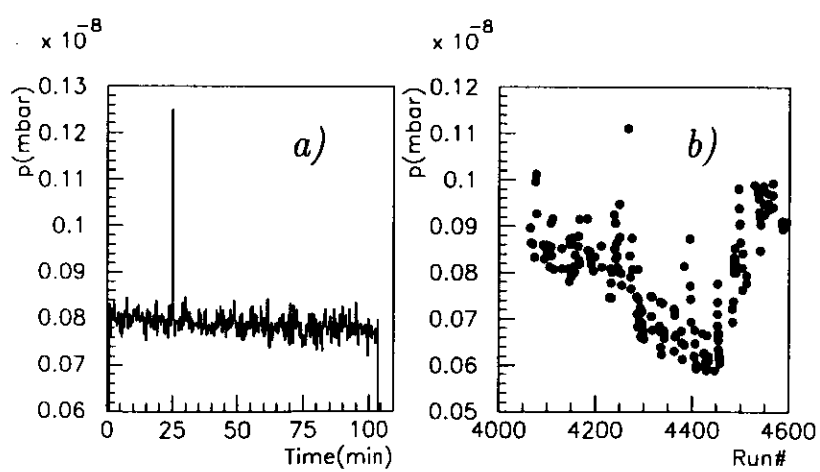

Figure 4.3: The measured rest gas pressure p as a function of time; (a) within one electron beam fill, (b) during the running period.

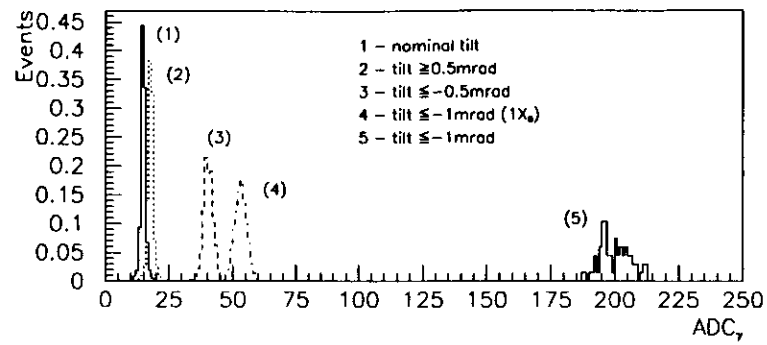

Figure 4.4: Shifts of the FADC pedestal due to synchrotron radiation (all runs with the $0.5X_0$ filter, except for the run #4).

electrons is about 70 times larger than that of the protons at HERA, and thus only the electron beam is a source of significant synchrotron radiation background. The energy spectrum of synchrotron photons is characterized by the *critical energy*, $k_c = 2\hbar c\gamma^3/3R$, and the radiation is confined to angles less than $1/\gamma$ with respect to the instantaneous direction of motion[1]. The number of synchrotron photons with energies between k_γ and $k_\gamma + dk_\gamma$ which are radiated in one revolution of an electron on a circular orbit is given by the formula [55]:

$$\frac{dN}{dk_\gamma}(k_\gamma) = \frac{\sqrt{3}\alpha\gamma}{2\pi k_c}\int_{k_\gamma/k_c}^{\infty} K_{5/3}(x)dx, \qquad (4.2)$$

where α is the fine-structure constant and $K_{5/3}$ is a modified Bessel function of the third kind.

While the electron beam is circulating, a fraction of the synchrotron radiation which is generated escapes from the beam pipe and, after multiple scattering, fills the accelerator tunnel. Therefore, all detectors of the LUMI monitor must be shielded against it. The detectors of the bremsstrahlung photons are additionally exposed to the direct radiation produced during the deflection of the electron beam immediately before and after the IP. The carbon filter installed in front of γcal drastically reduces the intensity of the radiation but at the same time degrades the precision of the energy measurement of the bremsstrahlung photons. So, a compromise is made to preserve a good energy resolution and yet keep the synchrotron radiation signal at an acceptable level.

The synchrotron radiation which reaches γcal is generated mainly in the dual function

[1]The similarity of the angular distributions of synchrotron radiation photons and bremsstrahlung photons is not accidental – ep bremsstrahlung can be viewed as the radiation from an electron bent in the electromagnetic field of a proton.

quadrupoles which are located about 6–7m from the IP. The radius R of the electron beam trajectory in these magnets is of the order of 1000m and the critical energy of the synchrotron photons for a 26.7GeV beam is about 30–40keV. The synchrotron radiation signal results in a shift of the ADC pedestals, ΔP_{sync} (Fig. 4.4). The dependance of the synchrotron radiation signal on the thickness of the carbon filter, the tilt of the electron beam, and on the BCN were investigated in a number of test runs. The synchrotron radiation signal normalized with the bunch current, ΔP_{sync}^{norm} (nominal bunch current is 0.27 mA, for the test runs the bunch current varied between 0.1 and 0.3 mA) , is plotted as a function of the filter thickness and of the beam tilt at the IP in Fig. 4.5. For large synchrotron radiation signals, e.g. above 20GeV, ΔP_{sync}^{norm} for subsequent bunch crossings increases, as can be seen in Fig. 4.5. We interpret this effect as a pileup, at the level of 1%, in the electronics. MC results, also presented in Fig. 4.5, describe well the absorption of synchrotron radiation as a function of the filter thickness. To match the data for large tilts of the electron beam the radius R was varied in the MC simulations between 1360 and 600 m. On the basis of these measurements thickness of the carbon filter was chosen to be 1 X_0 during the whole '92 running period.

The Monte Carlo simulations were done in two steps. First, the number of synchrotron photons reaching γcal per bunch crossing, dN^{cal}/dk_γ, was estimated by multipling dN/dk_γ from Eq. 4.2 by the number of electrons in the bunch, N_e, and by the product of the exponential attenuation factors of the absorber layers between the photon exit window and γcal :

$$\frac{dN^{cal}}{dk_\gamma}(k_\gamma) = N_e \frac{dN}{dk_\gamma}(k_\gamma) exp(-\sum_{abs.} d_i \mu_i(k_\gamma)), \tag{4.3}$$

where d_i is the thickness and μ_i is the attenuation coefficient of the ith absorber. The dependence of the μ_i on the photon energy were parameterized by fitting simple functions to the attenuation coefficients given in [56] (Fig. 4.6a).

Secondly, the sampling fraction $r(k_\gamma)$ of γcal was obtained using the EGS4 program [38]. The default version of the EGS4 package underestimates the mean energy deposited in the scintillator plates for incident photons with energies in the region 10–100 keV due to the termination of the transport of fluorescent photons. An extension of the EGS4 program was used to include the transport of fluorescence photons[2] and Rayleigh coherent scattering in the simulations (Fig. 4.6b). The distribution of the energy deposited in γcal , dE^{dep}/dk_γ, was then calculated from

$$\frac{dE^{dep}}{dk_\gamma} = k_\gamma \frac{dN^{cal}}{dk_\gamma} r. \tag{4.4}$$

The energy measured in γcal due to synchrotron radiation was obtained by integrating Eq. 4.4 over k_γ and dividing the result with the sampling fraction of γcal at high energies.

4.3 The Proton Beam Halo

The methods used to measure the proton beam related background in the LUMI monitor are described elsewhere [2]. The results obtained in the running period considered here

[2]The UCEDGE package [38].

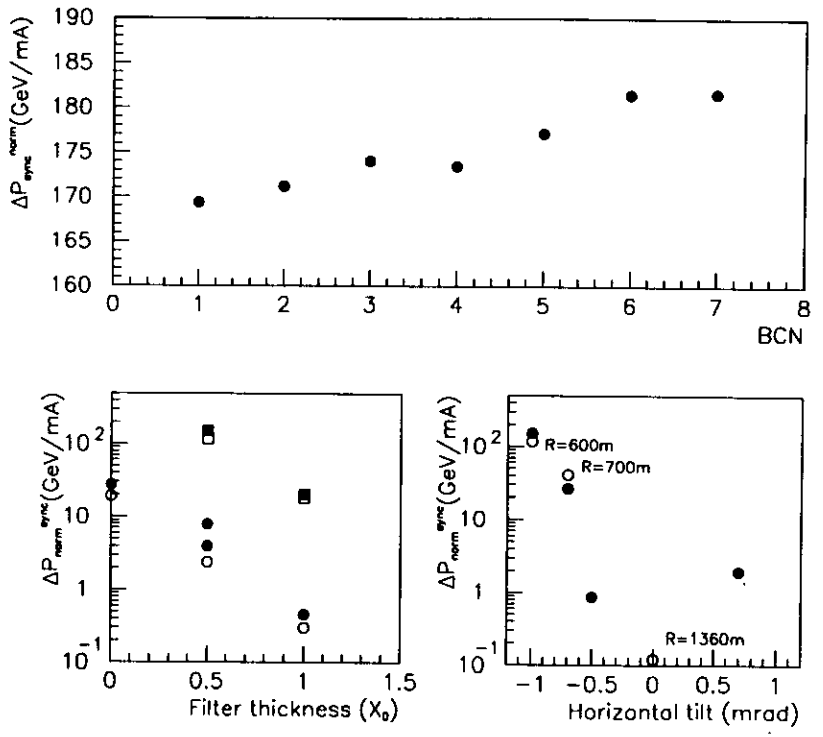

Figure 4.5: The synchrotron radiation signal plotted as a function of the BCN, the filter thickness, and the tilt of the e^- beam (data – full, MC – open symbols).

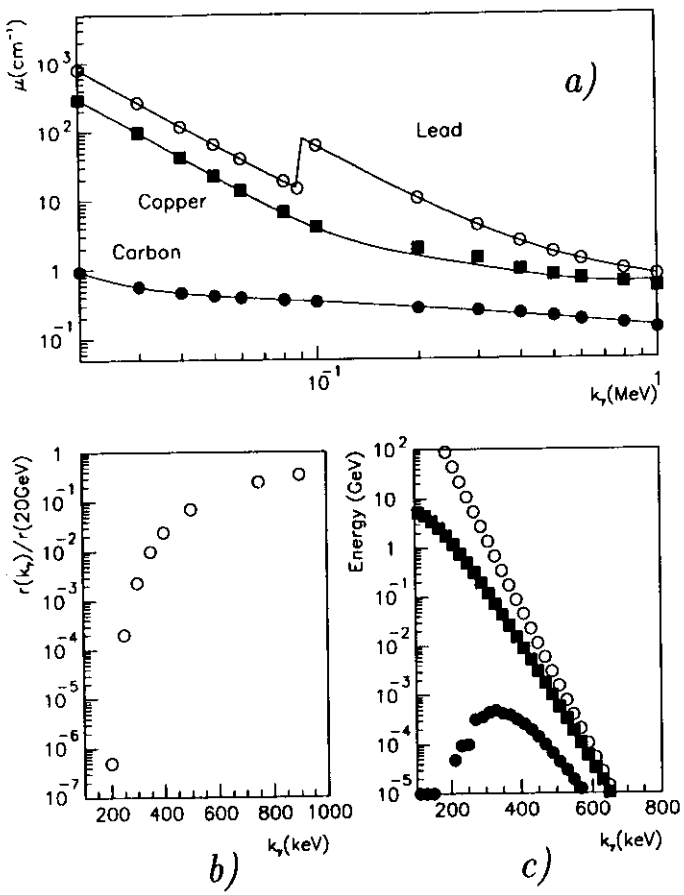

Figure 4.6: (a) Examples of the dependence of the absorption coefficients on the photon energy; (b) the γcal sampling fraction $r(k_\gamma)$ (normalized to the sampling fraction at high energies) obtained from EGS4 for small photon energies; (c) the energy per bunch crossing of the generated synchrotron photons (open circles), the photons reaching γcal (full squares) and measured in γcal (full circles) with the 1 X_0 carbon filter and the nominal electron bunch current.

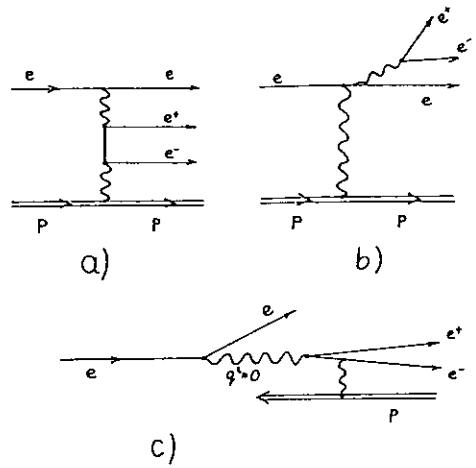

Figure 4.7: Feynman diagrams of $ep \to epe^+e^-$ in the first order perturbative expansion: (a) two-photon production, (b) bremsstrahlung production; (c) conversion of almost real photons into e^+e^- pairs.

show that this background was negligible in the luminosity measurement, and will not be discussed here further.

4.4 e^+e^- Pair Photoproduction

In the lowest order of perturbation theory, the process of e^+e^- pair production in electron-proton collisions is described by the two Feynman graphs shown in Fig. 4.7a,b. The contribution from two-photon production (Fig. 4.7a) dominates, and the bremsstrahlung production of e^+e^- pairs (Fig. 4.7b) can be neglected [57]. For the beam electrons which are scattered under small angles and are observed in the LUMI monitor, one can consider e^+e^- pair production as the conversion of a quasi-real photon ($Q^2 \approx 0$) in the proton field into an e^+e^- pair (see Fig. 4.7c).

In this way, the total cross section for $ep \to epe^+e^-$ observed in the LUMI monitor can be estimated from a convolution of the flux of virtual photons obtained from the EPA (Equivalent Photon Approximation) [58], and the cross-section for e^+e^- production in γp collisions:

$$\sigma \approx \frac{\alpha}{2\pi} \int \sigma_{\gamma p \to e^+e^- p}(y) \left(1 + (1-y)^2 \ln(\frac{Q^2_{max}}{Q^2_{min}(y)}) - 2(1-y)(1 - \frac{Q^2_{min}}{Q^2_{max}})\right) \frac{dy}{y}, \quad (4.5)$$

where $y = 1 - E_{e'}/E_e$, Q^2_{max} is limited by the electron acceptance and is of the order of $0.005 GeV^2$, $Q_{min} \approx m_e^2 y / E_{e'}$, and m_e is the electron mass. Integration of Eq. 4.5 over the

interval $5 < E_{e'} < 18\ GeV$ with $E_e = 26.7\ GeV$ yields $\sigma \approx 0.3\ mb$ [3]. The corresponding $ep \rightarrow e'\gamma p'$ cross-section is equal to 36.1 mb.

4.5 Other Processes

The volume of the beam pipe is filled with a gas of thermal (blackbody) photons with average energy, at room temperature, of about 0.025 eV. These photons, when back-scattered by beam electrons in Compton scattering, can acquire energies as high as 1GeV! This beautiful effect was recently measured at the LEP storage ring [60] and is also very clearly observed in measurements of the HERA e^- beam polarimeter [61]. In the luminosity measurement, however, the contribution from this process can hardly be observed due to the coarse resolution of the 8-bit FADC system and due to the substantial width of the ADC pedestals. For nominal beams, the expected mean energy deposit in γcal due to TPC scattering is below $0.1 GeV$, whereas the mean deposit due to bremsstrahlung events is 2 GeV.

The cross-section for the hadronic interactions, when the secondary electrons are detected in e^-cal , of virtual quasi-real photons with the beam protons [62] is only about a few μb [3] and can be neglected in the luminosity measurement.

4.6 Summary

On the basis of the studies presented in this chapter one can conclude that the background in the ZEUS luminosity measurement is small, except for the *egas* bremsstrahlung. This background is however well understood and monitored, and can be statistically subtracted from the measured distributions and rates. The production of e^+e^- pairs in ep collisions can be neglected in the luminosity measurement. The background due to synchrotron radiation and interactions of the proton beam halo were also monitored and found to be negligible even for extreme beam conditions.

[3] Recently, Monte Carlo studies showed that the exact cross-section for this process, with the LUMI monitor acceptance folded in, is 0.07mb [59].

Chapter 5

Experimental Errors

The procedure to evaluate the luminosity, discussed in chapter 3, requires the calculation of several independent instrumental corrections. These are the correction of σ_{br} due to the limited acceptance of bremsstrahlung events and the non-zero energy resolution, and the correction of the measured bremsstrahlung rates due to the contributions of background events, multiple events and the collisions of e^- satellite bunches with the protons. In this chapter the uncertainties in these corrections are estimated, and their contributions to the systematic error of the measured luminosity are discussed.

5.1 Uncertainty in the Acceptances

The error of the photon acceptance A_γ is estimated from the distribution of the relative difference between the measured acceptance and that predicted using MC simulations, according to $\Delta A_\gamma / A_\gamma = (A_\gamma^{meas} - A_\gamma^{MC})/A_\gamma^{MC}$.

In Fig. 5.1 the average difference $\Delta A_\gamma / A_\gamma$ is shown as a function of the horizontal tilts of the electron beam both for luminosity and *egas* (test) runs. The difference is most probably caused by the misalignment of beam-line magnets. Since the misaligment is not yet implemented in the MC simulations, therefore the difference has to be included in the error of the measured luminosity. In this way we find, for the typical tilts of -0.2 to -0.1 mrad in the fall '92 running period, a 2.5% error in the calculation of the photon acceptance of the LUMI monitor.

The error on $A_{e'}$ can be estimated in the same way. Distributions of $\Delta A_{e'} / A_{e'}$ shown in Fig. 5.2 indicate that the error on $A_{e'}^{meas}$ is about 4% and 7% for energy triggers requiring $16 > E_{e'} > 10 GeV$ and $19 > E_{e'} > 7 GeV$, respectively.

5.2 The Energy Calibration and Resolution

The 2% uncertainty in the calibration of the calorimeters (see Section 2.4.1) affects the various methods of measuring the luminosity in different ways. In Tab. 5.1 the relative luminosity errors $\Delta\mathcal{L} / \mathcal{L}$ caused by errors in the energy calibration and by the uncertainty of the pedestal values are listed. The numbers were obtained with the help of Monte Carlo

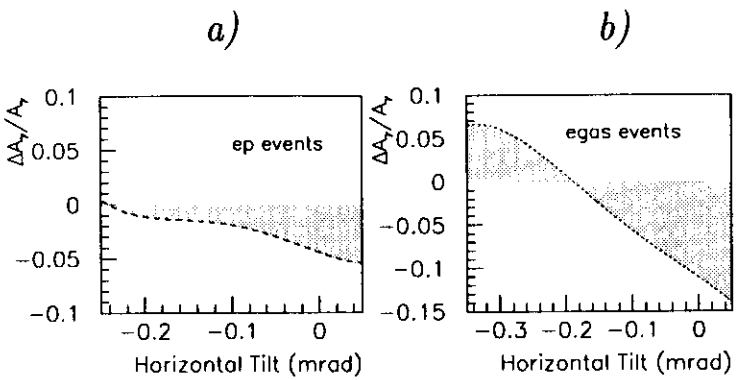

Figure 5.1: $\Delta A_\gamma / A_\gamma$ plotted as a function of the horizontal tilt of the electron beam for (a) ep and (b) $egas$ events.

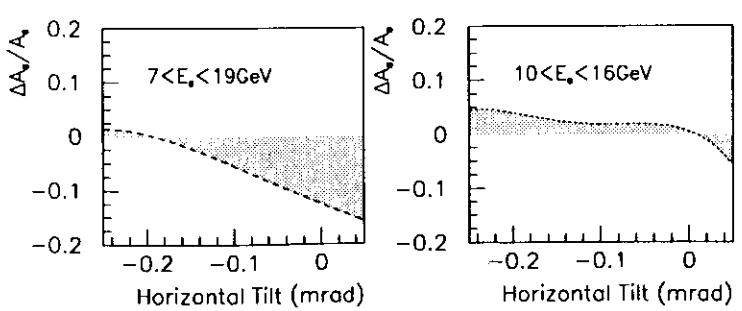

Figure 5.2: $\Delta A_{e'} / A_{e'}$ in two electron energy intervals plotted as a function of the horizontal tilt of the electron beam.

Trigger requirement	Error due to 2% mis-calibration	Error due to 0.05GeV pedestal uncertainty
$E_\gamma > 5GeV$	2.0%	0.7%
$E_\gamma > 10GeV$	2.5%	0.7%
$E_{e'} > 4GeV$	< 0.2%	-
$7 < E_{e'} < 19GeV$	2.5%	1.2%
$7 < E_{e'} < 19GeV \& 16 > E_\gamma > 10GeV$	1%	< 0.3%

Table 5.1: $\Delta\mathcal{L} / \mathcal{L}$ due the mis-calibration of the calorimeters and the uncertainty of the FADC pedestal values.

simulations by intentional mis-calibration of the calorimeters or change of the pedestal values and the calculation of the changes in the measured rates.

A comparision of the luminosities measured with two different photon energy thresholds (see Section 3.5) can be used to estimate the error due to errors in the energy scale of the bremsstrahlung photon. This is possible because the ratio of the luminosities, $r = L(E_\gamma > 5GeV)/L(E_\gamma > 10GeV)$, is sensitive to the calibration error of γcal. A 1% deviation of the ratio from 1 indicates a 3% error in the energy scale of the photon measurement. The measured mean value of the ratio (see Fig. 3.23) of 0.998 and the width of its distribution of 0.009 correspond to an uncertainty in the energy scale of the order of 2%, which is consistent with the estimates of the error of the γcal calibration.

The migration of events caused by the non-zero energy resolution and fluctuations of the energy deposited in the absorbers also contributes to the error of measured luminosity. Such a migration influences the value of σ_{br}^{obs} in Eq. 3.1 and the factor f_{res} in Eq. 3.2 corrects for its effect on the luminosity. Large energy deposits in the carbon filter result in a low energy tail in the distribution of E_{tot}, and the width of the distribution measures the energy resolution of both calorimeters. As can be seen in Fig. 5.3, the MC simulation describes both effects well.

Assuming a conservative value of 20% for the accuracy of the MC simulation of the migration effect, one finds that the error due to this effect is small, equal to $0.05 \times 20\% = 1\%$, where 0.05 is the magnitude of the migration in the MC and corresponds to a typical value of $1 - f_{res}$.

5.3 Subtraction of the *egas* Background

Inaccuracies in the subtraction of the background associated with the e^- beam are caused by errors in the bunch current measurements, the dependence of the acceptance on the BCN, by instrumental effects such as signal pileup in the electronics, and changes of the PMT gains with large currents.

The accuracy of the subtraction was monitored in two ways. First, with only the electron beam circulating in HERA, the measured rate of ep events should be consistent with zero. This corresponds to a constant rate of $egas$ events after normalization with the

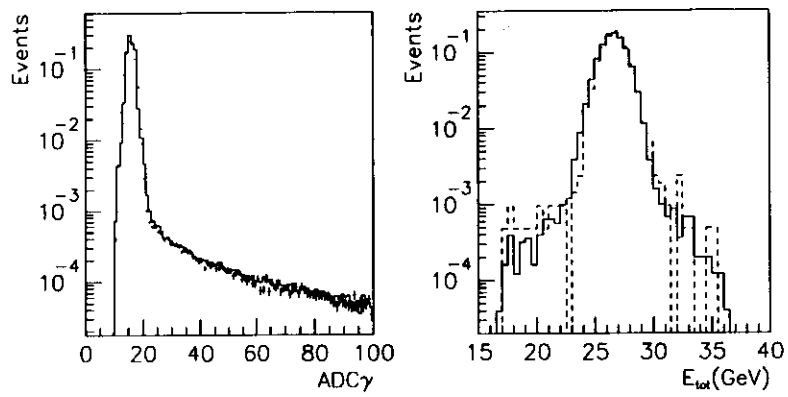

Figure 5.3: Measured (solid line) and simulated (crosses, dashed line) distributions of ADC_γ and E_{tot} .

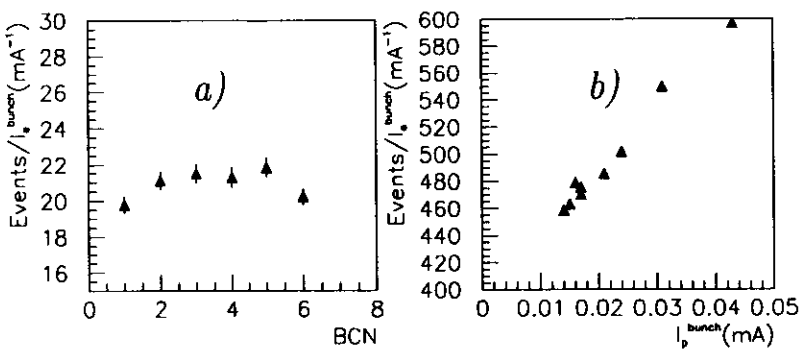

Figure 5.4: (a) The number of *egas* bremsstrahlung events (normalized to the electron bunch current) plotted as a function of the BCN; (b) the number of bremsstrahlung events (normalized to the electron bunch current) plotted as a function of the proton bunch current.

electron bunch currents[1] as a function of BCN. In Fig. 5.4a the measured normalized rates are shown, and the deviations from a flat distribution directly measure the inaccuracy of the subtraction method.

The subtraction method was also checked for luminosity runs. For example, for a run with particularly low proton beam current, the measured deviations of the rates (normalized to the electron bunch currents) from a linear increase with the proton bunch current (see Fig. 5.4b) provides an upper limit on the accuracy of the method.

In this way we have estimated the average accuracy of the background subtraction to be at a level of 4-5% and thus the contribution to the error of the luminosity $\Delta\mathcal{L}/\mathcal{L}$ is $5\% R_{egas}/R_{ep}$, where R_{ep}, R_{egas} are the rates of *ep* and *egas* bremsstrahlung events, respectively. Typically, the error in the measured luminosity due to the background subtraction was smaller than 2%, except for the measurement based on the counting rate of bremsstrahlung electrons. In this measurement the ratio R_{egas}/R_{ep} was typically 1-1.5, therefore the uncertainty in the luminosity measurement due to the *egas* subtraction was 7%.

5.4 Satellite Bunch Corrections

The error in the electron satellite bunch correction can be split into two separate sources: the measurement of the current of the satellite bunches and the estimation of the specific luminosity for collisions of such bunches with protons. The current of the satellite bunches relative to the current of the main bunches have been measured by fitting the C5 timing distributions (see Section 3.3.4) with a combination of exponential and Gaussian functions (see Fig. 5.5). The ratio of the heights of the two peaks, separated by 8ns, measures the ratio of the currents. The position of the two peaks measures the timing of bunches with respect to the HERA clock, hence also measures the timing of the signals in the luminosity monitor with respect to the FADC gates. The error of the ratio was assumed to be the sum of the statistical error of the fits and the systematic error due to the difference between the fitted functions and the actual distributions. The error was calculated separately for each run (if the C5 data was available). The mean ratio of the currents of the satellite and main bunches was found to be $11 \pm 2\%$.

The specific luminosity for the collision of satellite bunches with the proton bunches is lower than that for the main bunches because they do not occur at the nominal IP and the bunches are larger. The results of CTD and C5 measurements of the z distribution of the collision region show that also for main bunches the center of the collision region did not always coincide with the nominal position of the IP. The shift of the IP is included in the calculation of $\mathcal{L}_{spec}$ for the satellite and nominal bunches for each ZEUS run. Therefore, assuming a 20% error in the size of the electron and proton bunches and an error of $\pm 8cm$ in the measured mean z position of the collision region, we found that the ratio of the specific luminosities for the main and satellite bunches was known with an accuracy of approximately 10%.

The efficiency of the bremsstrahlung trigger for collisions of satellite bunches can be derived from the delay curves of the calorimeters. The 8 nsec timing delay results in

[1]The correction for multiple events was negligible.

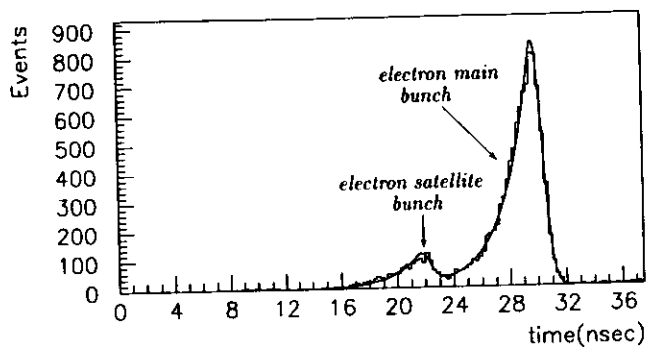

Figure 5.5: A C5 timing distribution of the electron bunches with the corresponding fit.

a decrease of trigger efficiency of approximately 8%. The error in this estimate can be neglected.

The relative luminosity error caused by the correction for the contribution of collisions of satellite bunches is thus equal to $0.014 = (0.1 \oplus 0.1)$.

5.5 Multiple Events

The accuracy of the simulation of the multiple events in the measurement of the luminosity was checked by inspecting the high energy tails in E_γ (beyond the kinematic end-point) and the distributions of E_{tot}. The difference between the MC expectations and the measured shape of the distributions in the regions populated only by multiple events is of the order of 10% (see in Fig. 5.6).

Thus, the relative luminosity error due to multiple events can be estimated as $10\%\Delta R/R$, where ΔR is the correction of the measured event rate R caused by this effect. This ratio was typically smaller than 0.01, and therefore this error is negligible.

5.6 Summary

In addition to the errors considered above, the performance of the scalers used to count the bremsstrahlung events was also checked. This was done by comparing the rates measured with three independent scalers: one LUMI VME resident, and two others available in the FLT system. The distribution of the ratios of the rates measured with these scalers, shown in Fig. 5.7, indicates that the counting errors are smaller than 0.5%.

The total systematic error of the main luminosity measurement ($E_\gamma > 5GeV$) is presented in Tab. 5.2. An error in the bremsstrahlung cross-section calculation of less

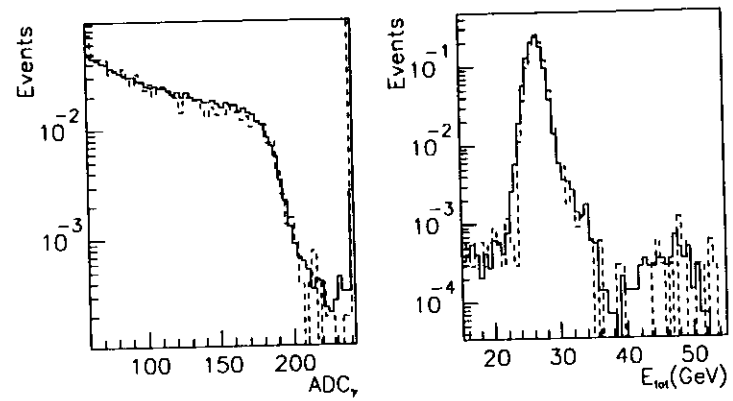

Figure 5.6: The measured (solid line) and expected (dashed line) distributions of ADC_γ and E_{tot}.

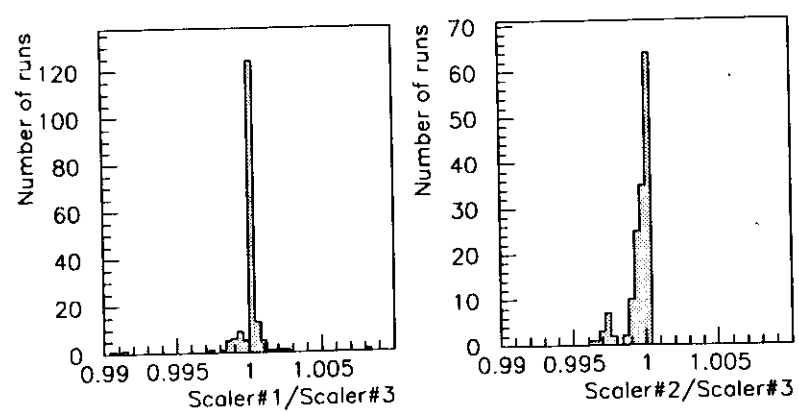

Figure 5.7: Distributions of the ratios of the bremsstrahlung rates measured with three independent scalers.

Component	Error
Energy Calibration/Resolution	2.5%
Photon Acceptance	2.5%
egas Background Subtraction	2%
Satellite Bunches	1.5%
Multiple Events	-
Counting Errors	< 0.5%
Bremsstrahlung Cross-Section	<1%
Total Error (sys.)	4.5%

Table 5.2: **A summary of the systematic errors for the main luminosity measurement.**

Trigger Type	Acceptance Error	Calibration/ Resolution Error
$E_\gamma > 10GeV$	2.5%	2.5%
$E_{e'} > 4GeV$	≈8%	< 0.2%
$19 > E_{e'} > 7GeV \& 16 > E_\gamma > 10GeV$	≈5%	1.5%

Table 5.3: **Contributions to the total systematic error for different luminosity triggers.**

than 1% was assumed, as discussed in Section 1.4.

The components of the systematic error are equal for each method of the luminosity measurement in the LUM1 monitor except for the errors in the acceptance measurements and the calibration of the calorimeters[2]. The contributions of these errors for selected trigger types are listed in Tab. 5.3.

[2]For the $E_{e'} > 4GeV$ trigger also the uncertainty in the *egas* subtraction is different than for the other triggers.

Chapter 6

Conclusions

The analysis of the data taken with the ZEUS luminosity monitor during the '92 HERA run period shows that an accurate measurement of *ep* bremsstrahlung events at HERA is feasible and provides a reliable measurement of the collider luminosity.

The energy scale can be maintained at a precision of 2% which is required for an accurate luminosity measurement, by utilizing special calibration methods. The tests and cross-check procedures, especially those concerning the determination of the acceptance and the details of the energy measurement, lead to a good understanding of the various instrumental effects which occur in the measurement. Additionally, two methods of dealing with the effects of multiple events were analyzed, and the contribution of the collision of electron satellite bunches with the proton bunches were also examined. The background sources were studied and the methods of background correction were discussed. With the results of these studies an accuracy of 5% of the luminosity measurement has been achieved.

From the considerations of the systematic errors in the ZEUS luminosity measurement one can see that at present the error in the determination of the photon acceptance and the uncertainties in the energy measurement are the main contributions to the total systematic error. A number of changes in the experimental setup (which are already applied or are in preparation) will minimize these uncertainties. A vacuum pipe extending between the photon exit window and the face of γcal has been installed to decrease the number of conversions of photons between the exit window and the photon calorimeter. New designs of γcal and of the carbon filter are under investigation, in which these two parts will be combined into one to improve the energy resolution and linearity of the bremsstrahlung photon measurement. The plan is to integrate the filter with the calorimeter in the form of a thick ($\approx 3X_0$) first absorber plate followed by an correspondingly thicker scintillator plate to compensate for the larger energy loss in the absorber. The thicknesses of the first two plates are chosen to keep the synchrotron radiation background at a negligible level and to mantain a good linearity of the energy measurement, especially for low energy photons. The regular lead/scintillator stack follows and the position detector consisting of scintillator fingers is inserted at a depth of $3X_0$. With these changes the systematic error caused by the energy resolution and the uncertainty in the energy scale are expected to be reduced to a level of 1–2%.

The improvements in the apparatus will also aid in the measurement of the geometric

acceptance of bremsstrahlung photons because with less absorber in front of γcal a better measurement of the angular distribution of the photon beam will be possible. A precise survey of the HERA magnets as well as more tests including measurements of the beam trajectories with the HERA beam monitors would help to determine the geometry and performance of the HERA beam-line magnets. One can expect that this will decrease the error of the photon acceptance to 1%. The installation in $e^{-}cal$ of an electron position detector during the 92/93 winter shutdown offers a much better control of acceptance of the secondary electrons and permits a better electron energy calibration. This will improve the precision of the luminosity measurements based on electron detection which will provide a powerful cross-check with the measurement currently used.

The error of the *egas* background subtraction and the correction for the contribution of satellite bunches depend on the performance of the HERA collider, e.g. the pressure of the residual gas in the beam pipe and th relative size of the satellite bunches. It is expeced that these problems will be solved.

With the nominal luminosity the effects related to high event rates (e.g. signal pileup in the electronics, deterioration of the photomultiplier gains due to the large anode currents, radiation damage of the scintillator, and multiple events) will presumably be the most important. Extensive laboratory tests of the front-end electronics and of the FADC cards now being performed will ensure a good understanding of the performance of the electronics in such conditions.

As a result of these efforts, it is therefore possible that an experimental accuracy of the luminosity measurement of 2% and less can be reached. In this case, more careful estimates of the theoretical uncertainties due to higher order corrections to the Bethe-Heitler cross-section as well as the effects of the finite beam sizes[1] are required.

In the '92 HERA run period a transverse polarization of the electron beam of 60% was observed [23]. This result and the installation of spin rotators in HERA allow one to hope for a longitudinally polarized electron beam being stored in HERA in the near future. It follows from the conservation of helicity that when the beam electrons are longitudinally polarized the bremsstrahlung photons with energies close to the beam energy are circularly polarized. The method of measurement of the photon circular polarization described in [63] appears to be applicable in the ZEUS luminosity monitor. The method utilizes a pair of crystal plates, the first plate converts the circular polarization of the photon to linear [64], and the second plate analyzes the degree of polarization through the measurement of the photon absorption. This opens the new possibilty of the use of the ZEUS luminosity monitor for the measurement of the longitudinal polarization of the electron beam at the ZEUS IP.

[1] With an improved energy resolution at low photon energies the exciting possibility of the measurement of the beam-size effect at HERA [7] becomes feasible.

Acknowledgements

I would like to thank very much the Directorate of the DESY laboratory for supporting my stay in Hamburg.
I am very much grateful to Professor Danuta Kisielewska and Professor Andrzej Eskreys for their firm support and constant encouragement during the writing of this thesis.
I thank very much Dr. Günter Wolf for much useful advice and his kind support, especially during my 'early days' at DESY.
I would like to express much gratitude to Dr. Robert Klanner for his numerous suggestions and many useful comments while I was working on the luminosity measurement.
I wish to thank very much all my collegues in the LUMI group, in particular Leszek Adamczyk for his help in the preparation of the test beam results as well as Mariusz Przybycień and Dr. Leszek Zawiejski for helping me with the Monte Carlo simulations.
I thank a lot all of my collegues from the ZEUS collaboration for their very pleasant and inspiring cooperation, especially Dr. James Crittenden for co-working on the problem of satellite bunches and Johannes Mainusch for fruitful discussions on the calibration of the LUMI calorimeters.
I am very much grateful to Mark Lomperski for his hard work on polishing my English and smoothing my style.
Last but not least I would like to thank my family for their help, endless patience and care.

Bibliography

[1] D.Kisielewska et al., "Fast Luminosity Monitoring at HERA", DESY-HERA Report 85-25.

[2] J.Andruszków et al., "First Measurements of HERA Luminosity by ZEUS Lumi Monitor", DESY 92-066, May 1992.

[3] M.Derrick et al., ZEUS Collaboration, Phys. Lett. **B293** (1992) 465.

[4] M.Costa, K.Piotrzkowski, L.Suszycki, "Measurement of the Total Photoproduction Cross Section with the ZEUS Luminosity Monitor", Proc. of the Workshop Physics at HERA, Vol.1, 509-518, Hamburg, October 1991.

[5] S.Jadach, M.Jeżabek, W.Płaczek, Phys. Lett. **B248** (1990) 417.

[6] H.Abramowicz et al., "A Determination of F_2 with the 1992 Data", ZEUS-Note 93-078, July 1993.

[7] G.L.Kotkin, V.G.Serbo and A.Schiller, Int. J. Mod. Phys. **A7** (1992) 4707-4745.

[8] L.D.Landau, E.M.Lifshitz, "The Classical Theory of Fields", Oxford, Pergamon Press, 4th ed., 1975.

[9] T.Suzuki, "General Formulas of Luminosity for Various Types of Colliding Beam Machines", KEK-76-3, July 1976.

[10] D.Decamp et al., ALEPH Collaboration, Zeit. f. Phys. **C53** (1992) 376.

[11] G.Arison et al., UA1 Collaboration, Phys. Lett. **B128** (1983) 336.

[12] S.White et al., CDF Collaboration, "Measurement of the $\bar{p}p$ Total Cross-Section at $\sqrt{s} = 1800\ GeV$", Fermilab-Conf-91-268-E, October 1991.

[13] C.Carboni et al., Nucl. Phys. **B254** (1985) 697.

[14] S.van der Meer, "Calibration of the Effective Beam Height in the ISR", CERN-ISR-PO/68-31, June 1968.

[15] K.Potter, "Luminosity Measurements and Calculations", Proc. of the CERN Accelerator School, Vol.1, CERN 85-19, November 1985.

[16] N.C.Christofilos, unpublished report, 1950;
E.D.Courant, M.S.Livingstone and H.S.Snyder, Phys. Rev. **88** (1952) 1190.

[17] A.Poncet, "Industry and the Accelerator Vacuum Field", Proc. of the CERN Accelerator School, CERN 89-05, April 1989.

[18] M.Sand, "The Physics of Electron Storage Rings: an Introduction", SLAC-121, November 1970.

[19] R.Siemann, "Introduction to the Physics of Particle Accelerators", CLNS 90/1021, September 1990.

[20] E.Wilson, "Transverse Beam Dynamics", Proc. of the CERN Accelerator School, Vol.1, CERN 85-19, November 1985.

[21] Hartz Seminar, Bad Lauterberg 1992, DESY HERA 92-07, April 1992;
Hartz Seminar, Bad Lauterberg 1993, DESY Internal Report.

[22] G.Wolf, "HERA: Physics, Machine and Experiments", DESY 86-089, August 1986.

[23] D.P.Barber et al., "High Spin Polarization at the HERA Electron Storage Ring", DESY-93-038, April 1993.

[24] M.Derrick et al., Nucl. Instr. Meth. **A309** (1991) 77;
A.Andersen et al., ibid. **A309** (1991) 101;
ZEUS Collaboration, The ZEUS Detector Status Report, DESY Internal Report, February 1993.

[25] C.Bini et al., Nucl. Instr. Meth. **A306** (1991) 467.

[26] H.Bethe and W.Heitler, Proc. Roy. Soc. **A146** (1934) 83.

[27] K.J.F.Gaemers, M.van der Horst, Nucl. Phys. **B316** (1989) 269; erratum, ibid. **B336** (1990) 184.

[28] A.A.Akhundov, D.Yu.Bardin and L.V.Kalinovskaya, Zeit. f. Phys. **C51** (1991) 557.

[29] M.van der Horst, Phys. Lett. **B244** (1990) 107.

[30] M.van der Horst, Nucl. Phys. **B347** (1990) 149.

[31] V.B.Berestetskii, E.M.Lifshitz and L.P.Pitaevskii, "Quantum Electrodynamics", Oxford, Pergamon Press, 2nd ed., 1982.

[32] A.E.Blinov et al., Phys. Lett. **B113** (1982) 423;
Yu.A.Tikhonov, Candidate Thesis, Novosibirsk 1982.

[33] V.N.Baier, V.M.Katkov and V.M.Strakhovenko, Yad. Fiz. **36** (1982) 163;
A.I.Burov, Ya.S.Derbenev, preprint INP 82-07, Novosibirsk 1982.

[34] K.Piotrzkowski, L.Suszycki, "BREMGE, A Monte Carlo Generator of High Energy Electron-Proton and Electron-Nucleus Bremsstrahlung Events", Proc. of the Workshop, Physics at HERA, Vol.3, 1463-1467, Hamburg, October 1991.

[35] C.W.Fabjan, T.Ludlam, Ann. Rev. Nucl. Part. Sci. **32** (1982) 335.

[36] Philips Inc., Catalogue of Photomultiplier Tubes, April 1984.

[37] B.Bicken et al., IEEE Trans. Nucl. Sci. **NS-38** (1991) 188.

[38] W.R.Nelson, H.Hirayama and D.W.O.Rogers, "The EGS4 Code System", SLAC-0265, December 1985.

[39] J.Andruszków et al., "Calibration of the Luminosity Monitor Detectors at the DESY Electron Beam", ZEUS Note 90-108, October 1990.

[40] J.Andruszków et al., "Calibration of the Luminosity Monitor Detectors at the CERN T9 PS Test Beam", ZEUS Note 90-125, December 1990.

[41] L.Adamczyk, private communication;
L.Adamczyk et al., ZEUS-Note in preparation.

[42] K.Piotrzkowski, "Results of the Position Detector Prototype Tests", ZEUS Note 90-030, March 1990.

[43] D.Kisielewska, K.Piotrzkowski, "Electron Position Detector for the LUMI Monitor", ZEUS-Note 91-066, July 1991.

[44] K.Tesch, Part. Accel. **9** (1979) 201.

[45] G.Hall et al., Nucl. Instr. Meth. **A253** (1987) 491.

[46] P.Jarron, M.Goyot, Nucl. Instr. Meth. **226** (1984) 156.

[47] W.Dąbrowski, "Fast Neutron Damage of Silicon PIN Photodiodes", in: E.Fernandez, G.Jarlskog, (eds), Instrumentation Technology for High-Luminosity Hadron Colliders, Proc. ECFA Study Week, Barcelona, 1989, CERN 89-10.

[48] H.Dinter, "Synchrotronstrahlung im HERA-Tunnel", DESY Internal Report, DESY D3-056, September 1985.

[49] R.Brinkmann, "Simulation of Background from Proton Losses in the HERA Straight Sections", DESY-HERA 87-019.

[50] J.Crittenden, M.Nakahata and K.Piotrzkowski, "Results of the C5 Detector Time Distributions for the Fall 1992 Running Period", ZEUS-Note 93-041, April 1993.

[51] MOZART - ZEUS Monte Carlo simulation program.

[52] W.Bialowons, private communication.

[53] D.Trines, private communication.

[54] J.D.Jackson, "Classical Electrodynamics", New York, Wiley, 2nd ed., 1975.

[55] Particle Data Group, K.Hikasa et al., Phys. Rev. **D45** (1992).

[56] K.Siegbahn (ed.), "Beta- and Gamma-ray Spectroscopy", Amsterdam, North-Holland, 1955.

[57] V.M.Budnev et al., Nucl. Phys. **B63** (1973) 519.

[58] V.M.Budnev et al., Phys. Rep. **C15** (1975) 181.

[59] R.Janik, private communication.

[60] V.I.Telnov, Nucl. Instr. Meth. **A260** (1987) 304;
B.Dehning et al., Phys. Lett. **B249** (1990) 145;
C.Bini et al., Phys. Lett. **B262** (1991) 135.

[61] M.Lomperski, "Compton Scattering off Black Body Radiation and Other Backgrounds of the HERA Polarimeter", DESY 93-045, June 1993.

[62] R.P.Feynman, "Photon-Hadron Interactions", Reading, Benjamin, 1972.

[63] G.De Zorzi, G.Diambrini-Palazzi and A.Di Domenico, "Use of Single Bremsstrahlung with Crystals for Measuring Longitudinal Polarization at LEP", in: Polarization at LEP, Vol. 2, 64-81, CERN, 1988.

[64] N.Cabibbo et al., Nuovo Cimento **27** (1963) 979;
N.Cabibbo et al., Phys. Rev. Lett. **9** (1962) 270.

Appendix

Detectors of the Luminosity Monitor

Photon Detector			
Component	Distance from IP (m)	Material	Shape/Size
Window	92.5	Copper-Beryllium	Circle 50 mm radius, 1.5 mm , $\approx 0.1\ X_0$ thick
Filter	103.15	Carbon	Square $(175 \times 175)mm^2$, variable thickness: 0.5-3.5 X_0
Čerenkov Counter	104.95	Air at NTP Al windows	Circle 100 mm radius, active length 1080 mm, two windows 3 mm each, in total 0.067 X_0 thick
Calorimeter	106.94	Absorber Lead Scintillator SCSN38	Square plates, $(180 \times 180)mm^2$, 5.7 mm thick, SCSN38 2.6 mm thick, depth $22X_0$
Position Detector	inside calorimeter after $7X_0$	Scintillator NE110	Two crossed planes of fingers: 14 horizontally $(10 \times 10 \times 163)mm^3$, 16 vertically $(10 \times 10 \times 143)mm^3$

Electron Detector			
Component	Distance from IP (m)	Material	Shape/Size
Window	27.29	Steel	69 mm radius, 1.5 mm $\approx$ 0.085 X_0 thick
Calorimeter	34.68	Absorber Lead Scintillator SCSN38	Square plates, $(250 \times 250)mm^2$, 5.7 mm thick, SCSN38 2.6 mm thick, depth $24X_0$
Position Detector	inside calorimeter after $7X_0$	Scintillator NE110	Two crossed planes of fingers: 12 horizontally $(13 \times 10 \times 218.5)mm^3$, 16 vertically $(13 \times 10 \times 166.5)mm^3$